SLAC-R-510
UC-414

Measurement of the Polarized Forward-Backward Asymmetry of B quarks at SLD *

V. V. Serbo

Stanford Linear Accelerator Center
Stanford University
Stanford, CA 94309

SLAC-Report-510
July 1997

Prepared for the Department of Energy
under contract number DE-AC03-76SF00515

Printed in the United States of America. Available from the National Technical Information Service, U.S. Department of Commerce, 5285 Port Royal Road, Springfield, VA 22161.

*Ph.D. thesis, University of Wisconsin-Madison.

Abstract

Measurement of the Polarized Forward-Backward Asymmetry of B Quarks at SLD

Victor V. Serbo

Under the supervision of Professor Richard Prepost

At the University of Wisconsin-Madison

This thesis presents a direct measurement of the parity-violating parameter A_b using the Left-Right Forward-Backward asymmetry of $b\bar{b}$ pair production at the Z^0 pole. The measurement was done at the Stanford Linear Accelerator Center (SLAC) using data from the SLAC Large Detector (SLD). We take advantage of the high polarization of the SLAC Linear Collider (SLC) electron beam. To identify heavy flavour decays of the Z^0, we use a b-tag based on the topological reconstruction of the mass of the B vertex. Discrimination between the b and $\bar{b}$ quark directions is provided by a self-calibrating jet-charge technique. This technique allows calibration of the analyzing power from data and gives a much reduced model dependence. Based on our 1994-95 (1993) sample of 100,000 (50,000) Z^0 decays recorded with an electron beam polarization of $< P_e >= 77\%$ (63%), we have obtained $A_b = 0.911 \pm 0.045(stat) \pm 0.045(syst)$. This value is in good agreement with the Standard Model.

Acknowledgments

The road to this degree was long and rough. It stretched over many years and many places, from the city of Novosibirsk somewhere in the depths of Siberia, through the American Midwest and to sunny California. Many people have helped me along the way.

I personally thank my advisor, Richard Prepost, for accepting me as his student and supporting me through long years of graduate school. Although we have disagreed on some points, his arguments were always clear, sharp, and directed right at the heart of the problem.

All members of the Wisconsin group at SLAC deserve special thanks: Henry Band for getting me involved in hardware work and showing the inner side of the SLC and polarimetry; Jim Johnson for always being there when I needed friendly advice, for reading patiently through my thesis and helping me convert it into "Standard English"; and Geordie Zapalac, who pioneered B_s mixing studies at SLD and showed me an example of scientific professionalism and dedication.

Working at SLD has been challenging and rewarding. I want to thank all members of the SLD collaboration for creating this unique atmosphere, this feeling of being in a big family. I will miss it. Special thanks goes to Su Dong, whose deep knowledge of physics, critical way of thinking, and ability to work 24 hours a day will always serve me as a model. Bruce Schumm, the leader of our SLD Asymmetry Group, deserves

many thanks. His support for new ideas, passion for perfection and unique sense of humor made our weekly meetings enjoyable and productive. Many other members of the SLD Heavy Flavor Group have contributed to my development as a physicist, and I am thankful for their support.

Thanks is not enough for my parents, Nadejda and Valery Serbo. It is through their example that I got interested in science.

And last but most important I thank my dear wife Shinar for her infinite love and support during these challenging years. Not only my graduate work, but my whole life would be incomplete without her. It is to her that I dedicate this thesis.

Table of Contents

List of Figures

List of Tables

Chapter 1

Introduction

1.1 The Standard Model

The Standard Model of electroweak interactions (SM), developed by Glashow [1], Weinberg [2] and Salam [3], combines the electromagnetic and weak interactions into a single interaction with $SU(2) \times U(1)$ gauge symmetry. Presented here is a brief introduction to the SM. A detailed description of the Standard Model can be found, for example, in References [4] [5]. The current status of the SM precision tests is given in Reference [6].

1.1.1 Overview

The first hint of parity violation came from the physics of strange particles. Two particles had been discovered that had the same mass and lifetime but decayed into final states with different parity. This puzzle was solved by Lee and Yang [7] by proposing that parity is not conserved in weak processes. These two particles then correspond to two different decay channels of a single particle, called today the K-meson:

$$K^+ \to \pi^+\pi^+\pi^-,\ \pi^+\pi^0\ . \tag{1.1}$$

A series of experiments [8]–[10] was conducted to test parity conservation in β-

decays and in $\pi^{\pm}$, $\mu^{\pm}$ decays, finding that parity was maximally violated by charged weak currents. In 1973 weak neutral currents (WNCs), predicted by the theory, were discovered in a purely leptonic process [11]:

$$\bar{\nu_{\mu}} + e^{-} \rightarrow \bar{\nu_{\mu}} + e^{-} \ . \tag{1.2}$$

Later WNCs were also observed in neutrino-nucleon deep-inelastic scattering [12]. The direct observation of the $W^{\pm}$ and Z^{0} bosons at CERN in 1983 [13] [14] completed the gauge boson sector, confirming the structure of the Standard Model.

The recent discovery of the missing third-generation particle, the t quark, at Fermilab [15] [16], left no doubts about the doublet structure of generations. The only particle that is required by the Standard Model that has not been observed is the Higgs boson H. The Higgs boson plays a special role in the Standard Model, providing a mechanism for the Z^{0} and $W^{\pm}$ bosons to have mass. Though not observed directly, the Higgs affects measurements at the one loop level such that m_H can be extracted from experiment. Such indirect measurements yield a Higgs mass upper limit at the 1 σ level [17] of $m_H < 360\ GeV$.

The very precise measurement of the Z^{0} boson mass from LEP [27] has changed the way the Standard Model is tested. Apart from the fermion masses and Higgs mass, there are only three free parameters in the SM. Three experimental inputs are chosen to be the Fermi constant G_F extracted from the muon decay rate, the fine structure constant $\alpha(m_Z)$ extrapolated from the low energy measurements, and the

Z^0 mass. Other observables, like m_W, A_b, R_b, can be predicted in the framework of the Standard Model. Thus an experimental measurement of additional electroweak parameters could be used to check and constrain theoretical predictions.

For the purpose of completeness we should mention some other tests of the Standard Model involving WNCs that can be performed away from the Z^0 resonance. Electromagnetic interactions of two fermions are always accompanied by the Z^0 exchange channel (Figure 1.1). While at low energy the Z^0 channel is suppressed by a factor of Q^2/M_Z^2, where Q^2 is the square of the momentum transfer, the effect can be measured in a sufficiently precise experiment. An important low Q^2 manifestation of Z^0 exchange is the atomic parity-violation (APV) effect caused by the Z^0 channel interaction between an electron and nucleus in an atom.

Parity violation associated with Z^0 exchange allows a small mixing between atomic S and P wave states. This mixing can be detected by observing the difference of the induced transition rates of an atom when the polarization of an incident laser beam exciting the atom is reversed. Recent measurements of the amplitude of the parity-nonconserving transition between the $6S$ and $7S$ states of cesium [22], done at Boulder, shows an impressive factor of 7 improvement in experimental precision over previous results. The total error, however, is dominated by the theoretical uncertainty of $\sim 1\%$ arising from the atomic matrix element calculations. In the framework of the Standard Model this result yields the value of the mixing angle (described in Section 1.1.2) $\sin^2\theta_W = 0.2261 \pm 0.0012(exp.) \pm 0.0041(theory)$, a factor of ~ 20 less

precise than the combined LEP/SLC measurement.

Even though the atomic parity-violation measurements do not reach the accuracy of the LEP/SLC experiments in determining the individual parameters of the Standard Model, they are important in many aspects. Different systematics, radiative corrections, and the small momentum transfer regime make the APV measurements a valuable addition to high energy experiments.

The scattering of longitudinally polarized electrons on nuclei is another way to observe the effect. The pioneering SLAC polarized $eD \to eX$ asymmetry experiment [18] established parity violation in the weak neutral current in the late 1970's. Three subsequent experiments have measured parity violation in muon-carbon deep inelastic scattering [19] (CERN), quasielastic electron-beryllium scattering [20] (at Mainz), and in electron-carbon elastic scattering [21] (at MIT-Bates). If expressed in terms of the Standard Model, the Bates experiment provides the smallest error on $\sin^2\theta_W = 0.221 \pm 0.014 \pm 0.004$.

Another way to detect effects of Z^0 exchange is to look for asymmetry in polarized e^-e^- scattering. While this is a pure leptonic process with small theoretical uncertainties and low backgrounds, it is challenging experimentally since the expected asymmetry is very small (a few parts per ten million). A proposal is under consideration now at SLAC [23] to measure parity violation in Møller scattering by measuring the polarized left-right asymmetry with statistical error better than 10^{-8}.

As of today, the Standard Model remains the preferred theory of electroweak in-

Table 1.1: Properties of fundamental fermions.

FAMILY			PARAMETERS		
1	2	3	T^3	Y	q
$\begin{pmatrix}\nu_e\\ e\end{pmatrix}_L$	$\begin{pmatrix}\nu_\mu\\ \mu\end{pmatrix}_L$	$\begin{pmatrix}\nu_\tau\\ \tau\end{pmatrix}_L$	$\begin{pmatrix}1/2\\ -1/2\end{pmatrix}$	$\begin{pmatrix}-1\\ -1\end{pmatrix}$	$\begin{pmatrix}0\\ -1\end{pmatrix}$
$\begin{pmatrix}u\\ d\end{pmatrix}_L$	$\begin{pmatrix}c\\ s\end{pmatrix}_L$	$\begin{pmatrix}t\\ b\end{pmatrix}_L$	$\begin{pmatrix}1/2\\ -1/2\end{pmatrix}$	$\begin{pmatrix}1/3\\ 1/3\end{pmatrix}$	$\begin{pmatrix}2/3\\ -1/3\end{pmatrix}$
e_R	μ_R	τ_R	0	-2	-1
u_R	c_R	t_R	0	$4/3$	$2/3$
d_R	s_R	b_R	0	$-2/3$	$-1/3$

teractions, describing a wide range of experiments with impressive precision.

1.1.2 Fundamental Particles

Two sets of fundamental particles are defined in the Standard Model: leptons and quarks. Leptons are subject only to electroweak interactions while quarks also interact strongly. The theory that describes the strong interaction is the Quantum ChromoDynamics (QCD) theory. These two sets can be ordered by mass in three families and exist in the form of left-handed doublets (L) and right-handed singlets (R).

A set of gauge bosons is also introduced to mediate interactions. The eigenstates of electroweak bosons are an SU(2) triplet W^i $(i = 1, 2, 3)$ and a U(1) singlet B. $\boldsymbol{W}$ couples to the weak isospin (T^3) with a coupling constant g. B couples to the weak hypercharge (Y) with a coupling constant g'. The assignment of the isospin,

hypercharge and electric charge (q) for the fundamental fermions is shown in Table 1.1. Observable bosons, however, are a mixture of $\boldsymbol{W}$ and B and can be described as:

$$\begin{aligned} massive\ charged\ fields: \quad W^{\pm} &= (W^1 \mp iW^2)/\sqrt{2}\ , \\ massive\ neutral\ field: \quad Z &= -B\sin\theta_W + W^3\cos\theta_W\ , \\ massless\ photon: \quad A &= B\cos\theta_W + W^3\sin\theta_W\ , \end{aligned} \tag{1.3}$$

where θ_W is a mixing angle. From experiments we know that the photon field does not violate parity, which gives the constraint:

$$e = g\sin\theta_W = g'\cos\theta_W \tag{1.4}$$

where e is the electric coupling constant.

The resulting couplings of the gauge bosons to fermions are pure vector (V) coupling for the photon, ($V-A$) coupling for the $W^{\pm}$ (giving maximum parity violation), and the coupling for the Z^0 in the form of

$$v_f \ - \ a_f\gamma^5\ , \tag{1.5}$$

where $v_f = T^3 - 2q\sin^2\theta_W$ is the vector coupling and $a_f = T^3$ is the axial coupling for the $Zb\bar{b}$ vertex.

In order to give mass to gauge bosons, a doublet of Higgs scalar fields is introduced

$$\phi = \begin{pmatrix} \phi^+ \\ \phi^0 \end{pmatrix}, \tag{1.6}$$

which spontaneously break the $SU(2) \times U(1)$ symmetry, leaving the $U(1)$ subgroup of the theory unbroken. The remaining $U(1)_{EM}$ symmetry leads to the massless photon. In the framework of this formalism, masses of the Z^0 and $W^{\pm}$ bosons can be expressed in terms of coupling constants g, g', and the vacuum expectation value of the Higgs field, v:

$$\begin{aligned} M_{W^{\pm}} &= \frac{1}{2} g v, \\ M_{Z^0} &= \frac{1}{2} v \sqrt{g^2 + g'^2}. \end{aligned} \tag{1.7}$$

At this point the theory has only three free parameters: the Weinberg angle θ_W, the electric coupling constant e, and the Higgs vacuum expectation value v. Three conventional experimental inputs are: the Fermi constant G_F extracted from the muon decay rate, the fine structure constant $\alpha(m_Z)$ extrapolated from the low energy measurements, and the Z^0 mass measured precisely at LEP.

1.1.3 Electroweak Interactions

In the particle physics formalism the probability of an interaction happening in a particular angular configuration is given by the differential cross section. For the particular process $e^+e^- \to Z/\gamma \to f\bar{f}$ (Figure 1.1), the differential cross section in the center-of-mass frame can be written in terms of the matrix element of γ and Z exchange (M_γ, M_Z) and the total energy (s) as:

$$\frac{d\sigma}{d\Omega} = \frac{1}{64\pi^2 s} \left| M_\gamma + M_Z \right|^2 \ , \tag{1.8}$$

where $d\Omega$ is the element of solid angle.

In the Quantum ElectroDynamucs (QED) theory the matrix element is derived using the interaction of the particle current with the field:

$$-ie j_\mu^{em} A^\mu = -ie \left(\bar{\psi}\gamma_\mu Q \psi\right) A^\mu \ . \tag{1.9}$$

The Feynman vertex factor $-eQ\gamma_\mu$ and propagator factor $-g_{\mu\nu}/s$ are then extracted from Equation 1.9. Thus the QED matrix element can be obtained in the form of

$$M_\gamma = -e^2 \left(\bar{f}\gamma_\nu f\right) \frac{1}{s} \left(\bar{e}\gamma^\nu e\right) \ , \tag{1.10}$$

where f and e represent the fermion and electron.

The weak interaction is incorporated into the formalism by introducing two basic interactions. First is an isospin triplet of weak currents, $\boldsymbol{J}_\mu$, coupled to three vector bosons $\boldsymbol{W}^\mu$,

$$-ig\boldsymbol{J}_\mu \boldsymbol{W}^\mu = -ig\bar{\chi}_L \gamma_\mu \boldsymbol{T}\boldsymbol{W}^\mu \chi_L \ , \tag{1.11}$$

where χ_L is one of the left-handed doublets (Table 1.1). Second is a weak hypercharge current, j_μ^Y, coupled to a vector boson B^μ,

$$-i\frac{g'}{2} j_\mu^Y B^\mu = -ig'\bar{\psi}\gamma_\mu \frac{Y}{2}\psi B^\mu \ , \tag{1.12}$$

where ψ is a singlet. $\boldsymbol{T}$ and Y are the generators of the SU(2) and U(1) groups of gauge transformations. In these terms the electromagnetic and weak neutral currents can be written as

$$j_\mu^{em} \ = \ J_\mu^3 + \frac{1}{2} j_\mu^Y \ ,$$

$$J_\mu^{NC} \quad = \quad J_\mu^3 - \sin^2\theta_W j_\mu^{em} \ , \tag{1.13}$$

and the interaction in the neutral current sector in terms of the physical fields (Equation 1.3) follows:

$$-iej_\mu^{em}A^\mu - \frac{ig}{\cos\theta_W}\left[J_\mu^3 - \sin^2\theta_W j_\mu^{em}\right]Z^\mu \ . \tag{1.14}$$

Thus the Z-exchange matrix element can be expressed as

$$M_Z = -\frac{g^2}{4\cos^2\theta_W}\left(\bar{f}\gamma^\nu\left(v_f - a_f\gamma^5\right)f\right)\frac{g_{\nu\mu} - k_\nu k_\mu/M_Z^2}{s - M_Z^2 + iM_Z,\ _Z}\left(\bar{e}\gamma^\mu\left(v_e - a_e\gamma^5\right)e\right) \ , \tag{1.15}$$

where f and e represent the fermion and electron, M_Z and , $_Z$ the mass and width of the Z^0, and k is the momentum transfer.

1.2 Asymmetries at the Z^0 Pole

The process of interest in is $e^+e^- \to f\bar{f}$, where f is a fermion (other than an electron). At tree level the only two diagrams that contribute to the cross-section are s-channel γ and Z^0 exchange with $\sigma_{e^+e^-\to Z^0} \gg \sigma_{e^+e^-\to\gamma}$ near the Z^0 boson resonance. Contributing Feynman diagrams are shown in Figure 1.1. It is also interesting to note that the $\gamma - Z$ interference term vanishes at $s = m_Z^2$. Before having a closer look at the asymmetry of the fermion production, definitions for the left-handed and right-handed couplings of the Z^0 to a fermion may be introduced:

$$c_L^{Zf} = (v^{Zf} + a^{Zf})/2 \ , \tag{1.16}$$

$$c_R^{Zf} = (v^{Zf} - a^{Zf})/2 \ . \tag{1.17}$$

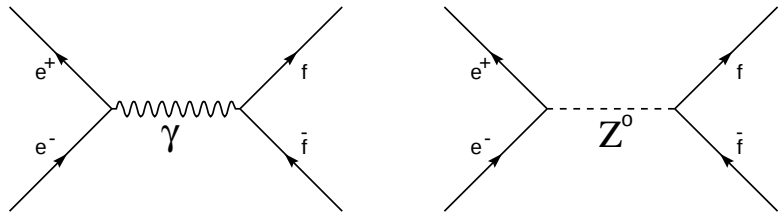

Figure 1.1: Tree-level Feynman diagrams for $e^+e^- \to f\bar{f}$.

Table 1.2: Coupling of the γ and Z^0 to fundamental fermions.

	γ coupling	Z^0 coupling			
fermion	Q_f	v^{Zf}	a^{Zf}	c_R^{Zf}	c_L^{Zf}
e, μ, τ	-1	$-\frac{1}{2} + 2\sin^2\theta_W$	$-\frac{1}{2}$	$\sin^2\theta_W$	$-\frac{1}{2} + \sin^2\theta_W$
ν_e, ν_μ, ν_τ	0	$\frac{1}{2}$	$\frac{1}{2}$	0	$\frac{1}{2}$
u, c, t	$\frac{2}{3}$	$\frac{1}{2} - \frac{4}{3}\sin^2\theta_W$	$\frac{1}{2}$	$-\frac{2}{3}\sin^2\theta_W$	$\frac{1}{2} - \frac{2}{3}\sin^2\theta_W$
d, s, b	$-\frac{1}{3}$	$-\frac{1}{2} + \frac{2}{3}\sin^2\theta_W$	$-\frac{1}{2}$	$\frac{1}{3}\sin^2\theta_W$	$-\frac{1}{2} + \frac{1}{3}\sin^2\theta_W$

Photon – fermion coupling is parity conserving and depends only on the electric charge of the fermion. A summary of all relevant couplings is given in Table 1.2.

Only the helicity of the incoming electron is considered for cross-section calculation, as the electron has to couple with the positron of the opposite helicity to produce a Z^0. Also a summation over the final-state fermion polarization is done [24] to obtain the result:

$$\frac{d\sigma_R}{d\Omega} \propto ({c_R^f}^2 + {c_L^f}^2)(1 + \cos^2\theta) + 2({c_R^f}^2 - {c_L^f}^2)\cos\theta \ , \tag{1.18}$$

$$\frac{d\sigma_L}{d\Omega} \propto ({c_R^f}^2 + {c_L^f}^2)(1 + \cos^2\theta) - 2({c_R^f}^2 - {c_L^f}^2)\cos\theta \ , \tag{1.19}$$

where the helicity index L (R) refers to the incoming electron and θ is the angle between the e^- beam and the outgoing fermion.

Table 1.3: Asymmetry A_f and sensitivity to $\sin^2\theta_W$.

Fermion	A_f	$\frac{\partial A_f}{\partial \sin^2\theta_W}$
e, μ, τ	0.16	−7.85
u, c, t	0.67	−3.45
d, s, b	0.94	−0.63

A more convenient formula can be obtained by using an asymmetry parameter:

$$A_f = \frac{(c_L^f)^2 - (c_R^f)^2}{(c_L^f)^2 + (c_R^f)^2} = \frac{2v_f a_f}{v_f^2 + a_f^2} \tag{1.20}$$

and combining the L and R electron states into the partially unpolarized initial state

$$\frac{d\sigma^f}{d\Omega} \propto (1 - A_e P_e)(1 + \cos^2\theta) + 2(A_e - P_e)A_f \cos\theta \ , \tag{1.21}$$

where P_e is the electron beam polarization. The asymmetry, A_f, and its sensitivity to $\sin^2\theta_W$, $\frac{\partial A_f}{\partial \sin^2\theta_W}$, are given in Table 1.3 for all fundamental fermions. Calculations were done for $\sin^2\theta_W = 0.23$.

1.2.1 Unpolarized Asymmetries

In the case of unpolarized initial beams, Equation 1.21 reduces to:

$$\frac{d\sigma^f}{d\Omega} \propto 1 + \cos^2\theta + 2A_e A_f \cos\theta \ . \tag{1.22}$$

The left-handed coupling of the Z^0 to the electron is bigger than the right-handed coupling, and as a result, the average spin of the Z boson along the z axis is not zero. To extract information from the data, a $\cos\theta$-dependent forward-backward asymmetry

can be formed:

$$A^f_{FB}(|\cos\theta|) = \frac{\sigma(\cos\theta) - \sigma(-\cos\theta)}{\sigma(\cos\theta) + \sigma(-\cos\theta)} = A_e A_f \frac{2\cos\theta}{1+\cos^2\theta} \ . \tag{1.23}$$

The main disadvantage of this method is that the product of the initial and final state couplings, $A_e A_f$, is measured and one has to rely on other experiments for the value of A_e. Also the value of A^f_{FB} is small and has a large energy dependence. Any polarization of initial beams, as well as any forward-backward detector asymmetry, would greatly affect the result.

1.2.2 Asymmetries in the Presence of Polarization

If the initial electron beam is polarized, we can form the "left-right forward-backward" asymmetry, $\tilde{A}^f_{FB}$, taking advantage of the separate helicity states:

$$\tilde{A}^f_{FB}(|\cos\theta|) = \frac{\sigma_L(\cos\theta) - \sigma_L(-\cos\theta) - \sigma_R(\cos\theta) + \sigma_R(-\cos\theta)}{\sigma_L(\cos\theta) + \sigma_L(-\cos\theta) + \sigma_R(\cos\theta) + \sigma_R(-\cos\theta)} = P_e A_f \frac{2\cos\theta}{1+\cos^2\theta} \ . \tag{1.24}$$

This way the product of the beam polarization and the final state asymmetry, $P_e A_f$, is measured. The advantage of this method is that the measurement is independent of the initial state couplings. Also the beam polarization at SLD is large and well measured ($P_e \approx 5A_e$).

It is important to note that the initial state asymmetry, A_e, can be measured separately in the same experiment by forming the left-right asymmetry:

$$\tilde{A}^{raw}_{LR} = \frac{\sigma_L - \sigma_R}{\sigma_L + \sigma_R} = P_e A_e \ , \tag{1.25}$$

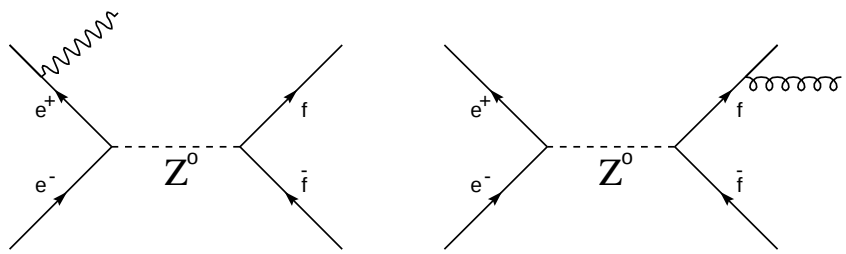

Figure 1.2: First order initial and final state radiation.

where $\sigma_{L(R)}$ is a cross-section integrated over the detector acceptance region for the left (right) electron beam polarization.

1.2.3 Radiative Corrections

The simple tree-level cross-section $\sigma_{e^+e-\to f\bar{f}}$ (Equation 1.21) is modified by initial state QED radiation (ISR), final state radiation (FSR), vertex corrections and propagator corrections.

The ISR is radiation of photons by the incoming electrons and positrons. It results in lower center-of-mass energy and non-zero momentum of produced Z bosons in the laboratory frame. Another important consequence of the ISR is that the $\gamma - Z$ interference term in $\sigma_{e^+e-} \to f\bar{f}$ does not vanish at the Z^0 pole, but $\approx 20\ MeV$ above it. The final state QED radiation is suppressed, and has a negligible effect on the asymmetry. The leading-order Feynman diagrams of the initial state QED and the final state QCD radiation are shown on Figure 1.2

Two diagrams that modify Z^0 production and decay vertexes are shown on Figure 1.3. The change in asymmetry due to QED radiation and vertex corrections was

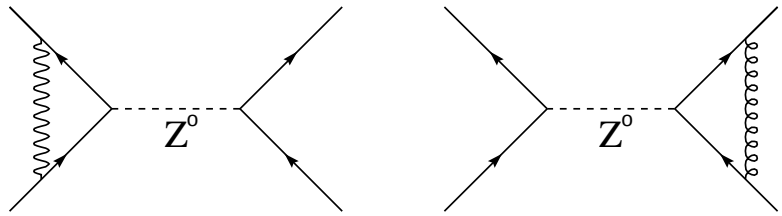

Figure 1.3: Leading order QED and QCD vertex corrections.

calculated using the program ZFITTER [25]. The result is a relative 0.17% decrease in the asymmetry. The measured value of A_b will be corrected for this in Section 5.5.3.

The main result of the propagator corrections is in modifying $\sin^2\theta_W$. Given the fact that A_b is very insensitive to changes in $\sin^2\theta_W$ (see Table 1.3), the propagator corrections result in a negligible change in A_b.

The final state gluon radiation affects only the decay of the Z^0. The width of the Z^0 is modified by the factor:

$$\approx 1 + \frac{\alpha_s}{\pi} + 1.4\left(\frac{\alpha_s}{\pi}\right)^2 + \ldots\,, \tag{1.26}$$

where α_s is the strong coupling constant. Fortunately, the measurement of A_b is not sensitive to these types of modifications because all multiplicative factors cancel in the ratio of cross-sections. Another effect of the gluon radiation is in modifying the topology of Z^0 decay – it smears the quark axis. Since the measurement of A_b relies on reconstruction of the b-quark direction, the FSR correction to the measured value of asymmetry has to be made. It is important to note that the QCD corrections for the unpolarized (A^b_{FB}) and polarized ($\tilde{A}^b_{FB}$) asymmetry are identical [52]. The first order

calculations of the QCD corrections to the asymmetry for the massive quarks and second order corrections for the massless quarks are available in the literature. Good reviews of the QCD corrections to the asymmetry can be found in [53]. In the current analysis the first order $\cos\theta$-dependent QCD corrections for the massive quarks were used [54]. The procedure is described in detail in Section 5.4.

Chapter 2

Experimental Status

2.1 How to Measure A_b

Over the last years several measurements of the b-quark asymmetry have been performed mainly at CERN and SLAC. In order to measure an asymmetry, the direction of the original quark has to be extracted from the data. The usual steps of the analysis are: (a) select a sample enriched in $b\bar{b}$ events (tag), (b) reconstruct the quark axis (thrust or jet axis) and (c) decide on the direction of the b quark ("forward" or "backward" event). In the following sections different techniques for asymmetry measurements are described.

2.1.1 A_b with Leptons

This method relies on the semileptonic decay channels $b \to X + l$. Two variables, the total momentum of the lepton, p, and the component of the lepton momentum transverse to the direction of the associated jet, $p_\perp$, are used to tag $b\bar{b}$ events. Hard b fragmentation results in high momentum of the B hadron and thus high momentum of the produced lepton. Because the B is so massive, decay products have a relatively large momentum in the B rest frame, giving a high transverse momentum in the laboratory frame. Leptons produced by the cascade processes, $b \to c \to l$, have lower

p and $p_\perp$, while direct $c \to l$ decays have lower $p_\perp$, but relatively high total momentum.

The charge of the lepton is used to distinguish between the quark and antiquark direction which makes this measurement quite sensitive to $B^0\bar{B}^0$ mixing. Mixing reduces the measured asymmetry by a factor $(1-2\chi)$:

$$A_{FB}^{b,mix} = (1-2\chi)A_{FB}^{b} \ , \tag{2.1}$$

where χ is the average mixing parameter, measured at the Z^0 pole for semileptonic B hadron decays. Leptons from the different decay chains can contribute to the sample [65] (also charge conjugate decay modes):

- $b \to l^-$ with asymmetry $A_{FB}^{b,mix}$
- $b \to \tau^- \to l^-$ with asymmetry $A_{FB}^{b,mix}$
- $b \to c \to l^+$ with asymmetry $-A_{FB}^{b,mix}$
- $b \to \bar{c} \to l^-$ with asymmetry $A_{FB}^{b,mix}$
- $c \to l^+$ with asymmetry $-A_{FB}^{c}$
- $b \to J/\psi \to l$ with zero asymmetry.

At the SLD the maximum likelihood method is used to measure A_b and A_c simultaneously. The most current SLD results [26] are:

$$muons: \quad (1994-95) \quad A_b = 0.880 \pm 0.109(stat) \pm 0.044(syst)$$

$$A_c = 0.609 \pm 0.151(stat) \pm 0.068(syst)$$

$$(1993) \quad A_b = 0.93 \pm 0.20(stat) \pm 0.10(syst)$$

$$A_c = 0.48 \pm 0.29(stat) \pm 0.19(syst)$$

$$electrons: \quad (1994-95) \quad A_b = 0.860 \pm 0.107(stat) \pm 0.049(syst)$$

$$A_c = 0.656 \pm 0.167(stat) \pm 0.089(syst)$$

$$(1993) \quad A_b = 0.90 \pm 0.19(stat) \pm 0.12(syst)$$

$$A_c = 0.45 \pm 0.36(stat) \pm 0.31(syst)$$

$$combined: \quad (1993-95) \quad A_b = 0.877 \pm 0.068(stat) \pm 0.046(syst)$$

$$A_c = 0.614 \pm 0.104(stat) \pm 0.074(syst).$$

The main systematic errors come from the limited Monte Carlo statistics, modeling

of the transverse momentum distribution and $B^0\bar{B}^0$ mixing.

2.1.2 A_b with Kaons

This is a new technique that uses charged kaons from the $B \to D \to K$ decay chain for $B/\bar{B}$ separation, requiring good particle identification, and providing high statistics and analyzing power. So far, the SLD is the only detector that has reported the measurement of A_b using the kaon tag [63]. The SLD uses charged kaons with momentum of $3 - 20\ GeV$, identified by the Cherenkov Ring Imaging Detector. The $\pi \to K$ mis-identification rate is calibrated using 1 prong and 3 prong τ decays that have well known small rates of $K^{\pm}$ production. The preliminary SLD result using 1994-1995 data is:

$$A_b = 0.91 \pm 0.09(stat) \pm 0.09(syst) \tag{2.2}$$

where the biggest contributions to the systematic error come from the kaon mis-identification calibration and uncertainty in the $K^{\pm}$ yield from B and D decays. The fact that the kaon tag is done in two hemispheres separately allows a calibration of the analyzing power from the data.

2.1.3 A_b with Momentum-Weighted Charge

Originally proposed almost twenty years ago [57] under the name of "Jet Charge", this method uses the combined charge of all tracks to distinguish between the quark and antiquark direction. The plane perpendicular to the event thrust axis defines two

hemispheres. The momentum-weighted charge of a hemisphere is defined as:

$$Q_{1(2)} = \sum_{tracks} q_i \left|\vec{p_i} \cdot \hat{T}\right|^{\kappa} , \tag{2.3}$$

where $\hat{T}$ is the unit vector in the direction of thrust axis, q_i and p_i are the charge and momentum of the i-th track, and the sum is taken over the tracks in the first (second) hemisphere. The exponent κ is used to maximize the probability of the correct assignment of the b quark direction. The charge of the hemisphere containing the b quark is on average negative, while the average $\bar{b}$ hemisphere charge is positive. The charge separation between the two hemispheres can be used to sign the thrust axis of the event:

$$\Delta Q = Q_1 - Q_2 = \sum_{tracks} q_i \left|\vec{p_i} \cdot \hat{T}\right|^{\kappa} sign(\vec{p_i} \cdot \hat{T}) \ . \tag{2.4}$$

The thrust axis direction is selected to make ΔQ negative. The signed thrust axis distribution for tagged SLD data is shown in Figure 2.1 for left- and right-handed events separately. The shaded region represents the light quark background, estimated from the Monte Carlo.

There are two kinds of tracks that dilute the measurement:

• fragmentation tracks that on average carry no or opposite asymmetry and have lower momentum than tracks from B hadron decays, and

• low momentum B–decay tracks that go in the direction opposite to the parent hadron.

Weighting the particle charge with its momentum reduces the effect of low momentum

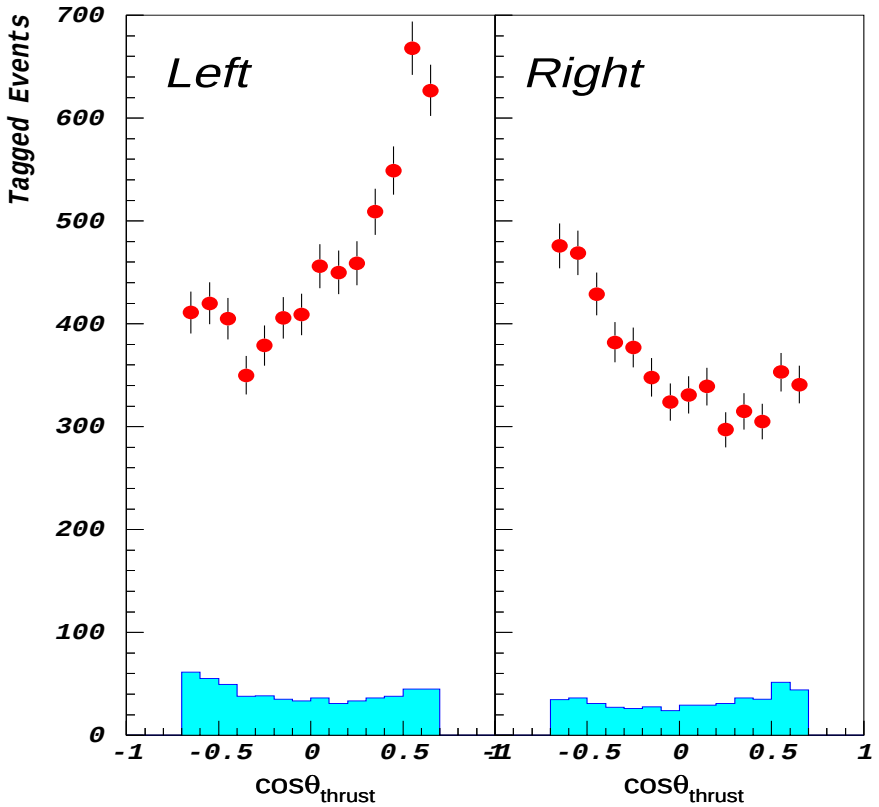

Figure 2.1: Thrust axis distribution signed with the momentum-weighted jet charge for left- and right-handed events. Dark circles are the tagged data events. Monte Carlo – estimated background is shown by the shaded region.

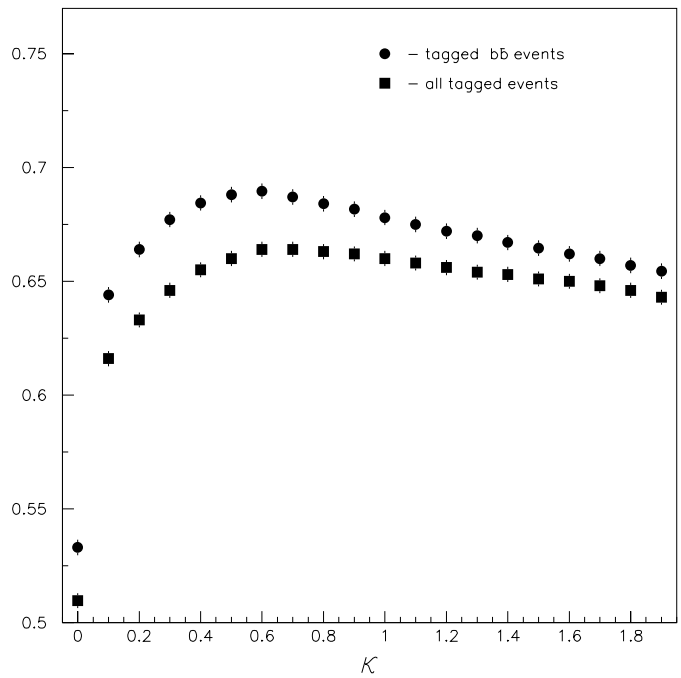

Figure 2.2: The probability of correct axis signing, $p^{correct}$, as a function of κ. Here $p^{correct}$ was estimated from the Monte Carlo.

tracks and increases the probability of correct axis signing, $p^{correct}$. Figure 2.2 shows $p^{correct}$ as a function of κ for all tagged events and the $b\bar{b}$ subsample.

Most of the recent measurements use a self-calibrating technique (see Section 5.3) to measure $p^{correct}$ from the data. This technique, together with the large statistics of the sample, makes the jet-charge method one of the most attractive for asymmetry measurements.

2.2 Current Status

Since the beginning of LEP and SLC operation, many asymmetry measurements have been reported by the SLD [61], [63] and by LEP detectors [64] - [71]. The most current results, as reported at the Moriond 1997 Conference [26], [27], are summarized in Figure 2.3. The measurement of A_b described in this thesis is not included in the plot.

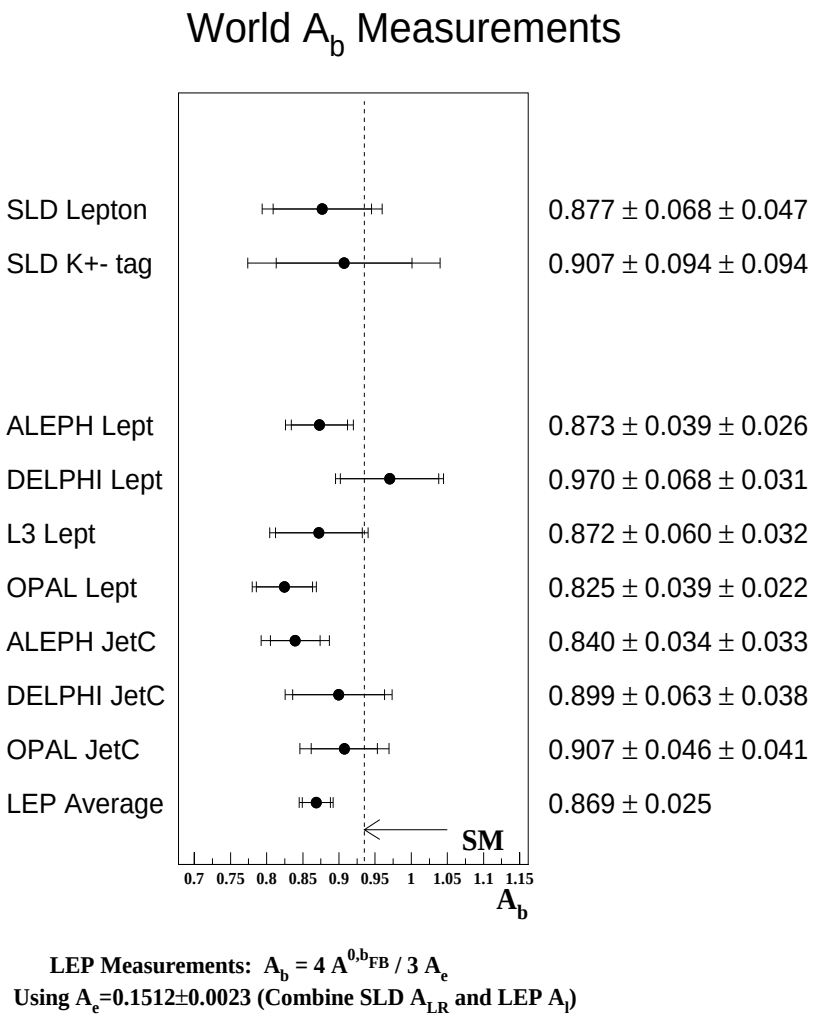

Figure 2.3: World A_b measurements (Moriond 1997).

Chapter 3

Experimental Apparatus

The analysis presented in this thesis uses data collected at the SLAC Large Detector (SLD) during the period 1993 – 1995. The SLAC Linear Collider (SLC) provides positron and polarized electron beams that collide inside the SLD at a center of mass energy of 91.2 GeV. The collision rate is 120 Hz. The polarization of the electron beam is measured by a Compton polarimeter.

3.1 SLAC Linear Collider

The SLC [28] consists of a two mile long linear accelerator (LINAC) and two arcs that separate electron and positron bunches and then steer them into the interaction region. Microwaves, generated by 244 65 MW klystrons [29], are directed into the resonant structure of the accelerator pipe, producing a standing wave with an oscillating electric field along the beam direction. Injected into the cavity at the appropriate phase, both electron and positron beams will experience the accelerating field. The transverse size of the beam in the LINAC is controlled by the periodic structure of quadrupole and sextupole magnets.

The layout of the SLC is shown schematically in Figure 3.1. The main elements shown are: the polarized electron source [30], the damping rings, the LINAC, the

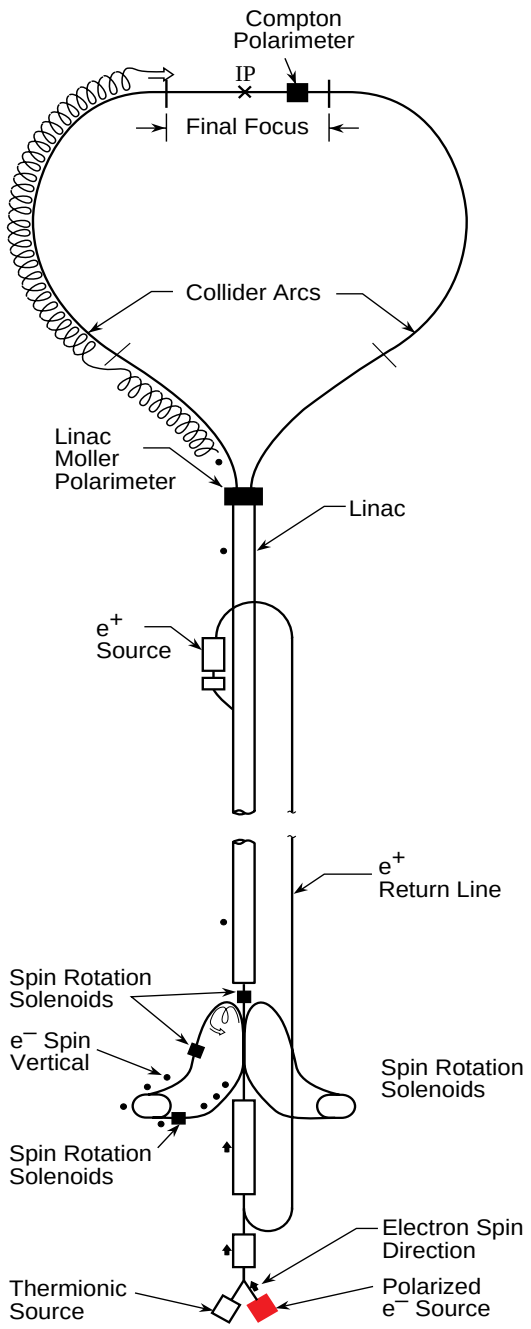

Figure 3.1: The SLAC Linear Collider. The direction of the electron spin is shown by the arrows (dots for vertical spin orientation).

collider arcs, and the Compton polarimeter. The electron spin direction is shown by the arrows and dots (if vertical). A strained GaAs photocathode is used to produce polarized electron beams [31].

The SLC acceleration cycle starts with generation of two electron bunches that are accelerated to 1.19 GeV and transported into the North damping ring. After 16.7 ms of "cooling", both electron beams are injected into the LINAC, lead by the positron bunch left from the previous cycle (see below). First two beams (e^+ and e^-) propagate to the end of the LINAC and are accelerated to an energy of 46.6 GeV. A dipole magnet sends electrons into the north and positrons into the south arc. Particles lose about 1 GeV of energy in the arcs due to synchrotron radiation. Before colliding at the interaction point (IP), bunches are focused by a set of superconducting quadrupoles. The electron beam polarization is measured by the Compton polarimeter [32] after the collision. The components of the Compton polarimeter are shown in Figure 3.2.

The third bunch in the train, called the "scavenger bunch", is accelerated to an energy of 31 GeV and then is extracted from the LINAC and sent to a tungsten target. Positrons, produced in an electromagnetic shower, are collected, accelerated to 200 MeV and then transported to the injector through the e^+ return line. After an additional boost to 1.19 GeV, positrons are guided into the South damping ring to provide an e^+ bunch for the next SLC cycle.

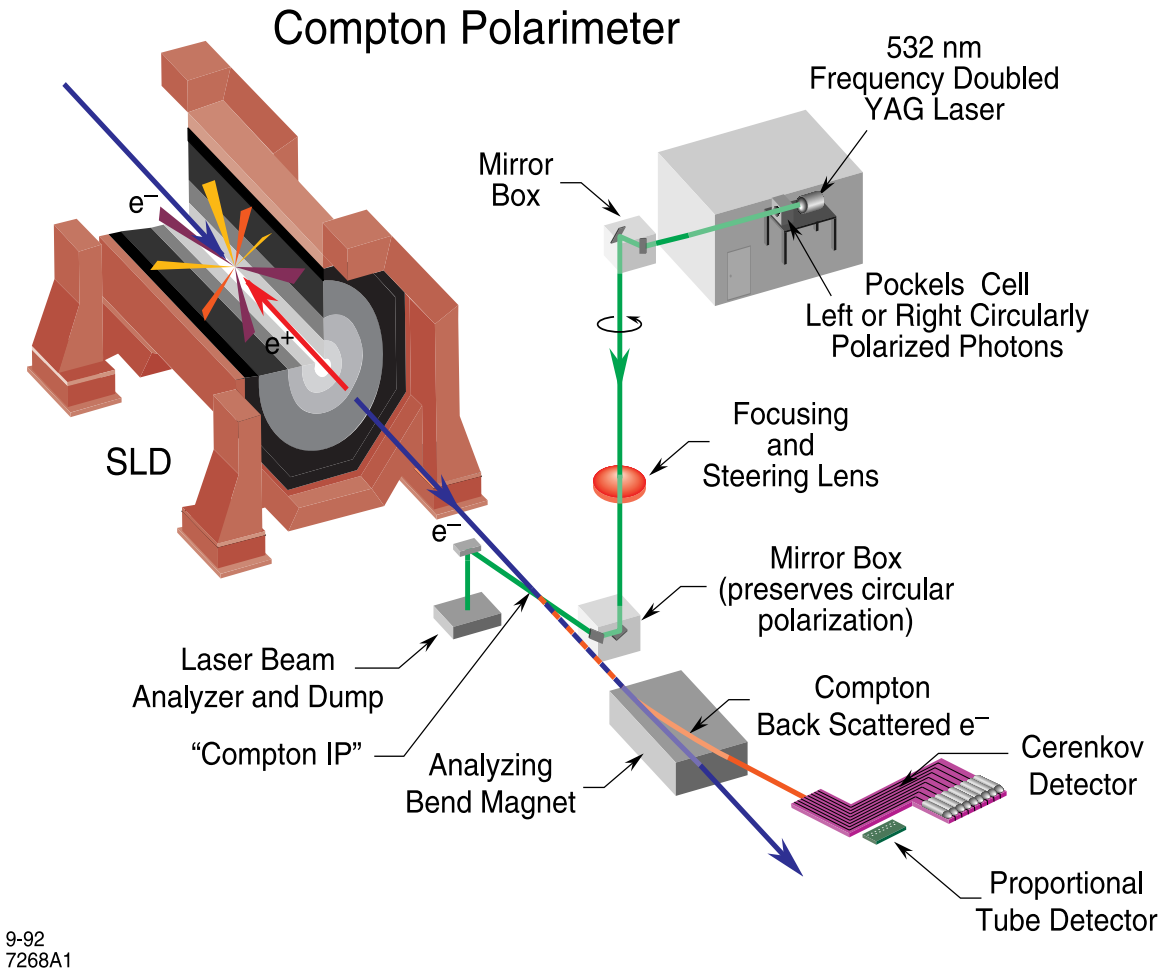

Figure 3.2: Elements of the Compton polarimeter.

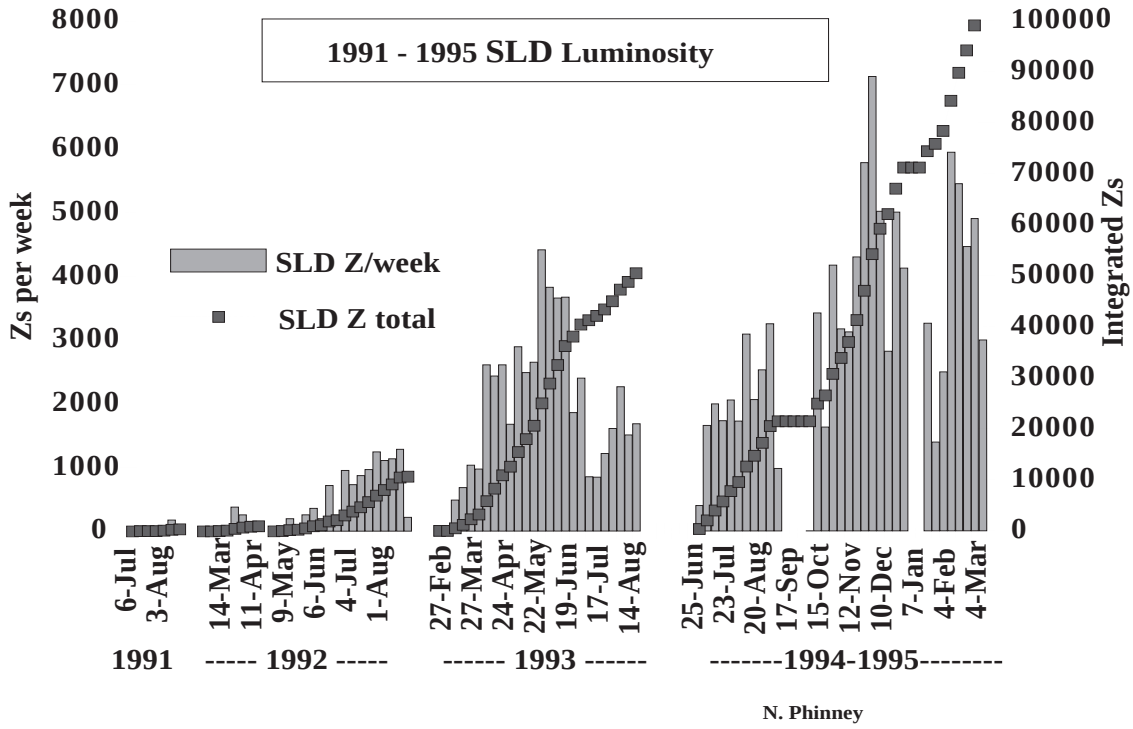

Figure 3.3: History of the SLC luminosity.

3.1.1 Performance

Since the beginning of its operation in 1989, the SLC had shown improvement in luminosity, reliability, and electron beam polarization. The SLC luminosity history is shown in Figure 3.3.

A number of upgrades were performed on the SLC between the 1993 and 1994-1995 runs. The damping ring vacuum chambers were replaced to reduce the impedance [33]. Introduction of an "overcompression" technique [34] allows shorter bunches in the transport line between the damping rings and the LINAC, reducing the energy spread. A final focus optics upgrade was designed to reduce chromatic effects [35].

Table 3.1: Important SLC parameters.

Parameter	1993	1994-1995
L (cm^2/s)	3.8×10^{29}	6.0×10^{29}
$N_{e^\pm}$/bunch	3.0×10^{10}	3.5×10^{10}
P_e	$63.0 \pm 1.1\%$	$77.4 \pm 0.6\%$
σ_E/E	0.25%	0.12%
σ_x	2.6 μm	2.3 μm
σ_y	0.8 μm	0.5 μm

The important SLC characteristics are summarized in Table 3.1.1.

The SLC beam polarization as a function of the number of collected Z^0 is shown in Figure 3.4. A bulk GaAs photocathode was used in the 1992 run yielding a polarization at the IP of 22%. In 1993 a strained GaAs cathode with a thickness of 0.3 μm was installed, resulting in significant increase in polarization (63%). For the 1994-1995 run, an even thinner strained GaAs cathode was used (0.1 μm) raising the average measured polarization to 77.4%.

3.2 SLAC Large Detector

The SLAC Large Detector (SLD) [36] is a multi-purpose detector, designed to operate at the Z^0 resonance. A perspective cut-away view of the SLD is shown in Figure 3.5. The first physics run was done in 1992 with all systems in place and functioning. Figure 3.6 shows the layout of the SLD subsystems including: the vertex detector, the drift chamber, the Cherenkov ring imaging detector, the liquid argon calorimeter and the warm iron calorimeter. Also shown are the magnet coil, providing a uniform

Figure 3.4: History of the electron beam polarization.

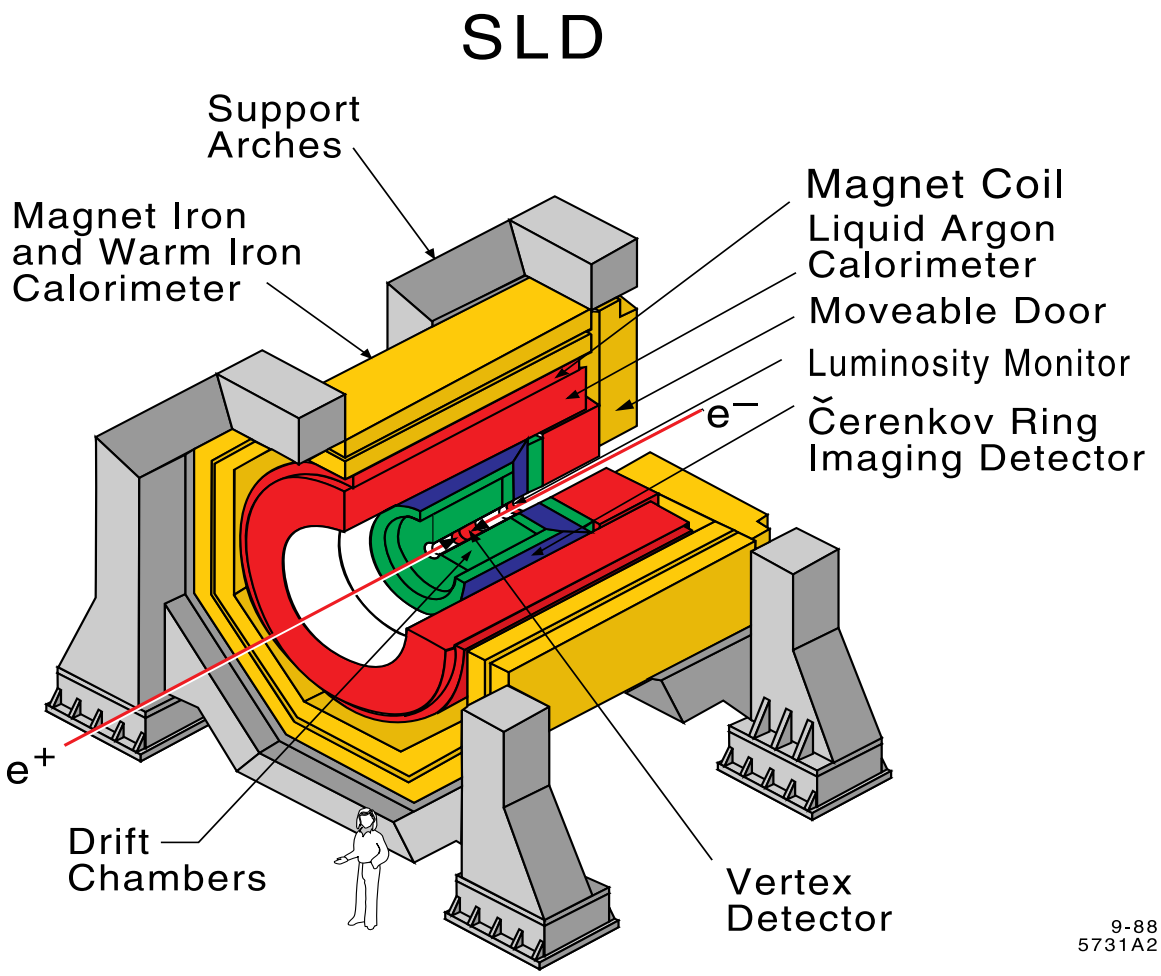

Figure 3.5: Perspective view of the SLD. South door (endcap) is not shown for clarity.

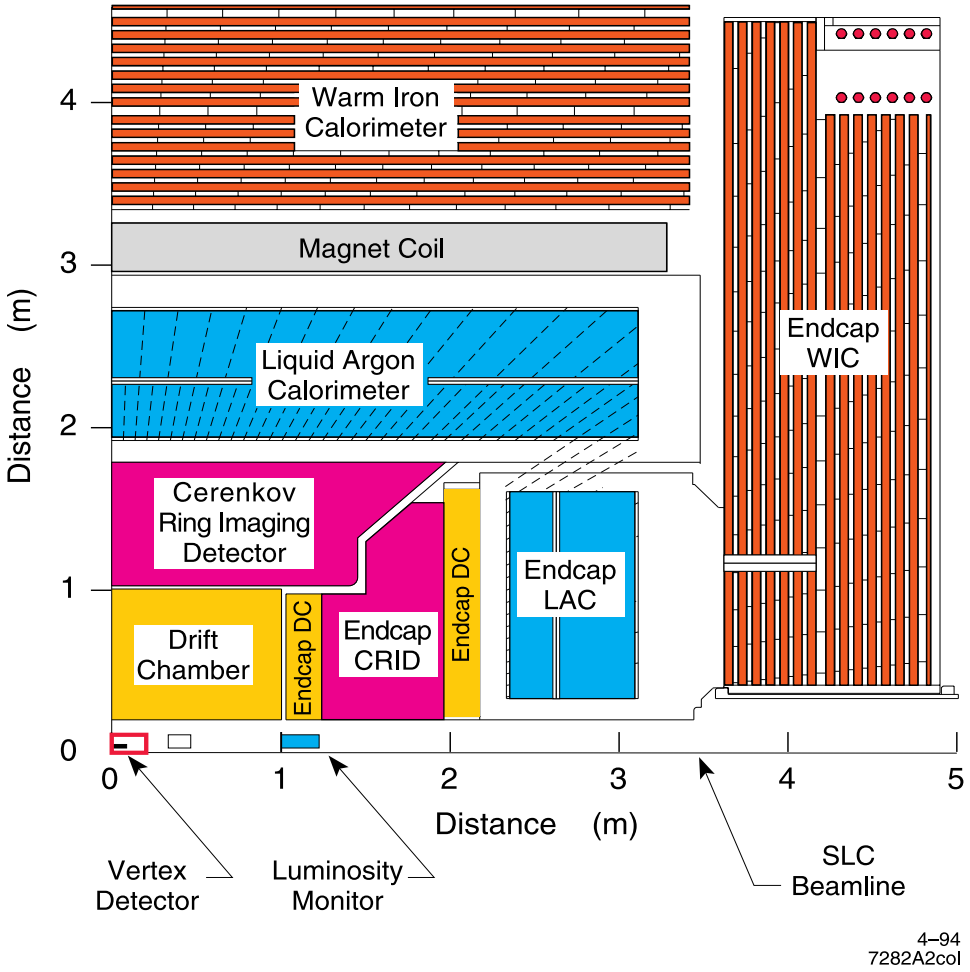

Figure 3.6: Cross-section of an SLD quadrant.

magnetic field of 0.6 T, and the luminosity monitor. Most SLD subsystems are divided into a barrel and two endcap parts.

3.2.1 Vertex Detector

The system that is closest to the IP is the SLD Vertex Detector (VXD) [37]. Based on Charge-Coupled Devices (CCDs), the VXD provides precision tracking of the Z^0 decay products.

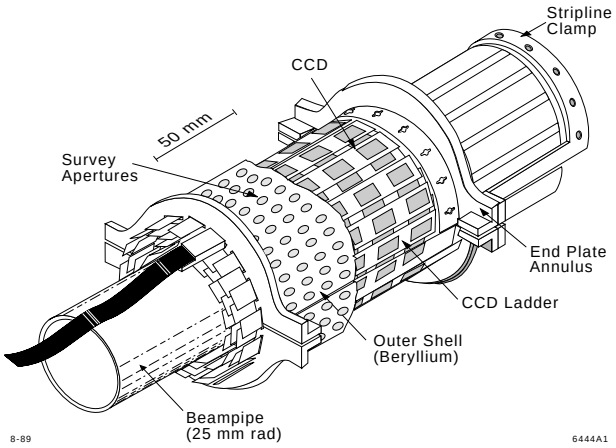

Figure 3.7: Perspective view of the SLD Vertex Detector.

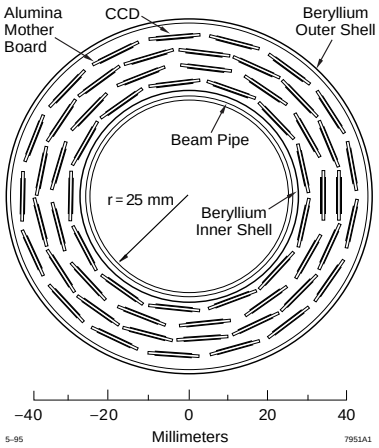

Figure 3.8: Cross-section view of the VXD.

The Vertex Detector uses 480 CCDs, mounted four on each side of 250 μm thick alumina motherboards, called ladders. Neighboring CCDs on a ladder have overlap of ≈ 1 mm allowing the use of charged particle tracks for internal alignment.

In general a CCD is a 2-dimensional array of potential wells [38]. When a charged particle passes through the device, the released electrons are collected in the wells. The CCDs used in the SLD Vertex Detector are metal-oxide-semiconductor (MOS) devices with a 2-dimensional array of 237,000 pixels each. The readout is done by shifting rows of charges, one at a time, into a special row on the edge of the CCD (R register). Charges in the R register are then shifted one at a time to an on-chip FET.

The perspective view of the VXD is shown in Figure 3.7. 60 ladders are organized in four coaxial layers around the beampipe (Figure 3.8), supported by beryllium endplates. To reduce the CCD dark current, the vertex detector was operated at a temperature of 195 K. The VXD is surrounded by a low density foam cryostat and is

Table 3.2: VXD design parameters.

Number of CCDs	480
Pixels/CCD	400×600
Pixel size	22 μm$\times$22 μm
Readout time	160 ms (19 beam crossings)
Radius Layer 1	2.96 cm
Radius Layer 2	3.36 cm
Radius Layer 3	3.76 cm
Radius Layer 4	4.16 cm
Radiation thickness	1.15%/layer
Average hits per track	2.3
Two-hit coverage	$\lvert\cos\theta\rvert < 0.75$
One-hit coverage	$\lvert\cos\theta\rvert < 0.82$

cooled by cold N_2 gas flow. The important design parameters of the VXD are summarized in the Table 3.2.1. After installation, one ladder with a broken connection was discovered. No significant degradation of performance due to radiation damage was observed after three years of exposure.

The VXD utilizes a Central Drift Chamber (CDC) aided reconstruction scheme. The CDC track is extrapolated back to the IP and the track error matrix is used to define the search region for VXD hits to be linked with the track. The VXD reconstruction works almost the same way for the data and the Monte Carlo. The only difference is in the input raw data bank. In the Monte Carlo, the positions of the hits have to be converted to the real CCD geometry, smeared, digitized and presented to the reconstruction as CCD pixels.

The flow chart of the VXD offline reconstruction is shown in Figure 3.9. There are

five major steps in the process.

The first step (VXRECEX) is the primary extrapolation in which the Central Drift Chamber (CDC) tracks are extrapolated to all layers of the VXD. The track parameters and errors on each CCD plane are stored. During Pass 1, extrapolated CDC tracks are required to go through the IP. This constraint is waived for Pass 2.

In the second step (VXRECCL) pixels are grouped together in clusters. The standard reconstruction only does this clustering on CCD's which have been intersected by an extrapolated track. Only about half the CCD's have this track extrapolation, so the time required for doing clustering is greatly reduced.

The third step (VXRECLK) is called the linking stage. In this step the CDC track is constrained to go through a cluster within the primary error ellipse. The track is refit with this constraint and extrapolated to the inner layers. A smaller secondary error ellipse is formed and a search is made for clusters inside this error ellipse. Any track with at least one primary cluster and one secondary cluster is a link candidate. A secondary extrapolation is performed for every cluster inside every primary error ellipse on all layers for every track. This leads to many track candidates consisting of a CDC track and possible VXD clusters. Subsets of possible links are eliminated and all possible links are stored. Tracks that do not have VXD links at this stage are re-processed with the Pass 2.

The fourth step (VXREC1H) consists of looking for track candidates with only a single associated VXD cluster. This is done only for tracks without a multiple VXD

cluster track candidate. Tracks are constrained to go through the interaction point, and clusters near the track-CCD intersection are considered good track candidates.

In the fifth and final step, (VXFPHV) all possible track candidates are sorted by their quality and the best candidate(s) are stored.

Linking VXD hits with the CDC tracks improves the overall momentum resolution but, more important for the current analysis, it also improves the impact parameter resolution. In the limit of low multiple scattering, the impact parameter resolution can be measured using $Z^0 \to \mu^+\mu^-$ events. In the SLD offline reconstruction, the IP position in the $x - y$ plane is determined by averaging the primary vertices of ≈ 30 hadronic events. Figure 3.10 shows the distance of closest approach of muons to the fit IP position as well as a Gaussian fit. For the lower momentum tracks, the $x - y$ impact parameter error can be parameterized as

$$\sigma_b = \sqrt{(11\mu m)^2 + (70\mu m/(p\,|\sin\theta|^{1.5}))^2}\ , \tag{3.1}$$

where p is the momentum of the particle and θ is the polar angle. The second term accounts for multiple scattering.

3.2.2 Central Drift Chamber

The SLD Central Drift Chamber (CDC) [39] is used to track the charged products of the Z^0 decays. The CDC is 2 m long and extends from 20 cm to 100 cm in the radial direction. It is placed in a uniform magnetic field of 0.6 T and consists of 10 superlayers of drift cells formed by wires. Cells are approximately 6 cm wide and 5 cm

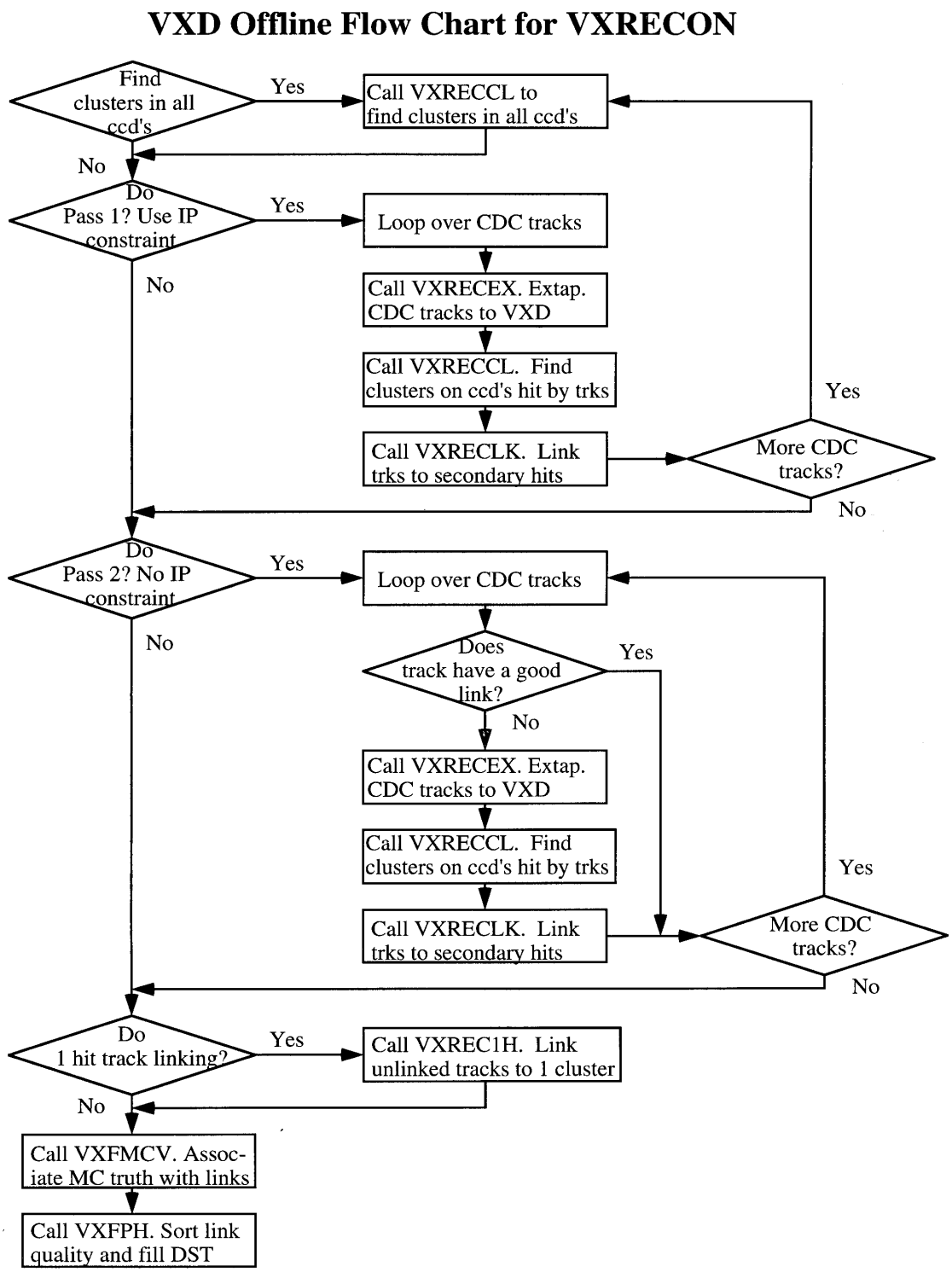

Figure 3.9: VXD Offline flow chart for VXDRECON.

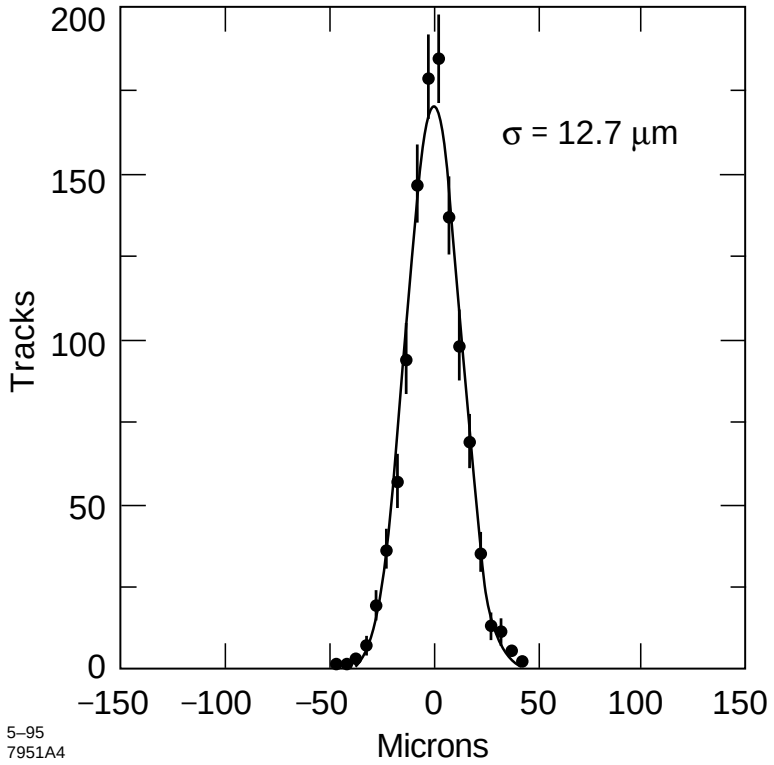

Figure 3.10: Impact parameter of tracks in $Z^0 \to \mu^+\mu^-$ events with respect to the average IP position determined from hadronic events, also shown fit to a Gaussian.

high. Each superlayer is one cell thick. The CDC geometry is shown in Figure 3.11. Each cell has ten sense wires, but only eight of them are digitized. Field wires, held at a voltage of ~ 5 kV, together with the field shaping (guard) wires create a uniform electrical field across the drift cell. The region of a strong nonuniform electric field between the sense and the guard wires is used to amplify the signal by creating a cascade. Ionization charge, left by a charged particle, drifts across the cell and is deposited on the nearest sense wire. The CDC gas is a mixture of 75% CO_2, 21% Ar, 4% Isobutane and 0.2% H_2O, providing proportional gain, low dispersion and a drift velocity of 7.9 μm/ns in the ≈ 0.9 kV/cm electrical drift field. The gas is kept at the constant temperature of 20°C and at atmospheric pressure. Sense wires are 25 μm in diameter, made of gold plated tungsten and held at 100 g of tension. Other wires are made of 150 μm gold plated aluminum and held at a tension of 500 g for the field wires and 400 g for the guard wires.

The innermost superlayer is parallel to the beam ("Axial"). The next superlayer is tilted at an angle of +42 mrad with respect to the beam to provide stereo information ("Stereo layer"). The next superlayer is again a stereo layer, but tilted at −42 mrad. Then the pattern is repeated. There are four axial layers (including the outermost) and 6 stereo layers in the CDC.

Electrical signals are read out from both ends of the sense wire. Pulses are sampled and digitized by the electronics mounted on the endplates of the CDC. Digital information, representing the signal waveform, is then transmitted through the fiber optic

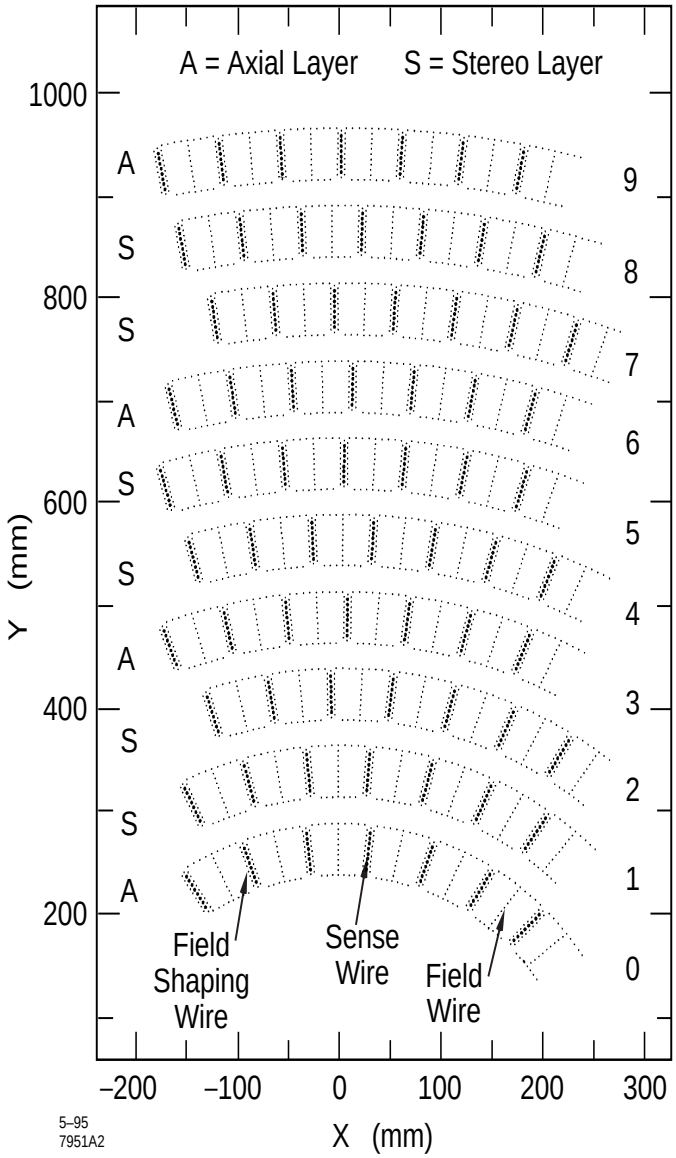

Figure 3.11: Central Drift Chamber geometry.

cables to the fastbus Waveform Sampling Modules (WSM). For each pulse the beginning time, the end time, the amplitude, the width and the total charge are extracted. These numbers are recorded on the SLD tapes and used later for the track reconstruction. The fact that information from both ends of the sense wires is recorded makes it possible to determine the position of the hit along the wire using the asymmetry in the charge division. The resolution of this method is ≈ 5 cm.

The CDC reconstruction starts by applying cuts on the drift time and the total collected charge to the raw hits to remove noise. Track segments within a superlayer, called vector hits (VHs), are identified as sets of four to eight hits within a cell that are consistent with belonging to the same helix. The next stage of reconstruction, called pattern recognition, combines vector hits to form candidate tracks. First VHs from the axial layers are selected by requiring that they belong to the same circle. Then the information from the stereo layers is added. Track candidates are sorted by length and quality and the best VH combination is passed to the fitter. The fitter makes an initial estimation of the track parameters. Then the track is propagated through the detector, taking into account nonuniformity of the magnetic field, energy losses and multiple scattering. The final set of track parameters is obtained by minimizing the χ^2 of the fit.

Drift distance resolution for the central part of the cell is about 100 μm and is limited by diffusion. The momentum resolution, derived from the reconstructed

cosmic ray tracks that pass near the center of the CDC, can be parameterized as:

$$dp/p^2 = \sqrt{(0.0050)^2 + (0.010/p(GeV/c))^2}\ , \tag{3.2}$$

where p is the component of the momentum transverse to the beam axis.

3.2.3 Cherenkov Ring Imaging Detector

The Cherenkov Ring Imaging Detector (CRID) [40] is the particle identification system for the SLD. When a charged particle passes through a medium at a speed exceeding the speed of light in the material, it produces a cone of Cherenkov light with an opening angle of

$$\theta = \cos^{-1}\left(\frac{1}{\beta n}\right), \tag{3.3}$$

where n is the index of refraction of the material and β is the speed of the particle divided by the speed of light in the vacuum.

The CRID uses this principle to measure the velocity of charged particles. In order to extend the momentum range of particle identification, two radiators are used in the CRID: a thin liquid radiator (C_6F_{14}) for lower energy particles and a deepeer gaseous radiator (C_5F_{12}) for higher energy particles. The layout of the barrel CRID is shown in Figure 3.12. Spherical mirrors focus the Cherenkov cones to form circles of light which are measured with a time-projection chamber (TPC), positioned between the two radiators. The TPCs are filled with a drift gas that is a mixture of ethane, argon and Tetrakis Dimethyl Amino Ethylene (TMAE). When hit by a photon from

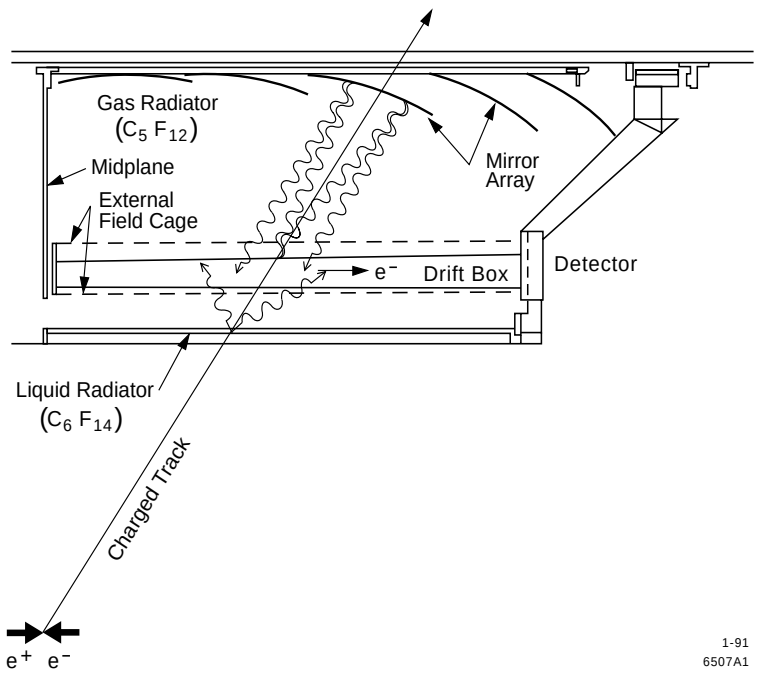

Figure 3.12: Schematic of the barrel CRID.

Cherenkov light, the TMAE releases a single electron. The electron drifts with a constant velocity in an electric field of the TPC and is detected by wires at the chamber's end. The z coordinate of the hit is measured by the drift time and the transverse coordinate by the position of the particular wire. Although the CRID is not used in the current analysis, it is one of the most important systems for other SLD measurements, like A_b with leptons and kaons.

3.2.4 Calorimetry

The SLD measures the energy deposition of the charged and neutral particles in a Liquid Argon Calorimeter (LAC) [41] and Warm Iron Calorimeter (WIC) [42].

The LAC is divided into a barrel section and two endcaps. The LAC barrel is

positioned inside the SLD magnet coil and extends from 177 cm to 291 cm radially, including the cryostat. The length of the barrel section is 620 cm. The LAC is made out of layers of parallel lead plates separated by plastic spacers and placed in liquid argon. A high voltage of 2000 V is applied to every second layer of lead. Particles that pass through the lead produce showers of lower-energy secondaries that ionize argon. Ionization charges drift in the electric field and are collected on the high-voltage tiles. Several tiles are connected together electrically to form a projective tower. Each tower is connected to a single amplifier in order to measure the charge deposited in the tower, and towers are assembled into modules. A typical set of the barrel modules is shown in Figure 3.13.

The LAC is segmented into two electromagnetic and two hadronic layers, EM1, EM2, HAD1, HAD2. Properties of the LAC layers are shown in Table 3.2.4. The segmentation was chosen so that approximately half of the electromagnetic shower energy is deposited in EM1 and half in EM2 with a minimal leakage into the hadronic section. The azimuthal and polar angle segmentation is ~ 33 mrad for the electromagnetic and ~ 66 mrad for the hadronic section. The endcaps cover the region 8° to 35° with similar angular segmentation. The overall energy resolution in the LAC barrel is $\frac{15\%}{\sqrt{E}}$ for electromagnetic showers. In the endcap region the electromagnetic energy resolution worsens to $\frac{25\%}{\sqrt{E}}$ due to more material in front of the calorimeter.

The LAC is thick enough to absorb on average about 95% of the energy from the Z^0 decays. Located outside the SLD magnetic coil, the WIC is designed to measure

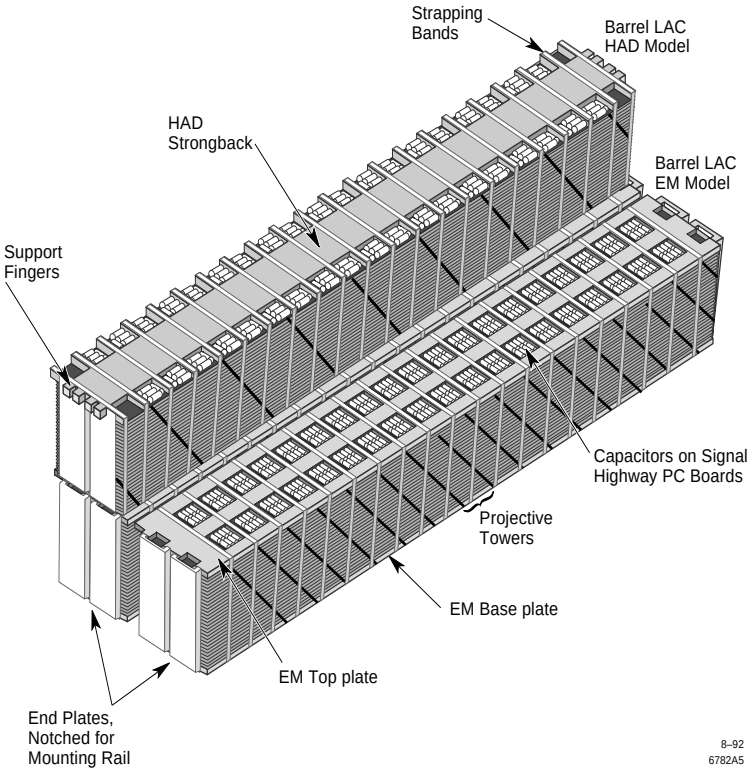

Figure 3.13: A typical set of barrel LAC modules.

Table 3.3: Properties of the LAC layers and WIC pads.

Layer	Rad. Length	Interaction Length	Angular Segmentation
EM1	6.0	0.24	33 mrad
EM2	15	0.60	33 mrad
HAD1	25	1.0	66 mrad
HAD2	25	1.0	66 mrad
WIC1	50	2.0	66 mrad
WIC2	50	2.0	66 mrad
Total	171	6.84	

the residual 5% of the energy, serve as mechanical support, and provide a magnetic flux return. It is constructed of 17 layers of plastic streamer tubes (Iarocci tubes) sandwiched between 5 cm thick steel plates. Tubes are equipped with long pickup strips used for muon identification and broad pads used for energy measurement. The WIC is not used for the current analysis.

Chapter 4

SLD Monte Carlo

A typical modern high energy physics detector, such as the SLD, is a complex apparatus requiring detailed computer simulation to understand fully its behavior. Simulation, usually employing Monte Carlo techniques, provides information about efficiencies, acceptances and resolutions of the detector subsystems. It is also crucial for determining analysis biases.

The SLD Monte Carlo is a combination of two parts: a physics simulation, which provides a model of the production and decay of the Z^0, and a detector simulation, which describes the propagation of particles through the detector volume and the response of the active systems.

4.1 Physics Simulation

The SLD uses a modified JETSET 7.4 [43] generator with LUND string fragmentation for simulation of $Z^0 \rightarrow hadron$ events. This generator includes initial- and final-state photon radiation, $\gamma - Z^0$ interference and a parton shower model [44] for the final-state gluon radiation. A very convenient feature of JETSET version 7.4 is that it preserves information about the parton shower evolution, including the direction of the initial quark from Z^0 decay. The latter is useful for estimating the QCD corrections to the

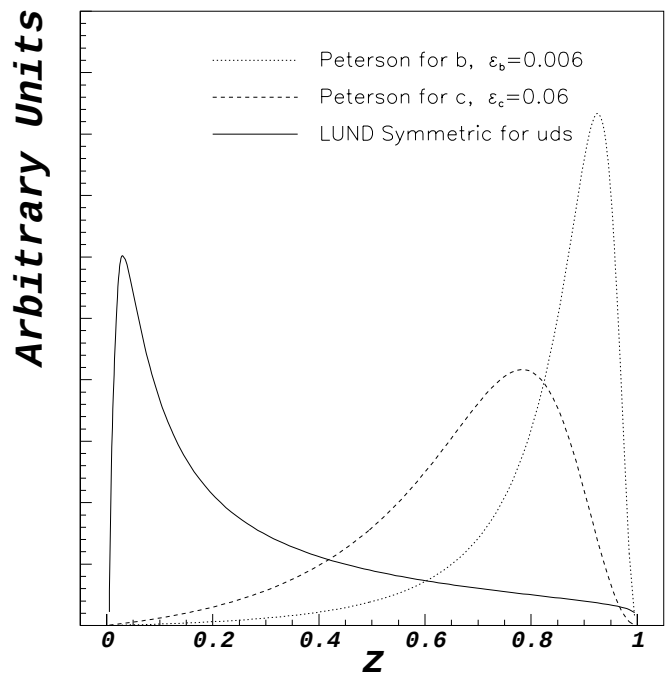

Figure 4.1: Peterson and LUND symmetric [43] fragmentation functions. The Peterson fragmentation function is given by: $f \sim z(1-z)^2/[(1-z)^2+\epsilon z]^2$, $z = \frac{(E+p_{||})_{hadron}}{(E+p)_{quark}}$. The parameter ϵ controls the average energy of the hadron.

measured asymmetry.

The Peterson fragmentation function [45] is used in the SLD Monte Carlo for b- and c-flavored hadrons, while light-flavored hadrons are produced with the default Symmetric LUND fragmentation. These functions are shown in Figure 4.1.

In the SLD Monte Carlo, events are generated with an electron beam polarization $P_e = 100\%$, while positrons are unpolarized. Equal number of left-handed and right-handed events are generated. In order to obtain the correct left-right asymmetry of the

sample, a fraction of the right-handed events, f_R, must be excluded from the analysis:

$$f_R = \frac{2\,|P_e|\,A_e}{1 + |P_e|\,A_e} \ . \tag{4.1}$$

However, the maximum likelihood analysis, presented in this thesis (Chapter 5), is not sensitive to the initial e^+e^- coupling and permits use of all the Monte Carlo statistics.

B-Hadron Decays

All unstable particles in the SLD generator are decayed by JETSET except for semileptonic B decays. This approach was taken because of the visible disagreement in the decay particle spectra between the JETSET decay model and data from CLEO and ARGUS [46] Instead of going through a complicated tuning process, an alternative program is now used to handle these decays. This program was chosen to be the CLEO decay simulation package. The CLEO model was integrated into the SLD environment and further tuned [47]. The D production spectra are shown in Figure 4.2.

The B hadron lifetimes in the Monte Carlo are set to 1.55 ps for B mesons and 1.10 ps for B baryons, yielding an average Monte Carlo B hadron lifetime of 1.51 ps.

Charmed Hadrons Decays

It is important to model the charmed hadron decays correctly since they affect the measurement in two ways. About 10% of the tagged B sample are $Z^0 \to c\bar{c}$ events. Also charmed hadrons appear as products of the cascade $b \to c$ process. The JETSET

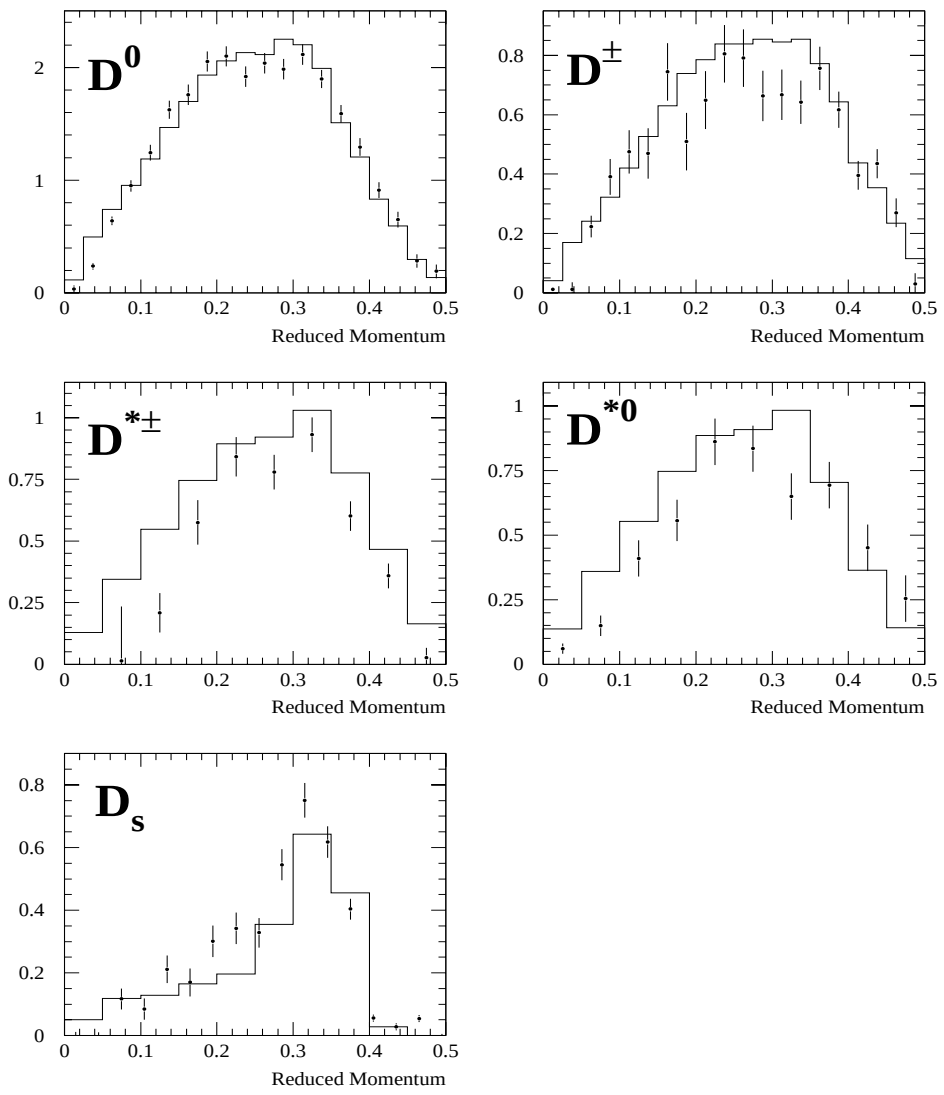

Figure 4.2: Shown are the D meson spectra from B decay for the CLEO decay model (histogram) and CLEO data.

Table 4.1: Charmed Meson Lifetimes.

Hadron	lifetime (ps)
D^+	1.057 ± 0.015
D^-	0.415 ± 0.004
D_s	0.467 ± 0.017

decay model is used for charmed hadrons in the SLD Monte Carlo, but the branching fraction tables were adjusted [47] for better agreement with the data from ARGUS, CLEO and MARK III. The charmed hadron lifetimes are set up according to the 1994 Particle Data Group [48] numbers and are shown in Table 4.1.

4.2 Detector Simulation

The purpose of the detector simulation is to provide a detailed model of the SLD response to the passage of particles through its volume. Not only physical interactions should be simulated, but also the efficiency, acceptance, and resolution effects must be properly modeled. The SLD uses a particle-detector simulation package called GEANT [49], version 3.21.

Detector simulation starts with a detailed description of the detector material, the magnetic field in the detector volume, and a list of all particles from the Z^0 decay generator. Long-lived particles, like K_s^0 and Λ^0, do not decay in JETSET, as they may interact with the detector material before decaying. Then GEANT propagates particles through the detector, modifying their paths as needed, and creating a list of

new particles formed by detector interactions.

The next step is to simulate the detector response. The idea is to have the Monte Carlo output in the same format as the real SLD data, keeping at the same time the true information about particles. Also the effects of the beam-related backgrounds and imperfect hardware have to be taken into account. This is primarily accomplished by overlaying random triggers onto generated Z^0 events. The random triggers are detector readouts taken randomly on a beam crossing approximately every 20 seconds. Any random trigger that also passes a Z^0 selection is not used. Information about the detector hardware status is also recorded with a random trigger and is used in the simulation to indicate any dead channels, high voltage status, and detector readout error. Signals from the random trigger are then merged with the simulated detector signals. For the vertex detector this appears as additional CCD hits. For the calorimeter the tower energies are simply added, but for the CDC, the two-hit resolution is applied. If two hits are received on the same wire with time separation Δt, then the probability of losing the later hit is $e^{-(\Delta t - 80ns)/25ns}$. Uncertainties in the positions of the tracking system elements are simulated by randomly smearing the position of particular CCD or CDC cells within the measured errors.

4.3 Data - Monte Carlo Comparison

Since the current analysis uses the topological reconstruction of the B-decay vertex for tagging and the momentum-weighted jet charge technique to determine the initial

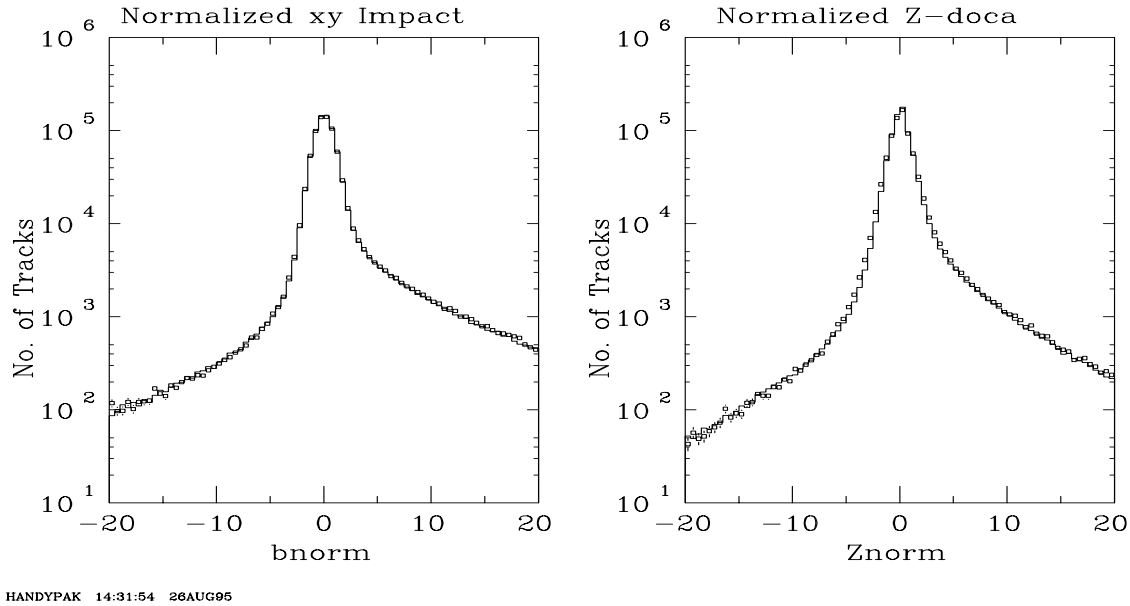

Figure 4.3: Normalized impact parameter distribution for the tagged events showing a visible discrepancy in normalized Z_{DOCA} between data (points) and Monte Carlo (histogram). Agreement in b_{norm} is much better.

b quark direction, the two most important parameters to be modeled correctly are the vertex resolution and the momentum spectrum of the charged tracks.

The distance of the closest approach of the track to the IP (DOCA), projected into the plane perpendicular to the beam axis, is called the XY impact parameter (b). The impact parameter divided by its error, σ_b, is called the normalized impact parameter: $b_{norm} = b/\sigma_b$. The Z coordinate of the track at the distance of closest approach is called the Z_{DOCA}. Figure 4.3 shows the data–Monte Carlo comparison for the normalized XY impact parameter and normalized Z_{DOCA}. To correct for the visible discrepancy in Z resolution, the Z_{DOCA} of every track that was linked to the

vertex detector was smeared:

$$Z_{DOCA}^{new} = Z_{DOCA}^{old} + \frac{g}{\cos\lambda} \ , \tag{4.2}$$

where λ is the dip angle of the track and g is a random number distributed according to the Gaussian probability with $< g >= 0$. Study showed [50] that the best agreement between the data and the Monte Carlo is achieved with $\sigma_g = 0.0016$ cm for the 1993 data, and $\sigma_g = 0.0020$ cm for 1994-1995 period.

The momentum-weighted jet charge technique relies on charged tracks to reconstruct the direction of the initial b quark, so it is important that momentum distributions of charged tracks from the Monte Carlo agree with the data. The first plot on Figure 4.4 shows the number of charged tracks per event as a function of the track's momentum. The suggested correction for the i-th bin: $(N_i^{MC}/N_i^{data} - 1)$ is shown on the second plot. It can be seen that the Monte Carlo produces more tracks than the data in every momentum region except $P_{tot} > 15\ GeV$. This discrepancy could be a result of momentum spectrum mismodeling for charged tracks from Z^0 decays. Figure 4.5 shows the charged track multiplicity distribution for the data and the Monte Carlo without corrections (first plot), and after corrections (second plot).

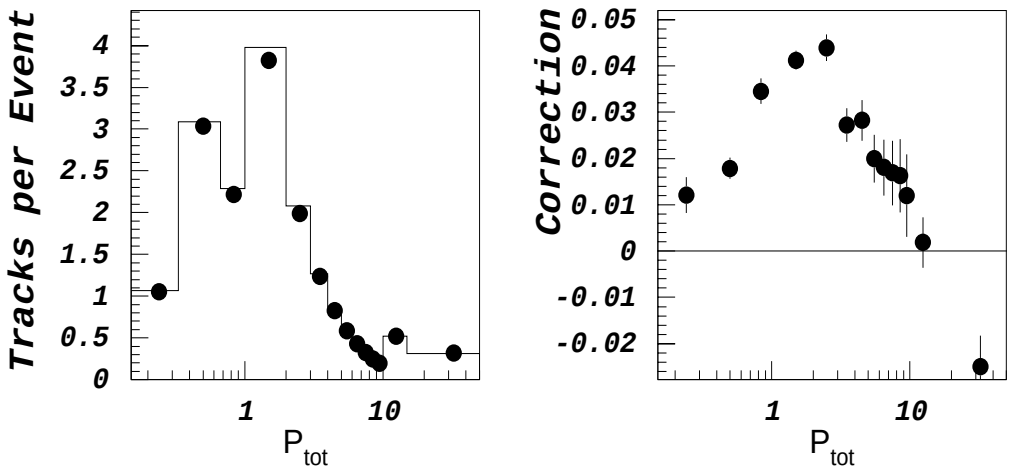

Figure 4.4: The first plot shows the number of charged tracks per event in different bins of the total momentum, P_{tot}. On the second plot, calculated tracking efficiency corrections are shown.

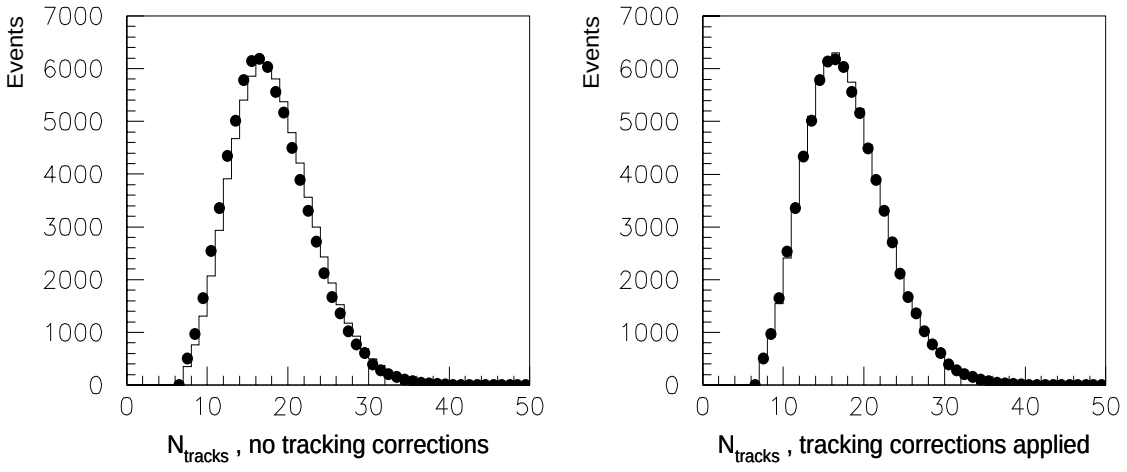

Figure 4.5: Charged track multiplicity for data (points) and Monte Carlo (histogram). The first plot shows a discrepancy between the data and the uncorrected Monte Carlo. For the second plot, tracking efficiency corrections were applied to the Monte Carlo.

Chapter 5

Analysis

5.1 Introduction

This chapter presents the actual measurement of the asymmetry A_b from 1993-95 data. To maximize the use of information, the maximum likelihood method was employed. The probability of the correct sign assignment for $Z^0 \to b\overline{b}$ events, $p^{correct,b}$, is estimated from the data. This procedure is described in detail in Section 5.3. The momentum-weighted charge of each event is used twice: to provide the sign of the thrust axis for the asymmetry measurement and to calculate the analyzing power of this measurement.

A B tag based on topological reconstruction of the mass of B-decay vertex was used to select the sample of $Z^0 \to b\overline{b}$ events. The estimated purity of the tagged sample at the selected cut is 91%. The double-tag method was used to calculate the purity of the sample from the data. The double-tag method [51] and B tagging results are presented in Section 5.5.2

5.2 Likelihood Function

In this analysis the maximum-likelihood technique was used to extract A_b from the data. The likelihood function used is:

$$P(event_i, A_b, A_c) = (1 - A_e P_e^i)(1 + \cos^2\theta_i) + 2(A_e - P_e^i)\cos\theta_i \tag{5.1}$$
$$[A_b \Pi_b^i (2p_i^{correct,b} - 1)(1 - \Delta_{QCD,b}^i) +$$
$$A_c \Pi_c^i (2p_i^{correct,c} - 1)(1 - \Delta_{QCD,c}^i) +$$
$$A_{bckg}(1 - \Pi_b^i - \Pi_c^i)(2p_i^{\text{“}correct'',bckg} - 1)] \ ,$$

where A_e is the electron asymmetry; P_e^i is the signed polarization measurement associated with the ith tagged event; $\cos\theta_i$ is given by the signed thrust axis $\hat{T}$; and the $\Pi_{b(c)}^i$ are the probabilities that the event was a $Z^0 \to b\overline{b}(c\overline{c})$ decay. The $\Delta_{QCD,b,c}^i$ are final-state QCD corrections, parameterized as a function of $cos(\theta_{thrust})$; A_{bckg} is the estimated background asymmetry from $u\overline{u}$, $d\overline{d}$, and $s\overline{s}$ decays of the Z^0; and $p^{correct,b,c}$ are correct-sign probabilities, parameterized as functions of the momentum weighted charge $|Q_{diff}|$. While $p^{correct,c}$ must be estimated from the Monte Carlo, $p^{correct,b}$ is calculated from the data with a much reduced model dependence.

5.3 Calibration of the Analyzing Power from the Data

5.3.1 Formalism

Let Q_b and $Q_{\bar{b}}$ be momentum weighted charges of the b and $\bar{b}$ hemispheres, as defined in Section 2.1.3. The only two assumptions we have to make at this stage are that Q_b

and $Q_{\bar{b}}$ are two uncorrelated variables which obey Gaussian statistics:

$$p(Q_b, Q_{\bar{b}}) = p(Q_b)p(Q_{\bar{b}}) \tag{5.2}$$

and

$$p(Q_b) = \frac{1}{\sqrt{2\pi\sigma_b^2}} e^{-(Q_b+Q_b^0)^2/2\sigma_b^2} \tag{5.3}$$

$$p(Q_{\bar{b}}) = \frac{1}{\sqrt{2\pi\sigma_{\bar{b}}^2}} e^{-(Q_{\bar{b}}-Q_{\bar{b}}^0)^2/2\sigma_{\bar{b}}^2} \tag{5.4}$$

where Q_b^0 and $Q_{\bar{b}}^0$ are positive.

We will challenge these assumptions later in Sections 5.3.2 and 5.6.

In high energy processes charge (C) is conserved with high accuracy. B-decay modes that violate C have small branching fractions, are charge conjugate, and therefore do not affect the momentum-weighted charge distribution. The C conservation requirement leads to:

$$\sigma_b = \sigma_{\bar{b}} \ , \quad Q_b^0 = Q_{\bar{b}}^0. \tag{5.5}$$

We do not use these equations in the present formalism, but it is interesting to see how well they hold. Figure 5.1 shows Monte Carlo distributions of Q_b and $Q_{\bar{b}}$ fit to a Gaussian hypothesis. Parameters extracted from the fit are $\langle Q_b \rangle = -0.91$ and $\langle Q_{\bar{b}} \rangle = 1.01$ with a width $\sigma_b = 2.70$ and $\sigma_{\bar{b}} = 2.69$. While the widths of the two distributions agree very well, the mean values are quite different. Nuclear interactions with detector material shift the balance by adding more positively charged tracks to

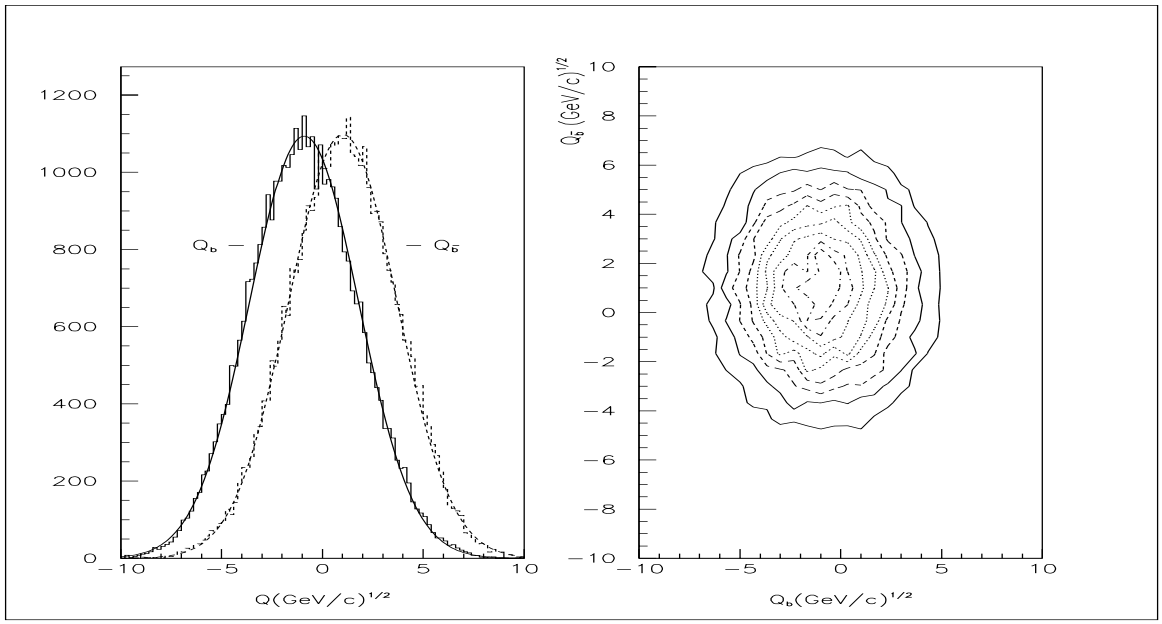

Figure 5.1: On the left plot histograms of Q_b and $Q_{\overline{b}}$ (from Monte Carlo) and Gaussian fits are shown. On the right is shown a contour plot of the Q_b, $Q_{\overline{b}}$ joint distribution.

both hemispheres. The second graph on Figure 5.1 shows the contour plot of the $Q_b(Q_{\overline{b}})$ dependence. In the absence of correlations it is a symmetric distribution. The correlation extracted from the fully simulated Monte Carlo sample of $Z^0 \to b\overline{b}$ events is $\lambda_b \approx 3\%$. That value is small and will be properly defined and corrected for in Section 5.3.2

We define the sum and the difference of charges from both hemispheres as:

$$Q_{sum} = Q_b + Q_{\overline{b}}, \tag{5.6}$$

$$Q_{dif} = Q_b - Q_{\overline{b}}. \tag{5.7}$$

Distributions for those new variables can be derived from Equations 5.3 and 5.4:

$$p(Q_{sum}) = \frac{1}{\sqrt{2\pi\sigma_0^2}} e^{-(Q_{sum}+Q_{sum}^0)^2/2\sigma_0^2}, \tag{5.8}$$

$$p(Q_{dif}) = \frac{1}{\sqrt{2\pi\sigma_0^2}} e^{-(Q_{dif}+Q_{dif}^0)^2/2\sigma_0^2}, \tag{5.9}$$

where

$$\sigma_0^2 = \sigma_b^2 + \sigma_{\overline{b}}^2, \quad Q_{sum}^0 = Q_b^0 - Q_{\overline{b}}^0, \quad Q_{dif}^0 = Q_b^0 + Q_{\overline{b}}^0 \ . \tag{5.10}$$

The parameters of the Q_{sum} distribution can be measured directly in the data because they are symmetric with respect to interchange of b and $\overline{b}$ quarks. However, this is not true for the Q_{dif} distribution. By definition Q_{dif} requires the knowledge of which hemisphere contains the b and which contains the $\overline{b}$ quark. We do not have this information in the real experiment, so the two observables that were used here are Q_{sum} and $|Q_{dif}|$.

The task now is to calculate $p^{correct}(|Q_{dif}|)$, the probability that we assign the b quark direction correctly as a function of $|Q_{dif}|$. As described in Section 2.1.3, we assign the thrust axis direction so that Q is negative (Equation 2.4), making it an estimation of the b quark direction. The first plot on Figure 5.2 shows the Monte Carlo distribution of Q_{dif}. The hatched area under the histogram corresponds to $Q_{dif} < 0$ and that is when the b quark direction assignment is correct. When the absolute value of Q_{dif} is taken, it effectively "flips" the negative part of the distribution to the right (second plot on Figure 5.2) and the $|Q_{dif}|$ distribution can be thought of as consisting

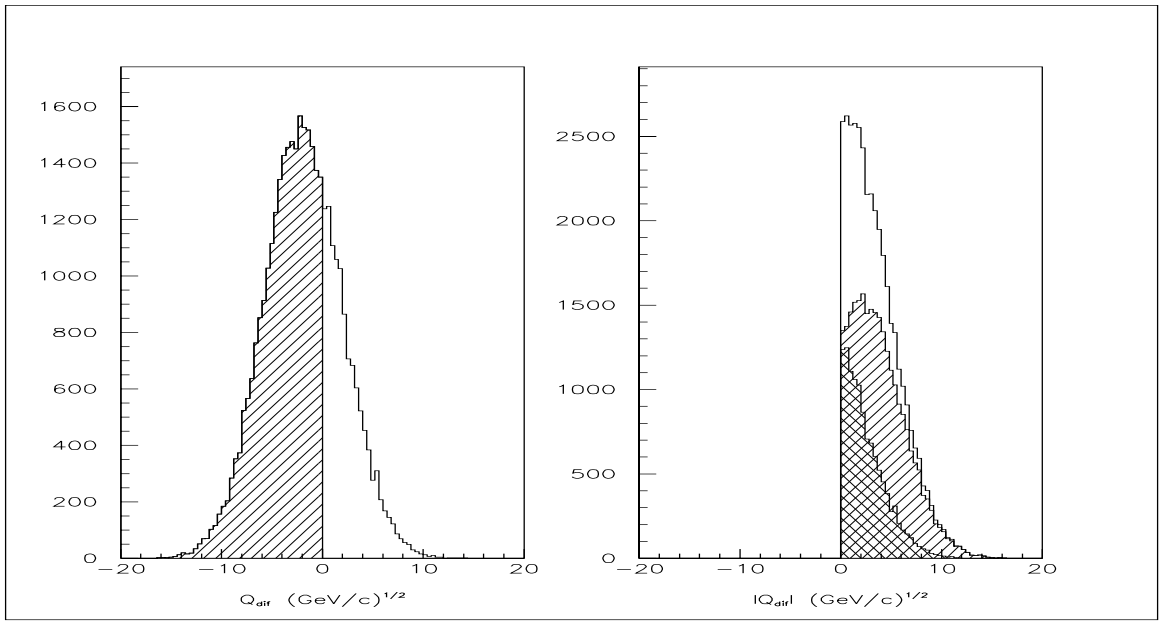

Figure 5.2: Q_{dif} and $|Q_{dif}|$ distributions (from the Monte Carlo). The hatched area on the left plot corresponds to the correct b quark direction assignment. The double-hatched area on the right plot represents the $Q_{dif} > 0$ part of the $|Q_{dif}|$ distribution.

of two parts:

$$p(|Q_{dif}|) = p(Q_{dif} > 0) + p(Q_{dif} < 0) \tag{5.11}$$

or

$$p(|Q_{dif}|) = \frac{1}{\sqrt{2\pi\sigma_0^2}} e^{-(|Q_{dif}|+Q_{dif}^0)^2/2\sigma_0^2} + \frac{1}{\sqrt{2\pi\sigma_0^2}} e^{-(|Q_{dif}|-Q_{dif}^0)^2/2\sigma_0^2}. \tag{5.12}$$

The correct-sign probability can then be expressed as:

$$p^{correct}(|Q_{dif}|) = \frac{p(Q_{dif} < 0)}{p(Q_{dif} > 0) + p(Q_{dif} < 0)} = \frac{1}{1 + e^{-\alpha|Q_{dif}|}} \ , \tag{5.13}$$

where

$$\alpha = \frac{2Q_{dif}^0}{\sigma_0^2} \ . \tag{5.14}$$

The parameter α defines the "effectiveness" of the technique used here. If $\alpha = 0$,

then $p^{correct} = 0.5$ for any $|Q_{dif}|$ which means that there is no analyzing power (the probability of correct charge assignment is 50 %).

The next question is to calculate α from the data. From Equations 5.8 – 5.10 we know that $\sigma_0 = \sigma_{dif} = \sigma_{sum}$. Since σ_{sum} can be measured directly in the experiment, the only unknown parameter in α is Q^0_{dif}. Let us have a closer look at the calculation of σ_{dif}. By the basics of statistics:

$$\sigma^2_{dif} = \langle Q^2_{dif} \rangle - \langle Q_{dif} \rangle^2 \ , \tag{5.15}$$

and given that $\sigma_{dif} = \sigma_{sum}$, $\langle Q_{dif} \rangle = Q^0_{dif}$ and $\langle Q^2_{dif} \rangle = \langle |Q_{dif}|^2 \rangle$, Equation 5.15 can be rewritten as:

$$\sigma^2_{sum} = \langle |Q_{dif}|^2 \rangle - \left(Q^0_{dif}\right)^2 \ , \tag{5.16}$$

giving

$$\alpha = \frac{2\sqrt{\langle |Q_{dif}|^2 \rangle - \sigma^2_{sum}}}{\sigma^2_{sum}} \ , \tag{5.17}$$

where everything can be calculated from the data using the two observables: Q_{sum} and $|Q_{dif}|$.

The plot of $p^{correct}(|Q_{dif}|)$ and the fit to Equation 5.13, extracted from the Monte Carlo sample of $Z^0 \to b\bar{b}$ events, are shown in Figure 5.3. The results of the fit are $\alpha_b = 0.2453 \pm 0.0013$ with $\chi^2/d.o.f. = 1.4$. The error is statistical only. Table 5.2 shows details of the α_b calculations for the current analysis.

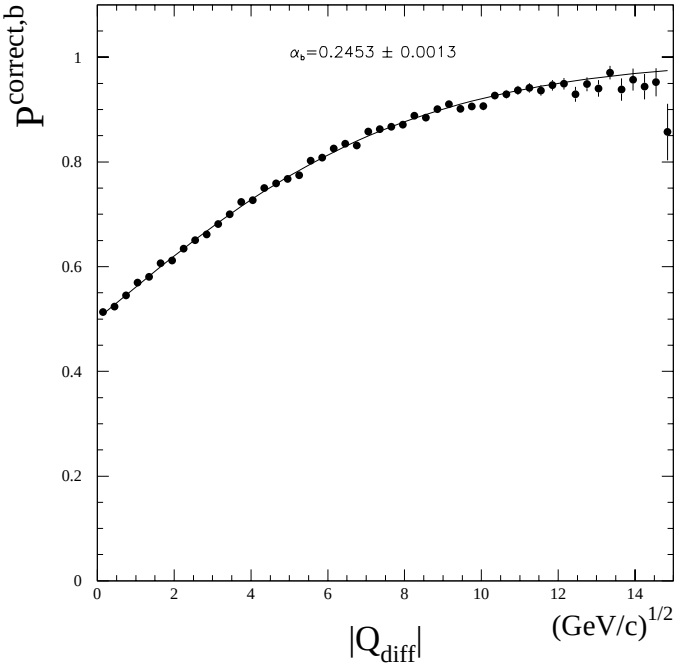

Figure 5.3: Probability of correct charge assignment.

5.3.2 Hemisphere Correlation

In the previous section we have assumed Q_b and $Q_{\overline{b}}$ to be two uncorrelated distributions. What can be expected if there is a correlation? The presence of correlation would mean that the probability to get some value of $Q_{\overline{b}}$ depends on the value of Q_b :

$$p(Q_{\overline{b}}) = f(Q_{\overline{b}}, Q_b) \tag{5.18}$$

and *vice versa*. It effectively stretches the joint probability distribution of Q_b and $Q_{\overline{b}}$ along some axis. CP conservation requires the widths of the Q_b and $Q_{\overline{b}}$ distributions to be the same (Equation 5.5). That means the only deformation possible is along the $(Q_b - Q_{\overline{b}})$ and $(Q_b + Q_{\overline{b}})$ axes. This effect is schematically shown in Figure 5.4.

The ratio of widths along the $(Q_b - Q_{\overline{b}})$ and $(Q_b + Q_{\overline{b}})$ axes would be a sensible measure of correlation. In the absence of correlation, this ratio is 1. The deviation from unity means that a correlation is present. We define the jet-charge correlation as:

$$\lambda = \frac{\sigma_{dif}}{\sigma_{sum}} - 1 \ . \tag{5.19}$$

The correlation, extracted from the fully simulated Monte Carlo sample of ≈ 400000 $Z^0 \to b\overline{b}$ events, is $\lambda_b = 2.67 \pm 0.11\%$, where the error is statistical.

The presence of correlation affects the results of the previous section in the following way: we have explicitly used $\sigma_{dif} = \sigma_{sum}$ in the derivation of α (Equations 5.15 – 5.17). When the effects of the correlation are taken into account, the corrected

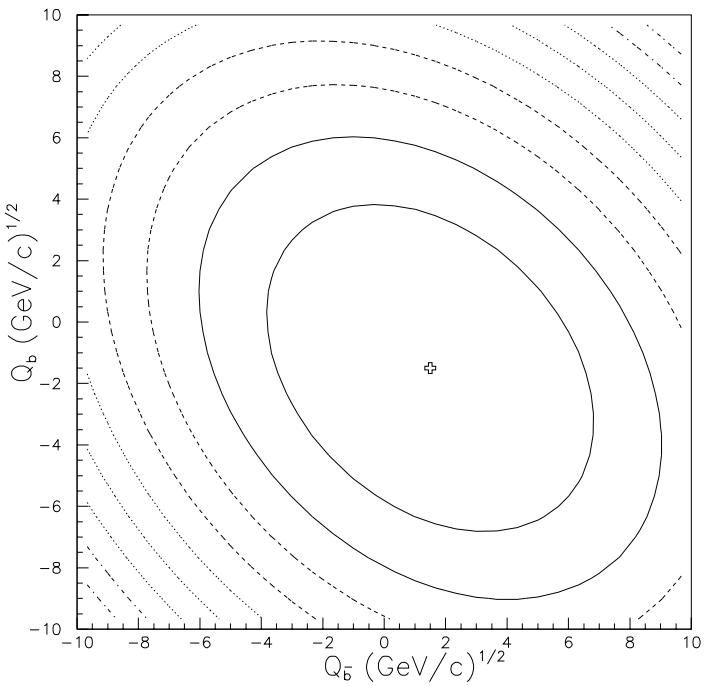

Figure 5.4: Possible effect of the hemisphere correlation

expression for σ_{dif} should be used:

$$\sigma_{dif} = (1+\lambda)\sigma_{sum} \ , \tag{5.20}$$

modifying Equation 5.17 as follows:

$$\alpha = \frac{2\sqrt{\langle |Q_{dif}|^2 \rangle - (1+\lambda_b)^2 \sigma_{sum}^2}}{(1+\lambda_b)^2 \sigma_{sum}^2} \ . \tag{5.21}$$

For this analysis, the correlation was estimated from the Monte Carlo, and both statistical and systematic errors on λ_b were propagated and included in the systematic uncertainties on A_b.

5.3.3 Light Flavor Subtraction

If the purity of the tagged sample were $\Pi_b = 100\%$, then the hemisphere correlation would be the only correction to be applied in the α_b calculation. In reality only about 90% of the events in the tagged sample are $Z^0 \to b\overline{b}$ events and thus the effects of light flavor contamination have to be taken into account. The way it is done in the present analysis is to correct the widths of the relevant distributions. In the data we measure the mixture of all flavors:

$$\langle |Q_{dif}|^2 \rangle_{measured} = \sum_{flavours} \Pi_f \langle \left| Q_{dif}^f \right|^2 \rangle \ , \tag{5.22}$$

where the purity of flavor f is $\Pi_f = \frac{N_{tagged}^f}{N_{tagged}^{all}}$ $(f = u, d, s, c, b)$ in the tagged sample. Also

$$(\sigma_{sum}^2)_{measured} = \sum_{flavours} \Pi_f \langle (Q_{sum}^f)^2 \rangle - (\sum_{flavours} \Pi_f \langle Q_{sum}^f \rangle)^2 = \sum_{flavours} \Pi_f (\sigma_{sum}^f)^2 + \Delta \ , \tag{5.23}$$

Table 5.1: Details of Light Flavor Subtraction.

Flavor (f)	$\sqrt{\langle \left\lvert Q^f_{dif} \right\rvert^2 \rangle}$	σ^f_{sum}
MonteCarlo		
All Tagged Events	4.383 ± 0.011	3.857 ± 0.010
b	4.431 ± 0.012	3.876 ± 0.011
c	4.033 ± 0.037	3.739 ± 0.035
uds	4.45 ± 0.12	3.95 ± 0.10
Data		
All Tagged Events	4.259 ± 0.028	3.755 ± 0.025

where

$$\Delta = \sum_{flavours} \Pi_f \langle Q^f_{sum} \rangle^2 - \langle Q_{sum} \rangle^2 \ . \tag{5.24}$$

The conservation of charge requires $\Delta = 0$, as $\langle Q_{sum} \rangle = \langle Q^f_{sum} \rangle = 0$ for all flavors. Interactions with detector material add extra positive charge to both hemispheres (Section 5.3.1) and give $\langle Q^f_{sum} \rangle$ some positive value. This way Δ does not have to be zero, but can be very small if $\langle Q^b_{sum} \rangle \approx \langle Q^c_{sum} \rangle \approx \langle Q^{uds}_{sum} \rangle$.

The value of Δ extracted from the Monte Carlo is $\Delta = -0.00006$. This value is very small and was neglected in the current analysis. The final formulas for $\langle \left\lvert Q^b_{dif} \right\rvert^2 \rangle$ and σ^b_{sum} are:

$$\langle \left\lvert Q^b_{dif} \right\rvert^2 \rangle = \frac{\langle \left\lvert Q^b_{dif} \right\rvert^2 \rangle_{measured} - \Pi_c \langle \left\lvert Q^c_{dif} \right\rvert^2 \rangle - \Pi_{uds} \langle \left\lvert Q^{uds}_{dif} \right\rvert^2 \rangle}{\Pi_b} \tag{5.25}$$

and

$$(\sigma^b_{sum})^2 = \frac{(\sigma^2_{sum})_{measured} - \Pi_c (\sigma^c_{sum})^2 - \Pi_{uds} (\sigma^{uds}_{sum})^2}{\Pi_b} \ . \tag{5.26}$$

Table 5.1 shows the values of $\sqrt{\langle \left\lvert Q^f_{dif} \right\rvert^2 \rangle}$ and σ^f_{sum} measured in the data and

Table 5.2: Details of Self-Calibration.

Comments	α_b
MonteCarlo	
Direct fit to Monte Carlo truth	0.2453 ± 0.0013
Self-Calibration, No Correlation, No Light Flavor Subtraction	0.2802 ± 0.0051
Self-Calibration, Correlation $\lambda_b = 2.67\%$, No Light Flavor Subtraction	0.2399 ± 0.0052
Self-Calibration, Correlation $\lambda_b = 2.67\%$, Light Flavor Subtraction Applied	0.2447 ± 0.0052
Data	
Self-Calibration, Correlation $\lambda_b = 2.67\%$, Light Flavor Subtraction Applied	0.249 ± 0.013

Monte Carlo.

In the current analysis, the light flavor subtraction correction is small due to the high purity of the tag and the fact that the widths of the distributions do not vary significantly from one flavor to another. The change in A_b, after the light flavor subtraction was applied, was $\frac{\delta A_b}{A_b} = 0.8\%$. The systematic error in this correction was taken to be 50 % of this value.

5.3.4 Self-Calibration Results

Results of the self-calibration, applied to the Monte Carlo and the data, are shown in Table 5.2. When effects of the hemisphere correlation are taken into account and the light flavor subtraction is applied, the self-calibrated technique shows no bias. There is also a good agreement between the values of α_b extracted from the data and from the Monte Carlo.

5.4 QCD Corrections

Effects of the b-quark axis smearing due to the final state QCD radiation (Section 1.2.3) are incorporated in the analysis by applying a correction Δ_{QCD} to the maximum likelihood function (Equation 5.1). Theoretical calculations of the QCD corrections to the asymmetry may be found in the literature [53] [54]. However there is a problem in using these corrections. Most theoretical calculations use the b-quark direction to define the asymmetry. In the current measurement, the thrust axis of the event is used as an estimation of the initial quark direction. The thrust axis, taking into account the momentum flow of the whole event, is less sensitive to the QCD radiation. Theoretical estimations [55] [56] show that $\Delta_{QCD}^{Thrust} = (0.9 - 0.95)\Delta_{QCD}^{Quark}$ at the parton level. One has to note, however, that in the case of a three-particle final state ($q\bar{q}g$) the thrust axis is always parallel to the direction of flight of the particle with the highest momentum. Also the B-tagging procedure and momentum-weighted track-charge technique, used in the current experiment, suppress events with hard gluon radiation.

Consequently, we have taken a different approach. The first-order theoretical calculations by J.B.Stav and H.A.Olsen [54] for massive quarks were used as a basis:

$$\Delta_{SO}(|\cos\theta|) = 1 - \frac{A_q(|\cos\theta|)}{A_0} \ , \tag{5.27}$$

where A_0 is the Born-level asymmetry (Equation 1.20) and A_q is the asymmetry based on the b-quark direction after all perturbutive radiation. Then Δ_{SO} was corrected for

analysis bias (thrust axis, B-tag and Jet Charge). The total correction is then:

$$\Delta_{QCD} = 1 - \frac{A_{exp}}{A_0} = x\Delta_{SO} \ , \tag{5.28}$$

with x estimated from the Monte Carlo and defined as:

$$x = \left(1 - \frac{\frac{A_{exp}}{A_0} - 1}{\frac{A_0}{A_q} - 1}\right) \ . \tag{5.29}$$

A_{exp} is the asymmetry measured in the experiment. The value $x = 0$ would mean that the measured A_b is not sensitive to gluon radiation and no QCD corrections need be applied, while $x = 1$ would mean that there is no analysis bias so that the theoretical correction Δ_{SO} must be applied in full.

A generator-level Monte Carlo was used to estimate x. JETSET7.4 with the first order matrix element (parameter MSTJ(101)=1) was used to generate events. Then a simple model of detector acceptance, analysis and tag cuts was applied. After that, the self-calibrating maximum likelihood method was used to extract A_{exp} in each bin of $|\cos\theta|$. Figure 5.5 shows $\mathbf{x}$ as a function of $|\cos\theta|$. The horizontal line fit was used in the $|\cos\theta|$ range of $0 - 0.7$ to extract the average correction: $x = 0.25 \pm 0.08$ with $\chi^2 = 1.4/dof$.

So the total applied QCD correction was:

$$\Delta_{QCD}(|\cos\theta|) = 0.25\Delta_{SO}(|\cos\theta|) \ . \tag{5.30}$$

The total QCD corrections used in the analysis, Δ_{QCD}, as well as the theoretical calculations, Δ_{SO}, are shown in Figure 5.6.

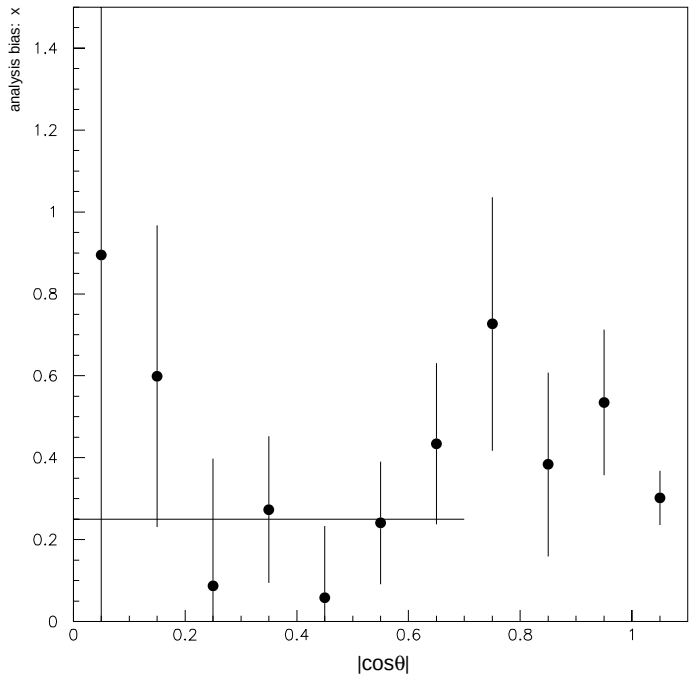

Figure 5.5: Analysis-related bias in the QCD correction for $b\bar{b}$ events, x, estimated from the generator level JETSET7.4. Only the first 7 bins are used in the analysis. The 11th bin represents x averaged over all $|\cos\theta|$.

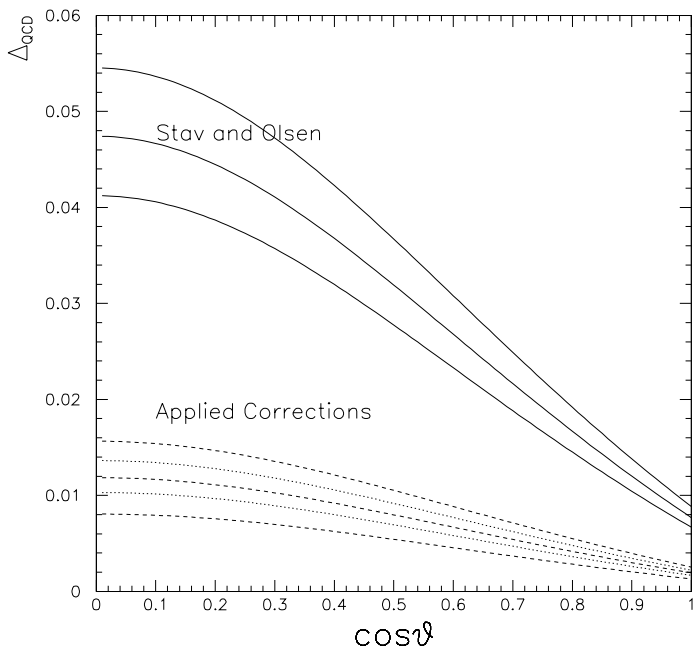

Figure 5.6: Theoretical calculations by Stav and Olsen, Δ_{SO} (solid line), and total QCD correction applied in the analysis, Δ_{QCD} (dashed line). The solid line band represents the uncertainty of the theoretical calculations, mainly due to the error in α_s. The dashed line band corresponds to statistical errors in $\mathbf{x}$, and the dotted line band covers theoretical uncertainty in Δ_{QCD}.

5.5 Asymmetry Measurement

5.5.1 Event and Track Selection

For the purpose of calculating the momentum-weighted jet charge, a loose set of cuts was applied to reconstructed tracks, while stricter requirements were placed on tracks used for selecting hadronic events and for the tag. "Jet-charge quality" tracks were required to have $p_\perp > 0.15$ GeV/c, $p_{tot} < 50$ GeV/c, $|\cos\theta| < 0.8$, number of CDC hits $N_{hits} > 39$, radius of the first CDC hit $R < 45$ cm, track fit $\chi^2/dof < 5$ and point of closest approach to the beam line (POCA) within a cylinder of radius $r_0 = 2$ cm and half-length $l_0 = 10$ cm about the IP.

"Tag quality" tracks were, in addition, required: to have the point of closest approach within $(r_0, l_0) = (0.3, 1.5)$ cm, at least one VXD hit, and impact parameter error $\sigma_d < 250$ μm; and not to be identified as a γ conversion or a product of Λ or K^0_S decay.

Events were classified as hadronic decays of Z^0 if they contained at least 7 tag quality tracks out of which at least 3 tracks had to be linked with 2 or more vertex detector hits, a visible energy of at least 20 GeV, and a thrust axis satisfying $|cos\theta_{thrust}| < 0.7$. The thrust axis was determined using energy deposition in the LAC. Figure 5.7 shows track multiplicity, visible energy and $\cos\theta_{thrust}$ distributions for the data and Monte Carlo. Hadronic event selection cuts are shown with vertical lines.

The main background comes from $Z^o \to \tau\bar{\tau}$ events and is estimated to be less then

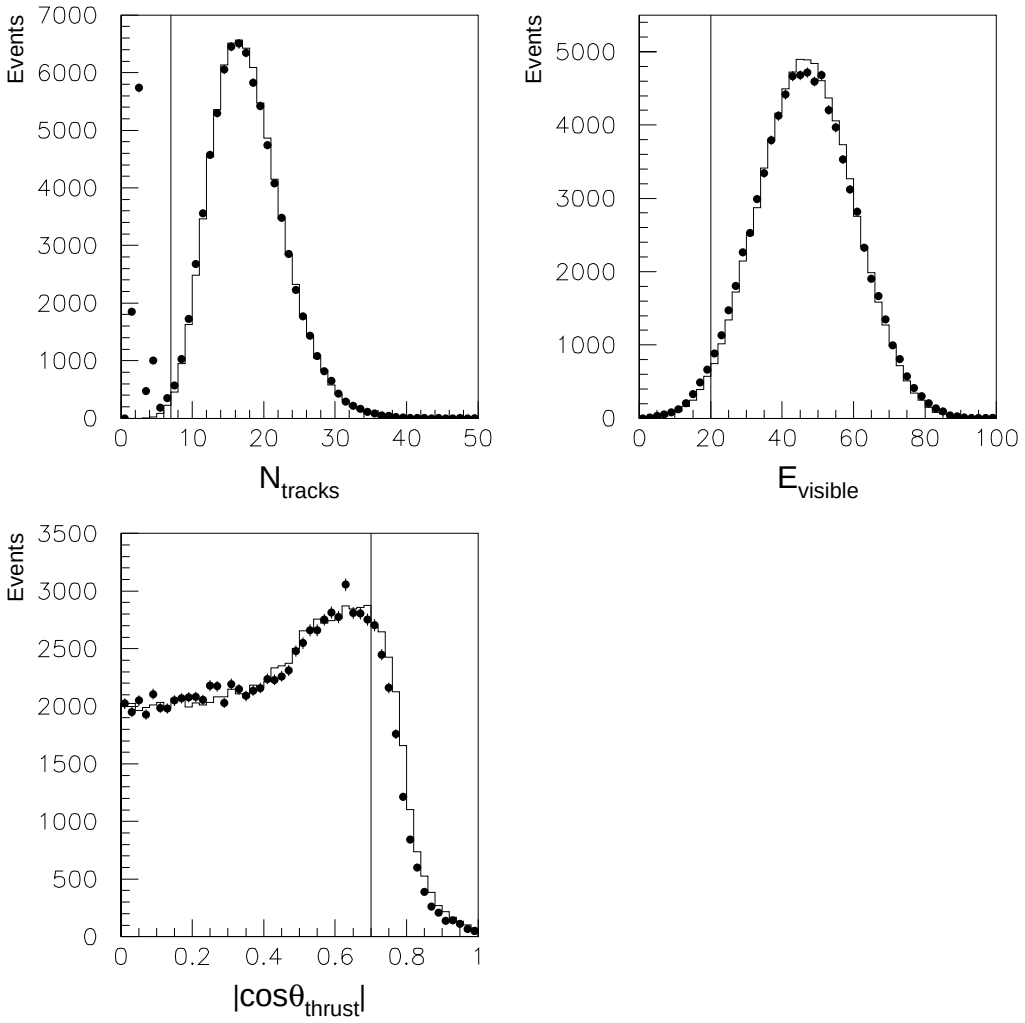

Figure 5.7: Hadronic event selection variables for data (dots) and Monte Carlo (histogram). For each cut shown, the rest of the cuts were applied.

0.1% of the sample. A total of 76554 events from the 1993-1995 data sample satisfy these requirements.

From this hadronic sample, two and three jet events were selected using the YCLUS jet-finding algorithm [60] with the parameter $Y_{cut} = 0.02$, leaving 71951 events in the sample.

5.5.2 B Tag

To enrich the sample with $Z^0 \to b\bar{b}$ events, a B tag based on topological reconstruction of B-decay vertexes was applied. The ZVTOP program [58] was used for secondary vertex finding. The idea is to look at tracks as Gaussian probability tubes in 3-D co-ordinate space, $f(\boldsymbol{r})$, near the point of the track's closest approach to the IP, $\boldsymbol{r_0}$:

$$f(\boldsymbol{r}) = exp\left\{-\frac{1}{2}\left[\left(\frac{x-(x_0+y^2\kappa)}{\sigma_1}\right)^2 + \left(\frac{z-(z_0+\tan(\lambda)y)}{\sigma_2}\right)^2\right]\right\} . \tag{5.31}$$

The first term inside the exponential includes a parabolic approximation to the circular track trajectory in the x, y plane. The parameter κ is determined from the particle charge and momentum, and the SLD magnetic field. The second term describes the propagation of the trajectory in the z direction, and λ is the helix parameter of the track. Parameters σ_1 and σ_2 are the measurement errors for the track at point $\boldsymbol{r_0}$ in the x, y and z directions respectively. The search was then done for the maximum of the vertex probability function for each hemisphere separately:

$$V(\boldsymbol{r}) = \sum_i f_i(\boldsymbol{r}) - \frac{\sum_i f_i^2(\boldsymbol{r})}{\sum_i f_i(\boldsymbol{r})} . \tag{5.32}$$

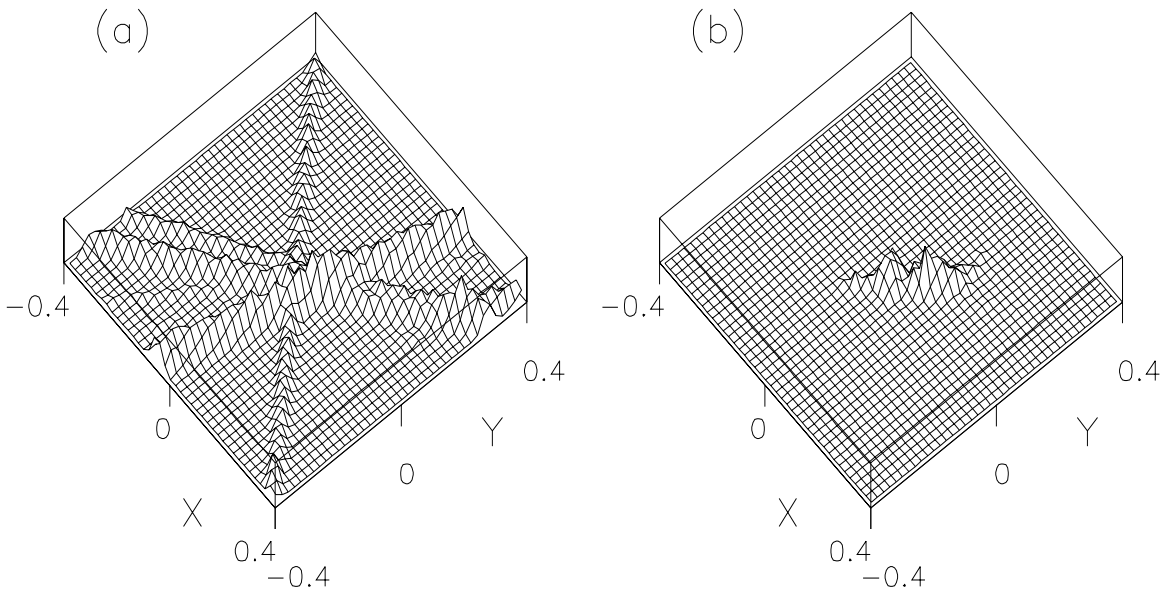

Figure 5.8: (a) Track and (b) vertex functions projected onto the x, y plane.

Figure 5.8 shows track and vertex functions projected onto the x, y plane for a Monte Carlo event. The two peaks in $V(\boldsymbol{r})$ can be seen in plot (b). The first peak at position (0,0) is due to the primary vertex (IP), while the secondary peak is displaced to the right of the IP by about 1.5 mm.

After the secondary vertex was found, more tracks were assigned on the basis of the longitudinal ($L/D > 0.25$) and transverse ($T < 1$ mm) distance from the vertex. This process is shown schematically in Figure 5.9 . Each track was assigned a pion mass and after correction for missing transverse momentum, the mass of the secondary vertex was calculated.

The vertex mass distribution calculated for the data and Monte Carlo is shown in Figure 5.10. As can be seen from this picture, the $Z^0 \to c\bar{c}$ event contribution has a

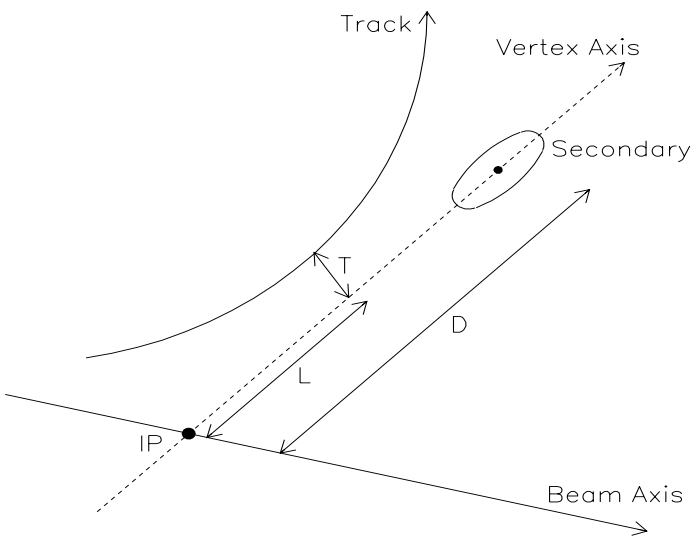

Figure 5.9: Parameters used to assign a track to the seed vertex: $T < 1$ mm, $L/D > 0.25$.

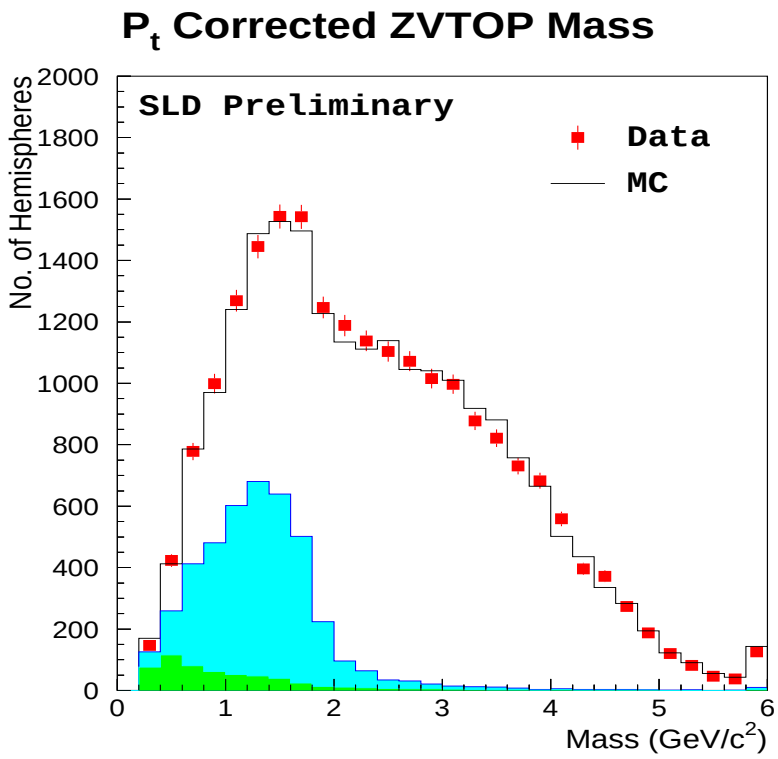

Figure 5.10: Mass distribution for data and Monte Carlo. The dark shaded area under the histogram represents the contribution from uds and the light shaded area from c quarks. The unshaded region is due to b quarks.

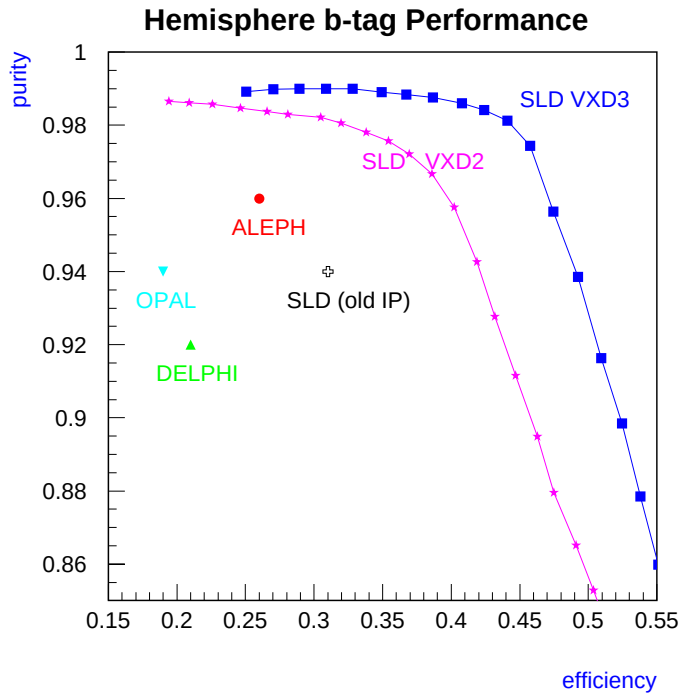

Figure 5.11: Purity (Π_b) *vs* hemisphere tagging efficiency (ϵ_b) for three LEP tags, the old SLD tag and the SLD topological tag (with VXD2). Also shown is the performance of the SLD B tag with a new vertex detector (VXD3).

clear cut-off at $1.8 - 2.0\ GeV$. This feature makes the mass tag very attractive for high-purity measurements. Figure 5.11 shows the performance of different tags.

The maximum of masses from the two hemispheres in the event was used as a tag variable in this analysis:

$$MASS = MAX(mass1, mass2)\ . \tag{5.33}$$

For the current analysis we required $MASS > 1.6\ GeV$.

Since the secondary vertex mass was calculated for each hemisphere separately, it is possible to use a double-tagging method to estimate the tagging efficiency and purity

of the tagged sample from the data. The idea of the method is that we count the number of hemispheres with mass above the cut (N_s) and the number of events where both hemispheres were tagged (N_d). In the simplified picture of only two flavors:

$$\begin{aligned} N_s &= 2\epsilon_1 N_1 + 2\epsilon_2 N_2 \ , \\ N_d &= \epsilon_1^d N_1 + \epsilon_2^d N_2 \ , \end{aligned} \tag{5.34}$$

where $\epsilon_{1(2)}$ is the efficiency to tag a hemisphere for flavor 1(2), ϵ^d is the efficiency to double-tag the event, and $N_{1(2)}$ is the total number of events of each flavor before tagging. It is more convenient to talk in terms of single and double tagging fractions $\left(F_s = \frac{N_s}{2N_{total}} \ , \ \ F_d = \frac{N_d}{N_{total}}\right)$ and production fractions for different flavors $R_{1(2)} = \frac{N_{1(2)}}{N_{total}}$. If in addition no correlation between hemispheres is assumed, then $\epsilon^d = \epsilon^2$ and from equations 5.34:

$$\begin{aligned} F_s &= \epsilon_1 R_1 + \epsilon_2 R_2 \ , \\ F_d &= \epsilon_1^2 R_1 + \epsilon_2^2 R_2 \ . \end{aligned} \tag{5.35}$$

The two equations 5.35 can be solved for any set of two parameters, usually ($\epsilon_1, \ \epsilon_2$) or ($\epsilon_1, \ R_1$), if other parameters are taken as model inputs.

In the real world the situation is more complicated since all 5 flavors are present in the tagged sample and there is a correlation between hemispheres. The tagging correlation for flavor f is defined here as:

$$\xi_f = \frac{\epsilon_f^d - \epsilon_f^2}{\epsilon_f - \epsilon_f^2} \ . \tag{5.36}$$

In terms of $R_f, \ \epsilon_f$ and ξ_f, the double-tagging equations can be written as:

$$F_s = \epsilon_b R_b + \epsilon_c R_c + \epsilon_{uds} \left(1 - R_b - R_c\right) \ ,$$

$$F_d = \left(\epsilon_b^2\left(1-\xi_b\right)+\xi_b\epsilon_b\right)R_b + \left(\epsilon_c^2\left(1-\xi_c\right)+\xi_c\epsilon_c\right)R_c \ . \tag{5.37}$$

Here we have neglected ϵ^d_{uds}, estimated to be less than $4 \cdot 10^{-6}$.

At this step, different strategies can be used. The two equations 5.37 can be solved simultaneously for ϵ_b and ϵ_c with ϵ_{uds}, ξ_b and ξ_c taken as Monte Carlo inputs (Method I). Another way would be to take ϵ_c from the Monte Carlo and use only the first Equation of 5.37 to find ϵ_b (Method II). Table 5.3 shows the details of the tag error analysis for two methods. In the first case the total error is dominated by statistics and this will be the way to calculate efficiency when there is more SLD data. However for this analysis the second method was selected. This method is limited by ϵ_c systematics, but gives a smaller total Π_b uncertainty.

So we measure F_s and F_d in the data, calculate ϵ_c , ϵ_{uds} , ξ_b , ξ_c from the Monte Carlo, use R_b and R_c as model inputs, and solve the first Equation 5.37 for ϵ_b. The goal is to calculate the purity of $Z^0 \to b\bar{b}$ events in the tagged sample, Π_b , in the maximum-likelihood function (Equation 5.1). The first step is to go from hemisphere tagging efficiencies ϵ to the event tag, ϵ^{ev} :

$$\epsilon^{ev} = \frac{N^{hem}_{tag} - N^{events}_{double\ tag}}{N_{total}} = 2\epsilon - \epsilon^d = \epsilon + (1-\xi)(1-\epsilon)\epsilon \ . \tag{5.38}$$

Then the purity of the sample can be expressed in terms of ϵ^{ev} :

$$\Pi_b = \frac{\epsilon^{ev}_b R_b}{\epsilon^{ev}_b R_b + \epsilon^{ev}_c R_c + \epsilon^{ev}_{uds}(1-R_b-R_c)} \ . \tag{5.39}$$

Values of ϵ_{uds} ,ϵ_c , ξ_b , ξ_c were extracted from the Monte Carlo, and the statistical and systematic errors were propagated and included as a systematic uncertainty in

Table 5.3: Details of Π_b Error Analysis.

Error Source	Variation	Method I σ_{Π_b}/Π_b (%)	Method II σ_{Π_b}/Π_b (%)
Statistics			
$F_s = 0.1019$	± 0.0008	1.06	0.05
$F_d = 0.0412$	± 0.0007	1.18	n/a
Systematics			
$\epsilon_c = 0.0382$	± 0.0044	n/a	0.94
$\epsilon_{uds} = 0.00103$	$\pm 20\%$	0.02	0.21
$R_c = 0.1715$	± 0.0056	0.01	0.26
$R_b = 0.2158$	± 0.0020	0.63	0.03
$\xi_c = 0.00938$	$\pm 100\%$	0.05	0.03
$\xi_b = 0.00379$	$\pm 100\%$	0.03	0.001
Total		1.7	1.0

Π_b. The error on R_b was taken as the total difference between the world average measurement $R_b^{meas} = 0.2178 \pm 0.0011$ and the Standard Model prediction $R_b^{SM} = 0.2158 \pm 0.0003$. The precision of the world average measurement $R_c^{meas} = 0.1715 \pm 0.0056$ was taken as the error on R_c. The systematic error due to detector modeling is not included here and will be treated separately in Section 5.6.

The resulting purity of the tagged data sample with the selected mass cut of 1.6 GeV/c^2 is $\Pi_b = 91.11 \pm 0.91\%$ where the ϵ_c systematic uncertainty is the main contribution to the error. A total of 11092 events from the SLD 1993-95 data sample were selected. More details on the SLD mass tag performance can be found in [59].

5.5.3 Measurement of A_b

The actual measurement of A_b is presented in this section. As a first step of the analysis, the purity of the tagged sample, Π_b was calculated from the data (Section 5.5.2) and Monte Carlo. The purity $\Pi_b(MASS)$, binned in the reconstructed vertex mass, was used in the maximum likelihood function (Equation 5.1). The statistics of the tagged data sample are not high enough to calculate $\Pi_b(MASS)$ from the data, so a scaled Monte Carlo purity was used instead:

$$\Pi_b(MASS) = \frac{\Pi_b^{dat}}{\Pi_b^{mc}} \Pi_b^{mc}(MASS) \ . \tag{5.40}$$

The Monte Carlo was then used to estimate the light-flavor composition ($\Pi_c(MASS)$, $\Pi_{uds}(MASS)$) of the tagged sample and the inter–hemisphere correlation λ_b. The measurement of the parameter α_b was then performed using σ^2_{sum} and $\langle |Q_{dif}|^2 \rangle$ from the tagged data sample. To incorporate the $\cos(\theta)$ dependence of α_b in the analysis, a scaled MC value was used, in the same manner as in Equation 5.40 :

$$\alpha_b(|\cos(\theta_{thrust})|) = \frac{\alpha_b^{dat}}{\alpha_b^{mc}} \alpha_b^{mc}(|\cos(\theta_{thrust})|) \ . \tag{5.41}$$

Other terms in the maximum likelihood function, such as α_c, α_{uds} were estimated from the Monte Carlo. The Standard Model value of $A_c = 0.67$, together with the light quark asymmetry $A_{uds} = 0$, was used in the analysis. To correct for the final state gluon radiation, $\cos(\theta)$–dependent QCD corrections, described in Section 5.4, were used:

$$\Delta_{QCD,b}(|\cos(\theta)|) = 0.25 \Delta_{SO,b}(|\cos(\theta)|), \tag{5.42}$$

$$\Delta_{QCD,c}(|\cos(\theta)|) = 0.9\Delta_{SO,c}(|\cos(\theta)|). \tag{5.43}$$

Tracking efficiency corrections (Section 4.3) were applied in the Monte Carlo to the Jet Charge calculations but not to the tag. Also z position smearing of the POCA was applied to all tracks that were linked to the vertex detector. Figure 5.12 shows the likelihood sum $-ln(L)$ over all tagged events as a function of A_b. A second order polynomial fit to the data was used to determine the position of the minimum as well as the error range. The value extracted from the fit is $A_b = 0.912 \pm 0.045(stat)$. This value should be corrected for the initial state radiation effects, discussed in Section 1.2.3, resulting in a relative bias of 0.17%.

The final value of the bottom quark asymmetry is:

$$A_b = 0.911 \pm 0.045(stat)\ . \tag{5.44}$$

5.6 Systematic Error Analysis

Table 5.4 gives a summary of systematic errors for the A_b measurement at $MASS = 1.6\ GeV$. Each individual error is discussed in detail in the following sections. The important point to note is that the biggest single contribution to the A_b systematic error, the statistics on α_b, is statistical by nature and will improve as $\sim \frac{1}{\sqrt{N}}$ with more data. We treat this statistical uncertainty as systematic since it is method-dependent.

Table 5.4: Summary of systematic errors for A_b measurement.

Error Source	Variation	$\delta A_b/A_b$
Self-Calibration		
α_b Statistics	1σ	3.7%
Hemisphere Correlation	JETSET,HERWIG,	1.7%
$p(Q_b)$ Shape	Triangular, other shapes	0.8%
$\cos\theta$ shape of α_b	MC Shape *vs* Flat	0.4%
Light Flavor Subtraction	50%	0.4%
Analysis		
Tag Composition	Mostly ϵ_c	1.5%
Detector Modeling	Efficiency Corrections, Smearing	1.5%
QCD	$x,\ \alpha_s \pm 0.02$, 2nd order terms	0.9%
P_e	0.8%	0.8%
A_c	0.67 ± 0.08	0.8%
A_{uds}	0.0 ± 0.50	0.1%
A_e	0.1506 ± 0.0028	$\ll 0.1\%$
Gluon Splitting	100%	0.2%
Total		4.9%

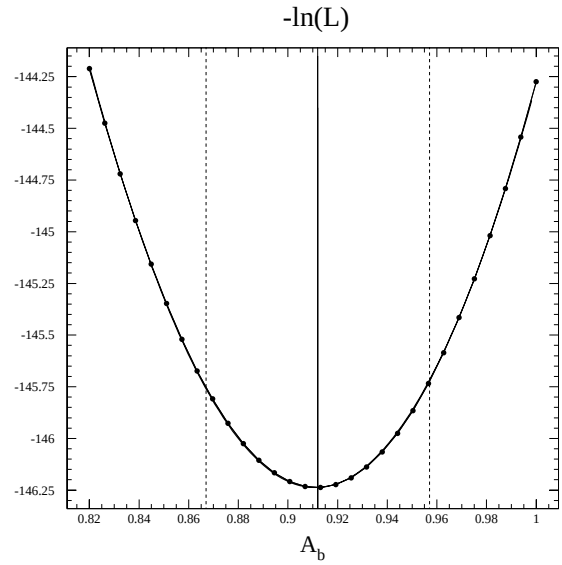

Figure 5.12: The likelihood function, $-ln(L)$, where the data points are fit with a parabola. The solid vertical line gives the central value $A_b = 0.912$, and the dashed lines represent statistical errors in A_b of ± 0.045

5.6.1 α_b Statistics

The measurement of α_b carries statistical uncertainty, propagated from statistical errors on σ_{sum} and $\langle |Q_{dif}|^2 \rangle$ measurements: $\alpha_b = 0.249 \pm 0.013$. The corresponding error on A_b was calculated by re-analyzing data with values of α_b^{dat} varied by 1 σ:

$$\frac{\delta A_b}{A_b} = \frac{A_b(\alpha_b^{dat} - \sigma_{\alpha_b^{dat}}) - A_b(\alpha_b^{dat} + \sigma_{\alpha_b^{dat}})}{2A_b(\alpha_b^{dat})}. \tag{5.45}$$

This error is expected to decrease $\sim \frac{1}{\sqrt{N}}$ with more data.

5.6.2 $p(Q_b)$ Shape

The self-calibrating technique is based on the assumption that the hemisphere momentum-weighted charge has a Gaussian distribution. A special study was done to check the

sensitivity of the measured A_b on the Q_b distribution shape.

A large amount of the Monte Carlo data was generated with the angular distribution:

$$\frac{d\sigma}{d\Omega} \propto (1 - A_e P_e)(1 + \cos^2\theta) + 2(A_e - P_e)A_f \cos\theta \ , \tag{5.46}$$

and two uncorrelated hemisphere charges, Q_b and $Q_{\bar{b}}$ with the constraint:

$$p(Q_{\bar{b}}) = p(-Q_b) \ , \tag{5.47}$$

The parameters of the trial Q_b distribution were selected from the condition that the generated σ_{sum} and $\left\langle \left| Q^2_{dif} \right| \right\rangle$ match the data. Then the self-calibrated maximum likelihood method, identical to the one used in the real analysis, was applied to extract the value of A_b. The difference between the input and extracted A_b was studied for different shapes of the Q_b distribution.

The distribution of the absolute value of the hemisphere charge from the data, $|Q_{hem}|$, was used to constrain possible Q_b distributions.

For each trial distribution, Table 5.5 shows the relative shift in measured asymmetry and the χ^2 of a fit to the data $|Q_{hem}|$ histogram using the functional form of the trial distribution. A pure Gaussian distribution shows no bias in the extracted A_b and a good χ^2. Triangular and rectangular distributions do not match the data at all. In the case of more realistic mixed distributions, the constraint was $\chi^2_{mixed} \approx 2\chi^2_{Gaussian}$. Two mixed distributions, shown in Table 5.5, are Gaussians with 2% of the event charges distributed with twice the width of the initial distribution and centered at Q_0

Table 5.5: Bias in measured A_b for different Q_b distributions.

Distribution	$\frac{\delta A_b}{A_b}$ (%)	χ^2 (d.o.f.=17)
Gaussian	-0.11 ± 0.13	20.
Triangle	-0.78 ± 0.34	9941.
Rectangle	-2.91 ± 0.32	18684.
98% Gauss + 2% at $(2\sigma_0,\ Q_0)$	$+0.56 \pm 0.13$	49.
98% Gauss + 2% at $(2\sigma_0,\ Q_0 = 0)$	$+0.62 \pm 0.13$	37.

in one case, and at the origin in another.

Based on these results, the systematic error due to a possible non-Gaussian shape of the Q_b distribution was taken to be:

$$\frac{\delta A_b}{A_b} = 0.8\% \ . \tag{5.48}$$

5.6.3 $\cos(\theta)$ shape of α_b

Since SLD tracking becomes less efficient at high values of $|\cos(\theta)|$, we expect the analyzing power to drop. A Monte Carlo estimation of the $\alpha_b(|\cos(\theta)|)$ dependence was used in this analysis. The total difference in the value of A_b extracted from the data with a θ–dependent α_b and a flat α_b was taken as the systematic error.

5.6.4 Hemisphere Correlation

The value of the correlation between hemispheres was obtained from the Monte Carlo: $\lambda_b = 2.67 \pm 0.11\%(stat)$. The systematic uncertainty was estimated by varying JETSET7.4 model parameters and comparing to a Monte Carlo model with a completely different fragmentation scheme – HERWIG5.7 . Since we do not have any samples

of fully reconstructed HERWIG5.7 or JETSET7.4 with altered parameters, the study was done at the generator level. The Monte Carlo was allowed to decay unstable particles, and a simple model of detector acceptance, tag and analysis cuts was applied. Then generator–level correlations were calculated. In order to obtain the value of λ_b at the reconstructed level, generator–level correlations were scaled down with a ratio of

$$\frac{\lambda_{full}^{JETSET}}{\lambda_{generator}^{JETSET}} = 0.61 \ , \tag{5.49}$$

where λ_{full}^{JETSET} is the correlation extracted from the fully reconstructed tuned JETSET7.4 Monte Carlo model, and $\lambda_{generator}^{JETSET}$ is the correlation with the generator-level tuned JETSET7.4. Table 5.6 shows the Monte Carlo model parameters that were changed, and the range of variations and resulting changes in the correlation at the generator level. The total uncertainty in the correlation was taken to be

$$\sigma_{\lambda_b} = 0.4\% \ . \tag{5.50}$$

5.6.5 Detector Systematics

The discrepancy between the data and Monte Carlo, described in Section 4.3, can affect the measured value of A_b. To calculate the final value of A_b, corrections were applied to the Monte Carlo events for tracking efficiency and smearing of the track impact parameter. The total change in measured A_b, with and without smearing, was taken as the systematic error: $\delta A_b/A_b = 0.6\%$. Also, effects of the tracking efficiency

Table 5.6: Summary of λ_b systematic error analysis.

Parameter		Nominal Value	Variation	$\delta\lambda_{b,\ gen}$ (%)
Λ_{QCD},	PARJ(81)	0.26	0.24 – 0.28	0.06 ± 0.14
Q_0,	PARJ(82)	1.0	0.7 – 1.8	0.17 ± 0.14
σ_q,	PARJ(21)	0.37	0.32 – 0.40	0.20 ± 0.14
γ_s,	PARJ(2)	0.28	0.25 – 0.32	0.19 ± 0.14
$[V/(V+S)]_{u,d}$,	PARJ(11)	0.50	0.30 – 0.75	0.27 ± 0.14
$[V/(V+S)]_s$,	PARJ(12)	0.45	0.45 – 0.60	0.11 ± 0.14
$[V/(V+S)]_{c,b}$,	PARJ(13)	0.53	0.53 – 0.63	0.05 ± 0.14
ϵ_b,	PARJ(55)	0.006	0.006 – 0.0277	0.04 ± 0.14
direct baryon rate,	PARJ(1)	0.08	0.08 – 0.12	0.20 ± 0.14
popcorn parameter,	PARJ(5)	1.	0. – 2.	0.11 ± 0.14
x_d,	PARJ(76)	0.7	0. – 0.7	0.16 ± 0.14
x_s,	PARJ(77)	10.	0. – 100.	0.18 ± 0.14
HERWIG5.7				0.29 ± 0.11
Total				0.6%

corrections on the tag and jet charge were studied separately, resulting in an additional relative 1.4% uncertainty.

5.6.6 QCD Systematics

The main components of the QCD systematic error are:

- Uncertainty of the theoretical calculations: $\frac{\delta\Delta_{SO,b}}{\Delta_{SO,b}} = 15\%$, mainly from the uncertainty in $\alpha_s = 0.118 \pm 0.020$. The corresponding change in A_b is

$$\frac{\delta A_b}{A_b} = 0.11\% \ . \tag{5.51}$$

- To check for the discrepancy between theoretical QCD calculations and the Monte

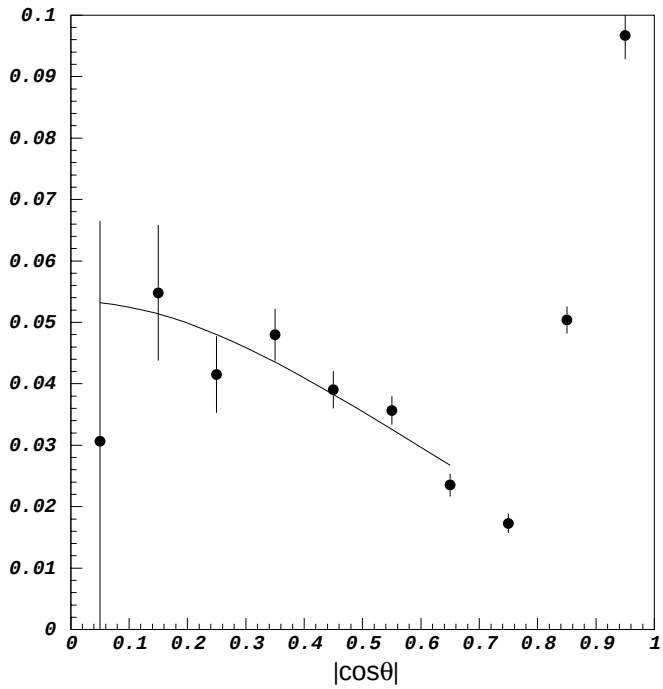

Figure 5.13: QCD corrections, $\Delta^{MC}_{SO,b}$, extracted from the Monte Carlo (points), and a theoretical fit (line) using the calculations of Stav and Olsen. Only the first 7 bins in $|\cos\theta|$ were used in the fit.

Carlo model, $\Delta_{SO,b}$ was extracted from the generated Monte Carlo sample:

$$\Delta^{MC}_{SO,b}(|\cos\theta|) = 1 - \frac{A^{MC}_q(|\cos\theta|)}{A_0} \ . \tag{5.52}$$

Then $\Delta^{MC}_{SO,b}$ was fit with the functional shape of the Stav and Olsen theoretical calculations [54]. The observed difference of $13 \pm 4\%$ was taken as an additional uncertainty on $\Delta_{SO,b}$, resulting in

$$\frac{\delta A_b}{A_b} = 0.10\% \ . \tag{5.53}$$

The value of $\Delta^{MC}_{SO,b}$ and the fitted curve are shown in Figure 5.13.

• The uncertainty in the analysis bias estimation, $x = 0.25 \pm 0.08(stat)$ (Equation 5.29). To estimate the systematic error on x, the analysis bias was recalculated with a different Monte Carlo QCD radiation mechanism (JETSET7.4 with a default parton shower model parameter MSTJ(101)=5). The result is $x = 0.16 \pm 0.09(stat)$. The difference was taken to be a systematic error. Thus the final value is $x = 0.25 \pm 0.08(stat) \pm 0.09(syst)$ and the corresponding error for A_b is

$$\frac{\delta A_b}{A_b} = 0.41\% \ . \tag{5.54}$$

• Uncertainty in QCD corrections for $c\bar{c}$ events. The full difference between the extracted A_b value with full theoretical QCD corrections, $\Delta_{SO,c}$, and with no QCD corrections for $c\bar{c}$ events was taken as the systematic error:

$$\frac{\delta A_b}{A_b} = 0.14\% \ . \tag{5.55}$$

• The uncertainty due to second order QCD effects was taken to be [53]

$$\frac{\delta A_b}{A_b} = 0.50\% \ . \tag{5.56}$$

The A_b uncertainty from the modeling of the gluon splitting was estimated separately by repeating the analysis with no Monte Carlo events containing the $g \to b\bar{b}$ process.

Combining all the pieces above, the total A_b uncertainty due to the QCD radiation was taken to be

$$\frac{\delta A_b}{A_b} = 0.9\% \ . \tag{5.57}$$

5.6.7 Background Asymmetry

To estimate the systematic error due to the unknown asymmetry of the background events, the data were reanalyzed with different values of A_c and A_{uds}. The total change in the measured value of A_b was taken as the systematic error. The precision of the combined SLD measurements of the c-quark asymmetry, $\sigma_{A_c} = \pm 0.08$, was used as the variation of A_c. The asymmetry of the light flavor components of the tagged sample, A_{uds}, was measured in the Monte Carlo and is consistent with zero. A variation of $\sigma_{A_{uds}} = \pm 0.5$ was taken for the systematic error estimation.

5.7 Extracting A_b from Monte Carlo

As an important cross-check of the method, the value of A_b was extracted from the Monte Carlo. The self-calibrating technique was used on the Monte Carlo sample exactly the same way as for the data. The Monte Carlo was generated with the value of $A_b = 0.935$ and the extracted asymmetry was: $A_b^{MC} = 0.925 \pm 0.013(stat)$, consistent with the expected value. Figure 5.14 shows A_b^{MC} as a function of the purity.

5.8 Summary

A measurement of A_b has been presented in this section. The mass of the reconstructed B decay vertex was used as a tag variable. The purity of the tagged sample was calibrated from the data using the double tagging technique. With the selected cut

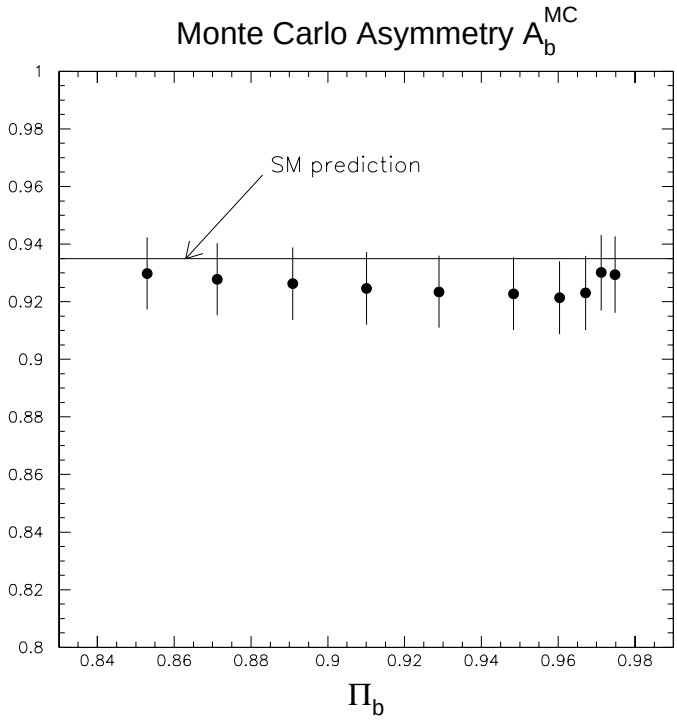

Figure 5.14: Asymmetry measured in the Monte Carlo as a function of the purity of the tagged sample.

$MASS > 1.6$ the purity was determined to be $\Pi_b = 91.11 \pm 0.91\%$. The difference between momentum-weighted charges from two hemispheres was used to provide the sign of the thrust axis. The analyzing power for this method was calculated from the data. The resultant value of A_b measured with the SLD 1993-1995 data sample is:

$$A_b = 0.911 \pm 0.045(stat) \pm 0.045(syst). \tag{5.58}$$

Chapter 6

$Z^0 \to b\overline{b}$ Vertex Parameters

A model-independent parameterization of the $Z^0 \to b\overline{b}$ vertex coupling and a fit to six observables are presented in this chapter.

A deviation from the Standard Model (SM) prediction for $R_b = \Gamma_{b\bar{b}}/\Gamma_{had}$ and A_b has been observed at LEP in recent years. These two measurements give indications of possible new physics at the $Z^0 \to b\overline{b}$ vertex. However any change in the couplings will also affect other observables, like σ^0_{had} and $R_Z = \Gamma_{had}/\Gamma_{l^+l^-}$. Takeuchi, Grant and Rosner [72] proposed a model-independent parametrization of the $Z^0 \to b\overline{b}$ vertex to constrain contributions of new physics to left- and right-handed couplings. Alternative parameterizations exist in the literature [73] [74] and can be expressed in terms of the formalism of Takeuchi, Grant, and Rosner.

6.1 Parameterization

The coupling of a fermion to the Z^0 is described by two constants: c^f_L and c^f_R. Also, in the Standard Model, couplings and observables depend on the value of $\sin^2\theta_{eff}$ [75]. Following the paper of Takeuchi, Grant, and Rosner, the selected parameterization was:

$$\sin^2\theta_{eff} \quad = \quad [\sin^2\theta_{eff}]_{SM} + \delta s^2,$$

$$
\begin{aligned}
c_L^b &= [c_L^b]_{SM} + \frac{1}{3}\delta s^2 + \delta c_L^b, \\
c_R^b &= [c_R^b]_{SM} + \frac{1}{3}\delta s^2 + \delta c_R^b \ , \qquad (6.1)
\end{aligned}
$$

where δs^2, δc_L^b, δc_R^b are contributions from new physics to $\sin^2\theta_{eff}$, c_L^b, c_R^b respectively. The Standard Model predictions are denoted as $[...]_{SM}$. For the purpose of fitting it is convenient to define the following linear combinations of δc_L^b and δc_R^b :

$$
\begin{aligned}
\xi_b &= (\cos\phi_b)\delta c_L^b - (\sin\phi_b)\delta c_R^b, \\
\zeta_b &= (\sin\phi_b)\delta c_L^b + (\cos\phi_b)\delta c_R^b \ , \qquad (6.2)
\end{aligned}
$$

where $\phi_b = \tan^{-1}\left|c_R^b/c_L^b\right| \approx 0.181$. The parameter ξ_b can be thought of as a cross section-like variable, while ζ_b is a parity violation-like variable for the new physics couplings.

The dependence of observables on δs^2, ξ_b and ζ_b can be found by expansion about the point $\delta s^2 = \xi_b = \zeta_b = 0$:

$$
\begin{aligned}
\sigma^0_{\text{had}} &= \left[\sigma^0_{\text{had}}\right]_{SM}\left(1 + 0.11\delta s^2 + 0.41\xi_b\right), \\
R_Z \equiv \, , \, {}_{\text{had}}/, \, {}_{l^+l^-} &= [R_Z]_{SM}\left(1 - 0.85\delta s^2 - 1.02\xi_b\right), \\
R_b \equiv \, , \, {}_{b\bar{b}}/, \, {}_{\text{had}} &= [R_b]_{SM}\left(1 + 0.18\delta s^2 - 3.63\xi_b\right), \\
R_c \equiv \, , \, {}_{c\bar{c}}/, \, {}_{\text{had}} &= [R_c]_{SM}\left(1 - 0.35\delta s^2 + 1.02\xi_b\right), \\
A_b &= [A_b]_{SM}\left(1 - 0.68\delta s^2 - 1.76\zeta_b\right),
\end{aligned}
$$

(6.3)

Table 6.1: Input fit parameters.

Observable	Experiment	SM prediction
$\sin^2\theta_{eff}$ (SLD)	0.23055 ± 0.00041	0.23163
$\sin^2\theta_{eff}$ (LEP)	0.23146 ± 0.00042	0.23163
A_b (SLD)	0.900 ± 0.052	0.93455
A_{FB} (LEP)	0.09852 ± 0.00223	0.10247
σ^0_{had} (LEP)	41.489 ± 0.055 nb	41.485
R_Z (LEP)	20.783 ± 0.029	20.730
R_b (LEP, SLD)	0.2177 ± 0.0011	0.21552
R_c (LEP, SLD)	0.1722 ± 0.0053	0.1723

and

$$A^b_{FB} = \frac{3}{4}A_e A_b \quad = \quad \left[A^b_{FB}\right]_{SM}\left(1 - 55.7\delta s^2 - 1.76\zeta_b\right). \tag{6.4}$$

6.2 Fit

The input parameters of the fit are summarized in Table 6.1. The experimental measurements are results presented at the 1997 Les Rencontres de Moriond [26] [27]. The LEP value of $\sin^2\theta_{eff}$ is averaged over lepton channel measurements only. The Standard Model predictions were calculated using the ZFITTER [25] program with $m_{top} = 180\ GeV/c^2$, $m_{Higgs} = 300\ GeV/c^2$, $\alpha_s = 0.117$, and $\alpha^{-1}_{EM} = 128.96$ [76]. A global 3-dimensional fit has been performed by B. Schumm [77]. The result is presented graphically in Figure 6.1 on the $\zeta_b - \delta s^2$ plane. The SLD measurement of A_b is the most direct probe of ζ_b and least sensitive to δs^2. Numerical constraints of

the non-Standard Model contributions extracted from the fit are:

$$\begin{aligned} \delta s^2 &= -0.00062 \pm 0.00053, \\ \xi_b &= -0.0025 \pm 0.0013, \end{aligned} \tag{6.5}$$

and

$$\zeta_b = 0.038 \pm 0.014 \tag{6.6}$$

In terms of δc_L^b and δc_R^b, the values in Equation 6.6 translate into:

$$\begin{aligned} \delta c_L^b &= 0.0047 \pm 0.0030, \\ \delta c_R^b &= 0.040 \pm 0.015. \end{aligned} \tag{6.7}$$

As can be seen, the right-handed coupling is more weakly constrained by present data than the left-handed coupling.

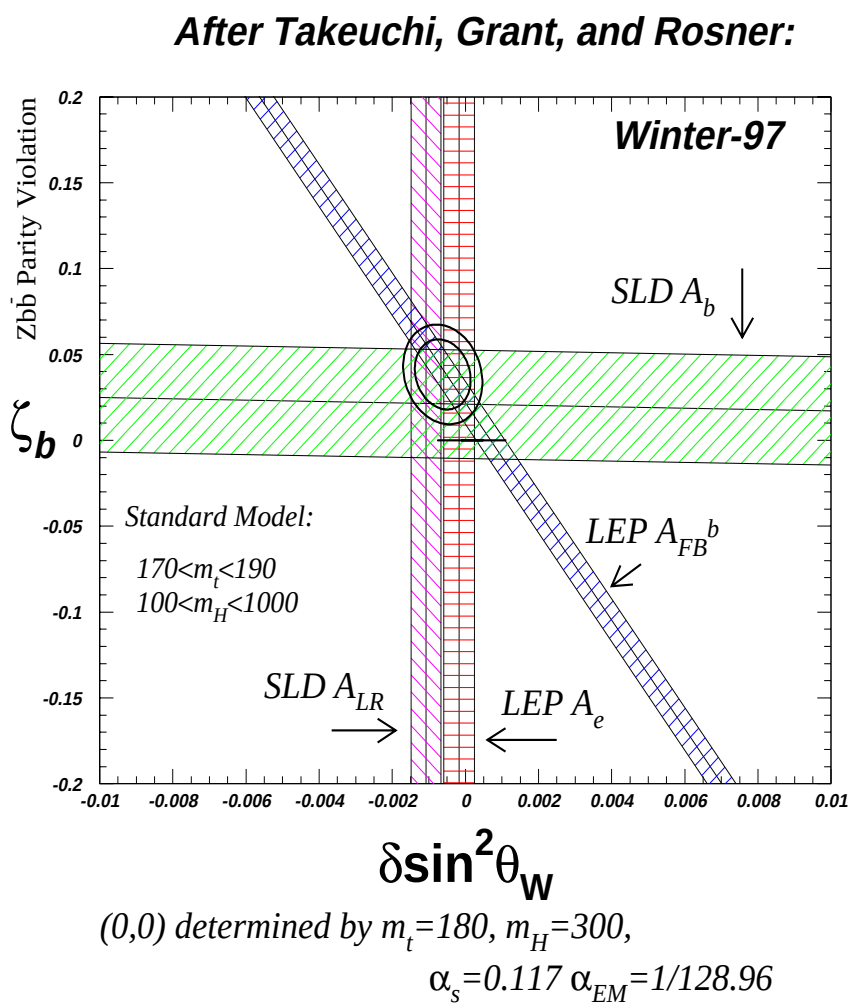

Figure 6.1: Constraints of the parity violation like parameter ζ_b, shown on the $\zeta_b - \delta s^2$ plane. The ellipses are 68% and 95% confidence-level limits. The short horizontal line near the origin is the Standard Model prediction for the range of values of m_{top} and m_{Higgs} shown on the plot. The left end of the line corresponds to the light Higgs and heavy top.

Chapter 7

Summary and Prospects

7.1 Summary

This thesis has presented a direct measurement of the parity-violating parameter A_b. A self-calibrating technique was used to calculate the probability of the correct axis signing from the data. A maximum-likelihood method, employed for the measurement, minimizes the statistical error by assigning each event a unique weight, based on the magnitude of the momentum-weighted charge. A double-tagging technique was used in the analysis to calculate the purity of the tagged sample from the data. The main model dependence of the measurement comes from the jet-charge hemisphere correlation estimation, the charm tagging efficiency estimation, the detector modeling and the modeling of the final-state QCD radiation. The resulting asymmetry, after correction for the initial-state photon radiation, is

$$A_B = 0.911 \pm 0.045(stat) \pm 0.045(syst). \tag{7.1}$$

This value is in good agreement with the Standard Model prediction of $A_b^{SM} = 0.935$ (see Section 1.2).

The status of world asymmetry measurements is summarized in Figure 7.1. The SLD average value of A_b agrees with the Standard Model prediction, while the LEP

value is 2.6 σ low. While the low value of A_b measured at LEP can be seen as a hint for a new physics at the $Z^0 \to b\bar{b}$ vertex, more precise asymmetry measurements are needed. For the moment, however, the Standard Model remains the valid theory of electroweak interactions.

7.2 Prospects

With the LEP moving to higher energies, the SLD is now the only detector in the world working in the region of the Z^0 resonance. In the beginning of 1996 a new vertex detector (VXD3) was installed in the SLD. Semiconductor technology developments in the past 5 years and accumulated experience of working with the old SLD vertex detector (VXD2) have resulted in the creation of this remarkable device. A comparison between VXD3 and VXD2 is shown in Table 7.2. The xy and rz cut views for VXD3 are shown in Figures 7.2, 7.3.

Improvements in the SLD asymmetry measurements are expected from:

- *More Statistics*.

Approximately 50,000 hadronic decays of Z^0 were recorded in the SLD 1996 run and $\sim 200,000$ more are expected during the scheduled run on 1997-1998.

- *New Vertex Detector*.

The new vertex detector provides larger angular coverage, less multiple scattering and higher efficiency. All this will result in more accurate reconstruction of the decay ver-

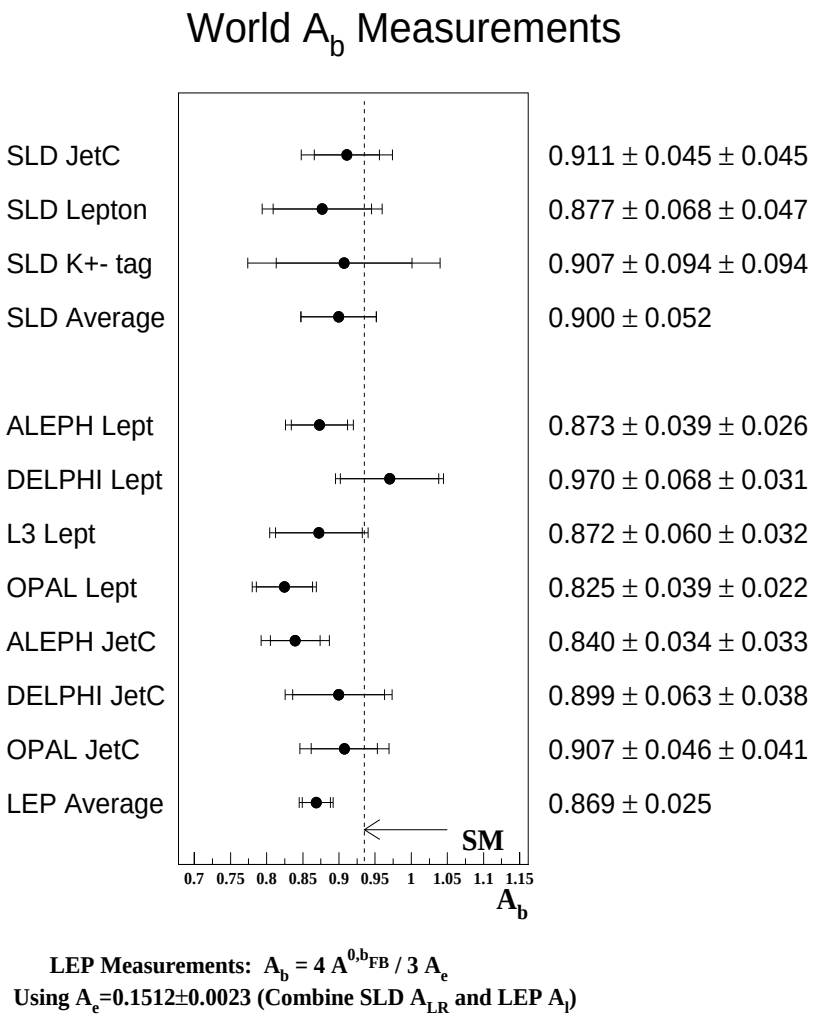

Figure 7.1: World A_b measurements (Moriond 1997).

Table 7.1: VXD3/VXD2 Comparison.

Parameter	VXD2	VXD3
Motherboard material	Alumina	Beryllium
Number of CCDs	480	96
Pixels/CCD	400×600	800×4000
Pixel size	22 μm$\times$22 μm	20 μm$\times$20 μm
Readout time	160 ms	210 ms
	(19 beam crossings)	(25 beam crossings)
Radius Layer 1	2.96 cm	2.80 cm
Radius Layer 2	3.36 cm	3.82 cm
Radius Layer 3	3.76 cm	4.83 cm
Radius Layer 4	4.16 cm	–
Radiation thickness	1.15%/layer	0.36%/layer
Average hits per track	2.3	3.0
Two-hit coverage	$\lvert\cos\theta\rvert < 0.75$	$\lvert\cos\theta\rvert < 0.90$

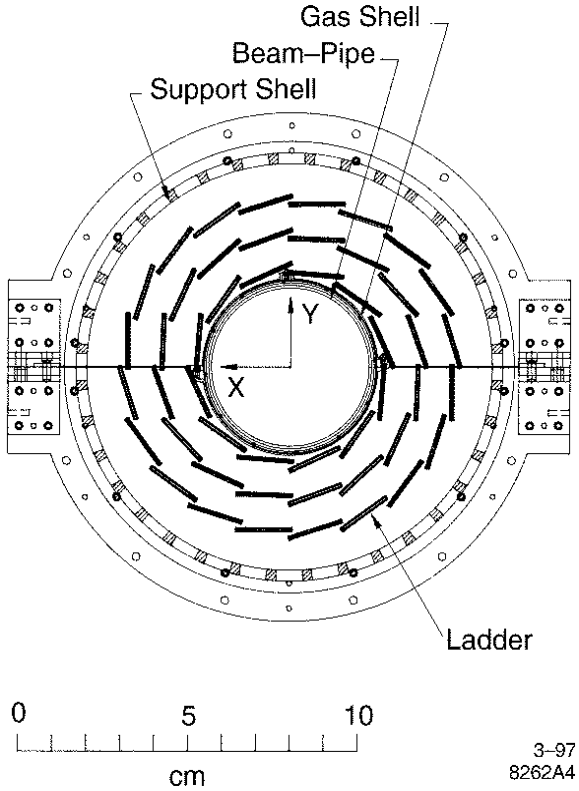

Figure 7.2: Cross-section view (xy plane) of the VXD3.

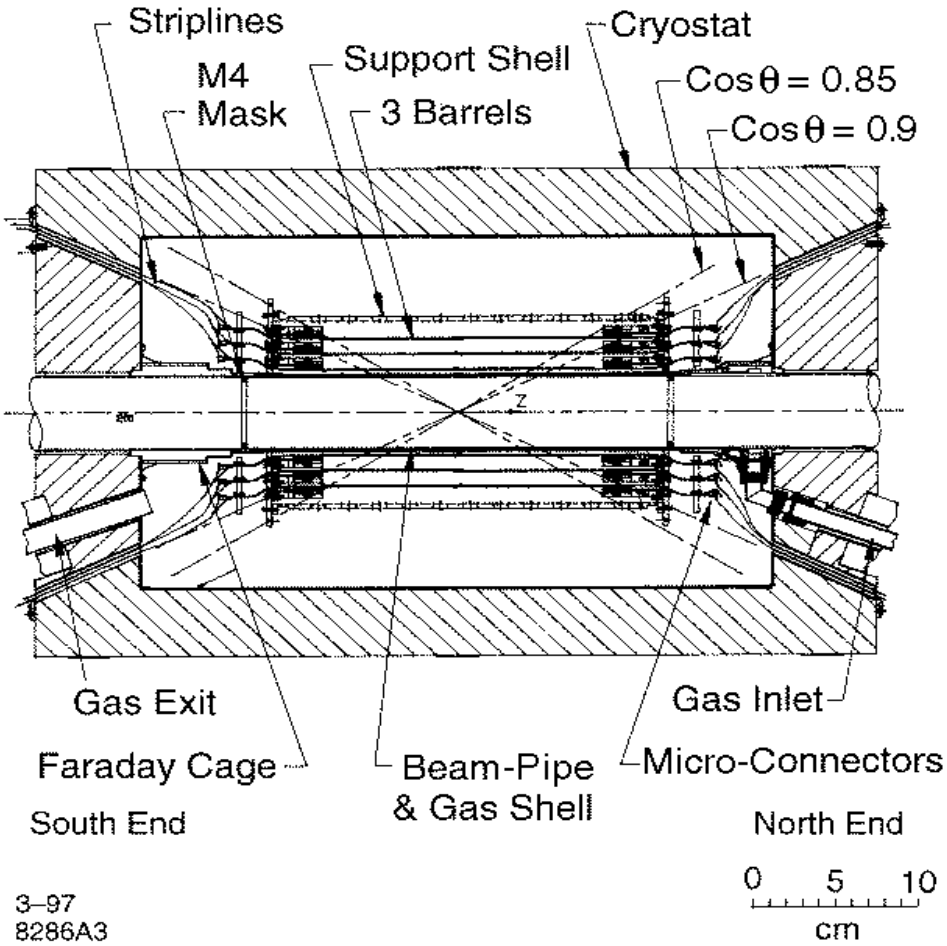

Figure 7.3: Cross-section view (rz plane) of the VXD3.

texes and better tagging. The expected B-tagging performance with the new VXD3 is shown in Figure 5.11.

- *New Analysis Techniques*.

While the jet-charge analysis will certainly benefit from the better tag, the analyzing power of the method is not expected to improve significantly. One of the alternatives would be to try to reconstruct the charge of the decayed B. A Monte Carlo study shows that in the case of charged B events this method provides very high analyzing power. Another possibility, under study now, is to combine the jet-charge, kaon and lepton analyses into a single "super tag" method.

Using these techniques, we expect that the uncertainty on A_b can be reduced to 4%.

Appendix A

The SLD Collaboration

* K. Abe,[19] K. Abe,[30] T. Akagi,[28] N.J. Allen,[4] W.W. Ash,[28]† D. Aston,[28]
K.G. Baird,[24] C. Baltay,[34] H.R. Band,[33] M.B. Barakat,[34] G. Baranko,[9]
O. Bardon,[15] T. L. Barklow,[28] G.L. Bashindzhagyan,[18] A.O. Bazarko,[10]
R. Ben-David,[34] A.C. Benvenuti,[2] G.M. Bilei,[22] D. Bisello,[21] G. Blaylock,[16]
J.R. Bogart,[28] B. Bolen,[17] T. Bolton,[10] G.R. Bower,[28] J.E. Brau,[20]
M. Breidenbach,[28] W.M. Bugg,[29] D. Burke,[28] T.H. Burnett,[32] P.N. Burrows,[15]
W. Busza,[15] A. Calcaterra,[12] D.O. Caldwell,[5] D. Calloway,[28] B. Camanzi,[11]
M. Carpinelli,[23] R. Cassell,[28] R. Castaldi,[23][a] A. Castro,[21] M. Cavalli-Sforza,[6]
A. Chou,[28] E. Church,[32] H.O. Cohn,[29] J.A. Coller,[3] V. Cook,[32] R. Cotton,[4]
R.F. Cowan,[15] D.G. Coyne,[6] G. Crawford,[28] A. D'Oliveira,[7] C.J.S. Damerell,[25]
M. Daoudi,[28] R. De Sangro,[12] R. Dell'Orso,[23] P.J. Dervan,[4] M. Dima,[8]
D.N. Dong,[15] P.Y.C. Du,[29] R. Dubois,[28] B.I. Eisenstein,[13] R. Elia,[28]
E. Etzion,[33] S. Fahey,[9] D. Falciai,[22] C. Fan,[9] J.P. Fernandez,[6] M.J. Fero,[15]
R. Frey,[20] T. Gillman,[25] G. Gladding,[13] S. Gonzalez,[15] E.L. Hart,[29]
J.L. Harton,[8] A. Hasan,[4] Y. Hasegawa,[30] K. Hasuko,[30] S. J. Hedges,[3]
S.S. Hertzbach,[16] M.D. Hildreth,[28] J. Huber,[20] M.E. Huffer,[28] E.W. Hughes,[28]

H. Hwang,[20] Y. Iwasaki,[30] D.J. Jackson,[25] P. Jacques,[24] J. A. Jaros,[28]
Z. Y. Jiang,[28] A.S. Johnson,[3] J.R. Johnson,[33] R.A. Johnson,[7] T. Junk,[28]
R. Kajikawa,[19] M. Kalelkar,[24] H. J. Kang,[26] I. Karliner,[13] H. Kawahara,[28]
H.W. Kendall,[15] Y. D. Kim,[26] M.E. King,[28] R. King,[28] R.R. Kofler,[16]
N.M. Krishna,[9] R.S. Kroeger,[17] J.F. Labs,[28] M. Langston,[20] A. Lath,[15]
J.A. Lauber,[9] D.W.G.S. Leith,[28] V. Lia,[15] M.X. Liu,[34] X. Liu,[6] M. Loreti,[21]
A. Lu,[5] H.L. Lynch,[28] J. Ma,[32] G. Mancinelli,[24] S. Manly,[34] G. Mantovani,[22]
T.W. Markiewicz,[28] T. Maruyama,[28] H. Masuda,[28] E. Mazzucato,[11]
A.K. McKemey,[4] B.T. Meadows,[7] R. Messner,[28] P.M. Mockett,[32]
K.C. Moffeit,[28] T.B. Moore,[34] D. Muller,[28] T. Nagamine,[28] S. Narita,[30]
U. Nauenberg,[9] H. Neal,[28] M. Nussbaum,[7]† Y. Ohnishi,[19] D. Onoprienko,[29]
L.S. Osborne,[15] R.S. Panvini,[31] C.H. Park,[27] H. Park,[20] T.J. Pavel,[28]
I. Peruzzi,[12][b] M. Piccolo,[12] L. Piemontese,[11] E. Pieroni,[23] K.T. Pitts,[20]
R.J. Plano,[24] R. Prepost,[33] C.Y. Prescott,[28] G.D. Punkar,[28] J. Quigley,[15]
B.N. Ratcliff,[28] T.W. Reeves,[31] J. Reidy,[17] P.L. Reinertsen,[6] P.E. Rensing,[28]
L.S. Rochester,[28] P.C. Rowson,[10] J.J. Russell,[28] O.H. Saxton,[28] T. Schalk,[6]
R.H. Schindler,[28] B.A. Schumm,[6] J. Schwiening,[28] S. Sen,[34] V.V. Serbo,[33]
M.H. Shaevitz,[10] J.T. Shank,[3] G. Shapiro,[14] D.J. Sherden,[28] K.D. Shmakov,[29]
C. Simopoulos,[28] N.B. Sinev,[20] S.R. Smith,[28] M.B. Smy,[8] J.A. Snyder,[34]
H. Staengle,[8] P. Stamer,[24] H. Steiner,[14] R. Steiner,[1] M.G. Strauss,[16] D. Su,[28]
F. Suekane,[30] A. Sugiyama,[19] S. Suzuki,[19] M. Swartz,[28] A. Szumilo,[32]

T. Takahashi,[28] F.E. Taylor,[15] E. Torrence,[15] A.I. Trandafir,[16] J.D. Turk,[34] T. Usher,[28] J. Va'vra,[28] C. Vannini,[23] E. Vella,[28] J.P. Venuti,[31] R. Verdier,[15] P.G. Verdini,[23] D.L. Wagner,[9] S.R. Wagner,[28] A.P. Waite,[28] S.J. Watts,[4] A.W. Weidemann,[29] E.R. Weiss,[32] J.S. Whitaker,[3] S.L. White,[29] F.J. Wickens,[25] D.C. Williams,[15] S.H. Williams,[28] S. Willocq,[28] R.J. Wilson,[8] W.J. Wisniewski,[28] M. Woods,[28] G.B. Word,[24] J. Wyss,[21] R.K. Yamamoto,[15] J.M. Yamartino,[15] X. Yang,[20] J. Yashima,[30] S.J. Yellin,[5] C.C. Young,[28] H. Yuta,[30] G. Zapalac,[33] R.W. Zdarko,[28] and J. Zhou,[20]

[1] *Adelphi University, Garden City, New York 11530*

[2] *INFN Sezione di Bologna, I-40126 Bologna, Italy*

[3] *Boston University, Boston, Massachusetts 02215*

[4] *Brunel University, Uxbridge, Middlesex UB8 3PH, United Kingdom*

[5] *University of California at Santa Barbara, Santa Barbara, California 93106*

[6] *University of California at Santa Cruz, Santa Cruz, California 95064*

[7] *University of Cincinnati, Cincinnati, Ohio 45221*

[8] *Colorado State University, Fort Collins, Colorado 80523*

[9] *University of Colorado, Boulder, Colorado 80309*

[10] *Columbia University, New York, New York 10027*

[11] *INFN Sezione di Ferrara and Università di Ferrara, I-44100 Ferrara, Italy*

[12] *INFN Lab. Nazionali di Frascati, I-00044 Frascati, Italy*

[13] *University of Illinois, Urbana, Illinois 61801*

[14] *E.O. Lawrence Berkeley Laboratory, University of California, Berkeley, California 94720*

[15] *Massachusetts Institute of Technology, Cambridge, Massachusetts 02139*

[16] *University of Massachusetts, Amherst, Massachusetts 01003*

[17] *University of Mississippi, University, Mississippi 38677*

[18] *Moscow State University, Institute of Nuclear Physics 119899 Moscow, Russia*

[19] *Nagoya University, Chikusa-ku, Nagoya 464 Japan*

[20] *University of Oregon, Eugene, Oregon 97403*

[21] *INFN Sezione di Padova and Università di Padova, I-35100 Padova, Italy*

[22] *INFN Sezione di Perugia and Università di Perugia, I-06100 Perugia, Italy*

[23] *INFN Sezione di Pisa and Università di Pisa, I-56100 Pisa, Italy*

[24] *Rutgers University, Piscataway, New Jersey 08855*

[25] *Rutherford Appleton Laboratory, Chilton, Didcot, Oxon OX11 0QX United Kingdom*

[26] *Sogang University, Seoul, Korea*

[27] *Soongsil University, Seoul, Korea 156-743*

[28] *Stanford Linear Accelerator Center, Stanford University, Stanford, California 94309*

[29] *University of Tennessee, Knoxville, Tennessee 37996*

[30] *Tohoku University, Sendai 980 Japan*

[31] *Vanderbilt University, Nashville, Tennessee 37235*

[32] *University of Washington, Seattle, Washington 98195*

[33] *University of Wisconsin, Madison, Wisconsin 53706*

[34] *Yale University, New Haven, Connecticut 06511*

[†] *Deceased*

[a] *Also at the Università di Genova*

[b] *Also at the Università di Perugia*

Bibliography

[1] S. Glashow, Nucl. Phys. **22**, 579, 1961.

[2] S. Weinberg, Phys. Rev. Lett. **19**, 1264, 1967.

[3] A. Salam, in *Elementary Particle Theory*, p. 367. ed. N. Svartholm, Almqvist and Wiksell, Stockholm, 1968.

[4] F. Halzen and A.D. Martin, *Quarks and Leptons : an Introductory Course in Modern Particle Physics*, John Wiley and Sons, New York, 1984.

[5] D. Griffiths, *Introduction to Elementary Particles*, John Wiley and Sons, New York, 1987.

[6] *Precision Tests of the Standard Electroweak Model*, P. Langacker (editor), World Scientific, 1995.

[7] T.D. Lee and C.N. Yang, Phys. Rev. **104**, 254, 1956.

[8] C.S. Wu, E. Ambler, R.W. Hayward, D.D. Hoppes, and R.P. Hudson, Phys. Rev. **105**, 1413, 1957.

[9] R.L. Garwin, L.M. Lederman, and M. Weinrich, Phys. Rev. **105**, 1415, 1957.

[10] V.L. Telegdi and J.I. Friedman, Phys. Rev. **105**, 1681, 1957.

[11] F.J. Hasert *et al.*, Phys. Lett. **B46**, 121, 1973.

[12] P. Musset, Jour. de Physique **11/12**, 34, 1973.

[13] G. Arnison *et al.* (UA1 Collaboration), Phys. Lett. **B134**, 469, 1984.

[14] G. Arnison *et al.* (UA1 Collaboration), Phys. Lett. **B126**, 398, 1983.

[15] S. Abachi *et al.* (D0 Collaboration), Phys. Rev. Lett. **74**, 2632, 1995.

[16] F.Abe *et al.* (CDF Collaboration), Phys. Rev. Lett. **74**, 2626, 1995.

[17] S. Dittmaier, D. Schildknecht, Phys. Lett. **B391**, 420, 1997

[18] C.Y. Prescott *et al.*, Phys. Lett. **B77**, 347, 1978; **B84**, 524, 1979.

[19] A. Argento *et al.*, Phys. Let. **B120**, 245, 1983; **B140**, 142, 1984.

[20] W. Heil *et al.*, Nucl. Phys. **B327**, 1, 1989.

[21] P.A. Souder *et al.*, Phys. Rev. **65**, 694, 1990.

[22] C.S. Wood *et al.*, Science **275**, 1759, 1997.

[23] R. Prepost, Private Communication, 1997.

[24] P. Clarke, Rutherford Appleton Laboratory preprint RAL-90-055, 1990.

[25] D. Bardin *et al.*, European Organization for Particle Physics preprint CERN-TH-6443, 1992.

[26] P.C. Rowson, presented at the 1997 Rencontres de Moriond, Electroweak Session, March 1997; to be published in the proceedings.

[27] A. Boehm, presented at the 1997 Rencontres de Moriond, Electroweak Session, March 1997; to be published in the proceedings.

[28] P. Emma, Proceedings of the 16th IEEE Particle Accelerator Conference (PAC 95) and International Conference on High Energy Accelerators, pp.606-610, Dallas, Texas, May 1995.

[29] R. Koontz *et al.*, Proceedings of the 15th International Linear Accelerator Conference (LINAC 92), vol. 2, pp.740-742, Ottawa, Canada, August 1992.

[30] R. Alley *et al.*, Nucl. Instrum. Methods **A365**, 1, 1995.

[31] R. Prepost and T.Maruyama, Ann. Rev. Nucl. Part. Sci. **45**, 41, 1995.

[32] M. Woods, Proceedings of the 12th International Symposium on High-Energy Spin Physics, pp.843-845, Amsterdam, The Netherlands, 1996.

[33] K. Bane *et al.*, Proceedings of the IEEE Particle Accelerator Conference (PAC 95), pp.3105-3108, Dallas, Texas, May 1995.

[34] F.J. Decker, R. Holtzapple, T. Raubenheimer, Proceedings of the 17th International Linear Accelerator Conference (LINAC 94), pp.47-49, Tsukuba, Japan, 1994.

[35] F. Zimmermann *et al.*, Proceedings of the IEEE Particle Accelerator Conference (PAC 95), pp. 656-658, Dallas, Texas, May 1995.

[36] SLD Design Report, Stanford Linear Accelerator Center preprint SLAC-REPORT-273, 1984.

[37] G. Agnew *et al.*, Proceedings of the 26-th International Conference on High Energy Physics, pp.1862-1866, Dallas, Texas, August 1992.

[38] C.J.S. Damerell, Rutherford Appleton Laboratory preprint RAL-P-95-008, December 1995.

[39] M. Hildreth *et al.*, Nucl. Instrum. Methods **A367**, 111, 1995.

[40] M. Cavalli-Sforza *et al.*, IEEE Trans. Nucl. Sci. **37**, 1132, 1990.

[41] D. Axen *et al.*, Nucl. Instrum. Methods **A238**, 472, 1993.

[42] A.C. Benvenuti *et al.*, Nucl. Instum. Methods **A290**, 353, 1990.

[43] T. Sjostrand and M. Bengtsson, Comput. Phys. Commun. **43** 367, 1987.

[44] T. Sjostrand, European Organization for Particle Physics preprint CERN-TH-7112-93, February 1994.

[45] C. Peterson, D. Schlatter, I. Schmitt and P.M. Zerwas, Phys. Rev. **D27**, 105, 1983.

[46] M. Artuso (CLEO Collaboration), talk presented at Workshop on b Physics at Hadron Accelerators, Snowmass, CO, Jun 1993; Published in Snowmass B Physics 1993, pp. 97-108.

[47] T.R. Junk, Ph.D. Thesis, Stanford University, Appendix E, November 1995, published as Stanford Linear Accelerator Center preprint SLAC-REPORT-476, 1995.

[48] The Particle Data Group, Phys. Rev. **D50**, Part I, 1994.

[49] GEANT program, version 3.21, CERN Application Software Group, CERN Program Library, 1993;
R. Brun *et al.*, GEANT3 User's Guide, European Organization for Particle Physics preprint CERN-DD/EE/84-1, 1987.

[50] H.A. Neal, Jr. II, Ph.D. Thesis, Stanford University, published as Stanford Linear Accelerator Center preprint SLAC-REPORT-473, 1995.

[51] D. Buskulic *et al.*, (ALEPH Collaboration), Phys. Lett. **B313**, 545, 1993.

[52] B. Schumm, Stanford Linear Accelerator Center SLD Physics Note 23, 1993 (unpublished).

[53] P.N. Burrows, Stanford Linear Accelerator Center SLD Physics Note 29, 1994 (unpublished).

[54] J.B. Stav and H.A. Olsen, Phys. Rev. **D52**, 1359, 1995; Phys. Rev. **D50**, 6775, 1994.

[55] B. Lampe, Max Planck Institute preprint MPH-PH-93-74, 1993.

[56] A. Djouadi, B. Lampe and P.M. Zerwas, Z. Phys. **C67**, 123, 1995.

[57] R.D. Field and R.P. Feynman, Nucl.Phys. **B136**, 1, 1978.

[58] D. Jackson, Nucl. Instrum. Methods **A388**, 247, 1997.

[59] K. Abe *et al.* (SLD Collaboration), Stanford Linear Accelerator Center preprint SLAC-PUB-7170, 1996; J. Coller, S. Dong, E. Etzion, and E. Weiss, Stanford Linear Accelerator Center SLD Physics Note 57, 1997 (unpublished).

[60] J.A. Lauber, Ph.D. Thesis, Stanford University, February 1993, published as Stanford Linear Accelerator Center preprint SLAC-REPORT-413, 1993.

[61] K. Abe *et al.* (SLD Collaboration), Phys. Rev. Lett. **74**, 2890, 1995.

[62] K. Abe *et al.* (SLD Collaboration), Phys. Rev. Lett. **74**, 2895, 1995.

[63] K. Abe *et al.* (SLD Collaboration), Nuovo Cimento **A109**, 663, 1996.

[64] OPAL Collaboration, Phys. Lett. **B294**, 436, 1992.

[65] OPAL Collaboration, Z. Phys. **C60**, 19, 1993.

[66] OPAL Collaboration, Z. Phys. **C60**, 601, 1993.

[67] ALEPH Collaboration, Phys. Lett. **B335**, 99, 1994.

[68] L3 Collaboration, Z.Phys. **C62**, 551, 1994.

[69] DELPHI Collaboration, Z.Phys. **C65**, 569, 1995.

[70] OPAL Collaboration, Z. Phys. **C67**, 365, 1995.

[71] OPAL Collaboration, European Organization for Particle Physics preprint CERN-PPE/97-006, 1997;
Submitted to Z.Phys.

[72] T. Takeuchi, A.K. Grant and J.L. Rosner, Proceedings of the 8th Meeting of the Division of Particles and Fields of the American Physical Society, pp.1231-1235, Albuquerque, NM, August 1994.

[73] G. Altarelli, R. Barbieri and F. Caravaglios, Nucl. Phys. **B405**, 3, 1993;
Phys. Lett. **B314**, 357, 1993.

[74] A. Blondel, A. Djouadi and C. Verzegnassi, Phys. Lett. **B293**, 253, 1992;
A. Blondel and C. Verzegnassi, Phys. Lett. **B311**, 346, 1993; D.Comelli, C. Verzegnassi and F.M. Renard, Phys.Rev. **D50**, 3076, 1994.

[75] P. Gambino and A. Sirlin, Phys.Rev. **D49**, 1160, 1994,

[76] M. Swartz, Phys. Rev. **D53**, 5268, 1996.

[77] B. Schumm, Private Communication, 1997.